

ANALYSIS OF SMALL SCALE LUNAR GRAVITY ANOMALIES:  
IMPLICATIONS FOR CRATER FORMATION AND CRUSTAL  
HISTORY

Thesis by

John Joseph Dvorak

In Partial Fulfillment of the Requirements  
for the Degree of  
Doctor of Philosophy

California Institute of Technology

Pasadena, California

February 19, 1979

Copyright © by  
John Joseph Dvorak  
1979

To my parents

for their support and understanding.

## ACKNOWLEDGEMENTS

I would like to thank Dr. Roger J. Phillips for his guidance and persistence throughout this work and for the many times he talked me out of quitting and kept me on a successful pathway.

A special thanks also goes to W. L. Sjogren for making available the processed lunar gravity data and to S. H. Zisk for providing unpublished radar topographic maps of selected areas of the Moon; both were essential in conducting this research. E. A. Abbott also played an important role in initializing this work and in being available whenever I became confused with the System.

The discussions and comments provided by H. J. Melosh, E. M. Shoemaker, and D. O. Muhleman were also essential in directing this work to a successful completion.

The frequent discussions I have had with B. G. Bills formed an important part of my education during these past few years and contributed to this thesis. L. M. Fong also played an important role by providing needed distraction from the anguish and anxiety connected with the completion of this work. To my many friends, past and present, I thank them for their encouragement and often unintentional guidance.

And a thanks to C. Seale and K. Campbell for typing this manuscript.

The Apollo photographs were provided by the National Space

Science Data Center. This research was funded by the Lunar and Planetary Programs Office of NASA and carried out at the Jet Propulsion Laboratory and the California Institute of Technology, under contract NAS 7-100, sponsored by the National Aeronautics and Space Administration.

## ABSTRACT

Anomalies in the local gravity field arise from lateral density variations within a planetary body. Hence, a consideration of the nature of these anomalies can be used to infer the subsurface structure and, from this, possibly constrain and characterize the processes which formed these features. Such a consideration is given here to the local gravity anomalies on the Moon.

The lunar *free-air* gravity data consist of the line-of-sight (i.e., Earth-to-spacecraft) component of the accelerations undergone by a spacecraft in a low lunar orbit. In this analysis the acceleration or gravity profiles across a feature of interest are corrected for the topographic contribution of the lunar surface to the local gravity field to obtain the *Bouguer* gravity profiles. The availability of lunar features for this analysis is mainly constrained by the nearside areal coverage of low altitude orbiting lunar spacecraft.

A total of twenty-one features are analyzed here of which all but two are of impact origin; these two exceptions are probable sites for intrusive and extrusive igneous activity on the Moon. The impact features have been divided into two major groups on the basis of age with the older group further subdivided into relatively unfilled craters and very shallow craters and also including a small multiringed basin.

The young lunar craters, which range in diameter from 32 to 135 kilometers, have negative Bouguer gravity anomalies (i.e., mass

deficiencies or low density regions) associated with them. Presumably, these low density regions represent material brecciated and crushed by the impact events which formed these craters. Calculations reveal a systematic variation in the magnitude of the total mass deficiency with increasing crater size and a comparison of lunar and terrestrial impact features shows that the magnitude of this mass deficiency is proportional to the cube of the crater diameter. Furthermore, studies of terrestrial impact structures indicate that the major contribution to these negative Bouguer anomalies is most likely due to a large lens of low density material extending laterally to approximately the crater rim crest and vertically to a depth of roughly one-third the rim diameter. Also based on studies of many terrestrial impact features, the maximum depth of the transient cavity associated with these lunar craters, as inferred from the apparent vertical extent of brecciation, was roughly one-fourth the crater rim diameter. This depth possibly also corresponded to the maximum depth of excavation of at least a small amount of the lunar crust by these impact events.

In all but one case, the old unfilled lunar craters have distinctly different Bouguer anomalies from the young lunar craters. With the exception of the crater Piccolomini which follows the trend for the younger craters, all of the remaining unfilled old lunar craters have, within the uncertainties of this analysis, zero Bouguer anomalies. The cause for this change in the value of the Bouguer gravity is, of course, expected to be related to the greater age and more modified appearance of these craters. A likely possibility is that the porosity initially

produced by the impact events which formed these older craters has been removed by the intrusion of igneous material, roughly contemporaneous with the emplacement on the surface of the lunar mare basalts. A second possibility is that the original porosity has been removed by compaction of the lunar crust during the seismic shaking which accompanied the formation of the last lunar multiringed basins, however, it is difficult to evaluate this mechanism since the efficiency at this scale is unknown.

The two shallow lunar craters for which it is possible to determine the Bouguer gravity have slight negative anomalies. These particular craters are also filled by light plains units which have been interpreted to be ejecta from later multiringed basin impacts. These slight negative anomalies are probably due to the higher porosity of the basin ejecta which now almost completely fills these craters.

The Bouguer gravity of a small multiringed basin, Grimaldi, has also been determined. Spacecraft free-air gravity data reveal a mascon associated with the inner ring of this structure. The topographic correction to the local gravity field indicates a maximum Bouguer anomaly of +90 milligals at an altitude of 70 kilometers. Approximately 20% of this positive Bouguer anomaly can be accounted for by the mare material lying within the inner ring. It is proposed, from a consideration of the Bouguer gravity over large lunar craters comparable in size to Grimaldi, that the remaining positive anomaly is due to a plug of high density lunar mantle material centrally uplifted by the inward collapse of material which resulted in the



formation of the concentric outer scarp. In addition, a ring of low density material, possibly ejecta deposited by the formation of Grimaldi, is required to fully reproduce the Bouguer gravity signature across this basin. A similar structure to the one described here for Grimaldi has been previously proposed for the Orientale Basin.

The two non-impact features, Lamont and Marius Hills, have positive Bouguer anomalies. Since these are probable sites for extrusive igneous activity, that is, possible source areas for the surrounding mare material, these positive gravity anomalies are interpreted to be the result of intrusive activity within the lunar crust, much more intensive activity than the intrusion of material proposed beneath the old lunar craters also analyzed here. At Lamont, located in western Tranquillitatis, the mare ridge pattern and local topography suggest a general subsidence of this region. The gravity data indicate that the density anomaly extends beyond the inner circular ring of mare ridges which define the Lamont feature. The occurrence of a magnetic high at Lamont further supports the presence of a major intrusive body probably emplaced early in lunar history. Several other local gravity or magnetic highs in the lunar mare are also interpreted as the result of intrusive activity. At Marius Hills, an isolated plateau in Oceanus Procellarum, the positive Bouguer anomaly is much smaller than at Lamont and is localized in the northeast corner of the plateau.

## TABLE OF CONTENTS

Chapter		Page
I	INTRODUCTION	1
II	TERRESTRIAL IMPACT STRUCTURES	11
III	LUNAR GRAVITY AND TOPOGRAPHIC DATA	38
	Lunar Gravity Data	38
	Lunar Topographic Data	41
	Orbit Simulation Procedure	53
	Bouguer Gravity	55
	Model Calculations	62
IV	YOUNG LUNAR CRATERS	72
	Introduction	72
	Model Calculations	76
	Discussion	84
V	OLD UNFILLED LUNAR CRATERS	87
	Introduction	87
	Discussion	98
	Summary	113
VI	SHALLOW LUNAR CRATERS	117
	Introduction	117
	Description	118
	Bouguer Gravity	120
	Discussion	131

## TABLE OF CONTENTS

Chapter		Page
VII	GRIMALDI: LUNAR MULTIRINGED BASIN	133
	Introduction	133
	Description	134
	Model Calculations	150
	Discussion	161
	Summary	163
VIII	NON-IMPACT FEATURES	166
	Introduction	166
	LAMONT	167
	Description	167
	Geophysical Data	173
	Discussion	178
	MARIUS HILLS	192
	Description	192
	Geophysical Data	196
	Discussion	197
IX	HISTORY OF THE LUNAR CRUST	199
	Lunar Cratering and Igneous Activity	200
	Lunar Isostasy	207
	APPENDIX	209
	REFERENCES	232

## FIGURES

Number		Page
1	Variation of the mass deficiency, $\Delta M$ , with crater rim diameter, $D_r$ , for terrestrial impact structures.	25
2	Maximum depth of brecciation versus crater diameter.	35
3	Line-of-sight gravity signature as a function of longitude.	43
4	Comparison of elevations determined by LTO and ERT data sets (Ptolemaeus).	46
5	Comparison of elevations determined by LTO and ERT data sets (Langrenus).	49
6	Comparison of crater depths determined by ERT and other data sets.	51
7	Effect of topographic datum level on gravity signature.	58
8	Dependence of the topographic correction on assumed values for the lunar crustal density.	60
9	Schematic diagram of four models for the mass deficiencies associated with young lunar craters.	65
10	Comparison of model calculations with the gravity data across Copernicus.	67
11	Comparison of identical model and topographic calculations for several different orbital tracks across Langrenus.	70
12	Apollo 16 oblique metric photograph of Theophilus.	75
13	Variation of the mass deficiency with crater rim diameter for young lunar craters.	78
14	Comparison of the variation in the mass deficiency associated with terrestrial and young lunar craters with crater rim diameter.	83

## FIGURES

Number		Page
15	Lunar Orbiter photograph of Neper.	91
16	Lunar Orbiter photograph of Humboldt.	94
17	Lunar Orbiter photograph of Piccolomini.	97
18	Comparison of $\Delta M$ values determined for young lunar craters with upper bound values of $\Delta M$ for unfilled Imbrian and pre-Imbrian age craters.	100
19	Lunar Orbiter photograph of the central lunar nearside.	120
20	Apollo 16 metric photograph of Ptolemaeus.	122
21	Apollo 16 oblique metric photograph of Hipparchus.	124
22	Comparison of $\Delta M$ values for Ptolemaeus and Hipparchus with other lunar craters.	130
23	Lunar Orbiter photograph of the western limb of the Moon.	136
24	Schematic map of the same region shown in Figure 23.	138
25	Lunar Orbiter photographs detailing Grimaldi.	141
26	Earth-based radar topographic (ERT) map of Grimaldi.	143
27	Lunar Orbiter photograph of Schrödinger Basin.	147
28	Comparison of the gravity profile across Grimaldi with several model calculations.	154
29	Schematic cross-section of Grimaldi.	158
30	Earth-based photograph of western Tranquillitatis.	169
31	Earth-based radar topographic (ERT) map of the Lamont region.	172

## FIGURES

Number		Page
32	Comparison of model calculations with the Bouguer profiles across Lamont.	176
33	Map of the scalar magnitude of the lunar magnetic field.	181
34	Proposed history of the Lamont and western Tranquillitatis region of the Moon.	186
35	Lunar Orbiter photographs of Marius Hills.	194
36	Lunar Orbiter photograph of southern Mare Australe showing the partial flooding of a highly cratered region.	205

## TABLES

Number		Page
I	Free-air gravity maps of the Moon.	4
II	Lunar features analyzed in this work.	5
III	Summary of terrestrial impact structures.	6
IV	Comparison of crater depth determinations.	52
V	Summary of young lunar craters.	73
VI	Summary of old unfilled lunar craters.	88
VII	Summary of shallow lunar craters.	128
VIII	Gravity models for Grimaldi.	160
IX	Gravity values for Grimaldi--Present and past.	164





The Moon is a harsh mistress.

--Robert A. Heinlein

## CHAPTER I

## INTRODUCTION

A great deal of theory, experimental work and conjecture has been brought to bear on the problem of the formation and evolution of lunar impact craters. The unraveling of partial solutions to this problem is important since these solutions will lead to a better understanding of the impact process and to a better characterization of the crustal processes operating to modify the original crater form. Studies of lunar craters have been primarily confined to an interpretation of the surficial geology based on lunar orbital photography and to inferences drawn from analogies with terrestrial impact structures and experimentally produced impact and explosion craters. These studies have been invaluable in characterizing the impact process and in delineating the stratigraphic record of the lunar surface, and, also, in formulating ideas and concepts to account for transitions in crater morphology with increasing crater diameter and increasing crater age. To some extent the detailed photographic coverage of the lunar surface by orbiting spacecraft and the results from the Apollo landings have enabled lunar scientists to eliminate some hypotheses initially proposed from solely Earth-based observations to account for the present lunar landscape. However, many ambiguities remain. Some of these ambiguities cannot be further resolved without resorting to additional constraints imposed by other data types. With this purpose in mind, a comprehensive study of the gravity anomalies associated with lunar craters is presented in an effort to

further constrain their structures, and, by inference from these results, to characterize their mode of formation and evolution.

Several investigators have previously used this method to study lunar craters (Gottlieb et al., 1970; Sjogren et al., 1972a; 1974a). The present work deals with a more careful examination of the lunar gravity and topographic data than previously given and will present results of a more quantitative nature and for a larger number of lunar features than reported by earlier investigators.

The lunar gravity values are the line-of-sight accelerations derived by differentiating with respect to time the measured Doppler shift residual in the Earth-based navigational tracking of a spacecraft in a low lunar orbit. This analysis considers several profiles of the local accelerations undergone by a spacecraft as it passes over a feature of interest. These accelerations are termed the *free-air* gravity and are due to the combined gravitational effects of surface topography and lateral density variations within the Moon.

This technique of deriving lunar gravity values from measured variations in spacecraft velocity has been used for many years starting with an analysis of the Lunar Orbiter spacecraft series which first revealed the association of positive free-air gravity anomalies (called mascons) with mare-filled multiringed lunar basins (Muller and Sjogren, 1968). The later Apollo missions contributed to the coverage and resolution of lunar gravity data, especially in making available low altitude orbital passes which resolved many individual lunar features.

The free-air gravity maps which resulted from each mission have been published as a series of papers and are listed in Table I for reference.

Mission constraints on Apollo spacecraft orbital geometry and altitude limited the availability of lunar features for this analysis to the lunar equatorial region and a portion of the eastern limb. Excluding the major basins, a total of twenty-one lunar features, for which there exists adequate topography, are identified here with observed free-air gravity anomalies. These features are listed alphabetically in Table II along with the diameter and the crater rim-to-floor depth, the stratigraphic age of each feature, and the location on the lunar surface. Also given in Table II are the orbits which were determined to be of sufficient quality for use in this analysis, the approximate spacecraft altitude over each feature, and the chapter in which each feature is discussed. The remaining orbital coverage was either repetitive of the coverage already provided or was deemed unsuitable for this analysis due to data gaps in or poor determinations of the accelerations from the Doppler data.

The small spatial scale of most of the lunar gravity anomalies discussed here requires that the density variations giving rise to these anomalies reside within the lunar crust. The topographic contribution to each gravity profile has been determined and removed by an orbit simulation procedure which takes into account the peculiarities in deriving the lunar gravity values. The remaining

TABLE I

## FREE-AIR GRAVITY MAPS OF THE MOON

<u>Lunar Mission</u>	<u>Reference</u>
Lunar Orbiter V	Muller and Sjogren, 1968
Apollo 12 LEM (descent)	Gottlieb et al., 1970
Apollo 14 CSM	Sjogren et al., 1972 a
Apollo 15 CSM	Muller et al., 1974
Apollo 15 subsatellite	Sjogren et al., 1974a
Apollo 16 CSM	Sjogren et al., 1974b
Apollo 16 subsatellite	Sjogren et al., 1974a
Apollo 17 CSM	Sjogren et al., 1974c

TABLE II  
LUNAR FEATURES ANALYZED IN THIS WORK

NAME	DIAMETER	DEPTH	AGE	LATITUDE	LONGITUDE	ORBITS	ALTITUDE	CHAPTER
Agrippa	46 km	3.0 km	C	4.1	10.6	16SS Rev 210	16 km	IV
Copernicus	93	3.8	C	9.7	-20.0	Ap 17 CSM Rev 3 Ap 17 CSM Rev 6 16SS Rev 194	34 31 25	IV
Eratosthenes	58	3.5	E	14.5	-11.4	Ap 17 CSM Rev 10	23	IV
Grimaldi	200 (inner) 400 (outer)	2.0	pl	-5.2	-68.0	Ap 17 CSM Rev 3 Ap 17 CSM Rev 7 Ap 17 CSM Rev 11 15SS Rev 1557	67 63 58 88	VII
Hecataeus	120	4.0	pl	-23.0	79.4	15SS Rev 1529 15SS Rev 1533 15SS Rev 6565	62 66 48	V
Herschel	42	3.3	E	5.5	-2.0	Ap 14 CSM Rev 7	17	IV
Hipparchus	150	1.1	pl	-5.5	5.2	Ap 14 CSM Rev 3 Ap 14 CSM Rev 7	17 14	VI
Humboldt	200	3.0	pl	-26.9	80.7	15SS Rev 1503 15SS Rev 6502 15SS Rev 6526	53 62 45	V
Kepler	32	2.7	C	8.2	-37.9	16SS Rev 218 16SS Rev 220 16SS Rev 222	20 19 18	IV

C = Copernican  
E = Eratosthenian  
I = Imbrian  
pl = pre-Imbrian

TABLE II (CONTINUED)

NAME	DIAMETER	DEPTH	AGE	LATITUDE	LONGITUDE	ORBITS	ALTITUDE	CHAPTER
*Lamont	70 km	---	I - pl	5.0	23.5	16SS Rev 170 16SS Rev 185 16SS Rev 194 15SS Rev 1443 15SS Rev 6673 15SS Rev 6838	18 16 19 140 141 120	VIII
Langrenus	135	4.4 km	C	-8.9	61.1	Ap 16 CSM Rev 4 Ap 16 CSM Rev 8 Ap 16 CSM Rev 15	23 24 26	IV
Macrobius	65	4.0	I	21.4	46.0	Ap 15 CSM Rev 10	16	V
*Marius Hills	350	---	E - I	13	- 52	Ap 15 CSM Rev 5 Ap 15 CSM Rev 7 Ap 15 CSM Rev 10	43 40 36	VIII
Neper	150	4.4	pl	8.9	84.9	Ap 15 CSM Rev 3 Ap 15 CSM Rev 5 Ap 15 CSM Rev 6	33 35 36	V
Pasteur	240	3.0	pl	-12.0	105.0	Ap 14 CSM Rev 11 15SS Rev 1525	75 81	V
Petavius	176	3.0	I	-25.4	60.5	15SS Rev 1491 15SS Rev 6565 15SS Rev 6571 15SS Rev 6574	63 39 41 42	V
Piccolomini	89	3.0	I	-29.5	32.2	15SS Rev 1535 15SS Rev 6559 15SS Rev 6565	46 43 39	V
Ptolemaeus	150	1.8	pl	-9.0	-1.8	Ap 16 CSM Rev 4 Ap 16 LEM Rev 15	30 26	VI

\*non-impact feature

TABLE II (CONTINUED)

NAME	DIAMETER	DEPTH	AGE	LATITUDE	LONGITUDE	ORBITS	ALTITUDE	CHAPTER
Sacrobosco	96 km	2.0 km	pI	-23.7	16.5	15SS Rev 1517	58	V
						15SS Rev 6619	58	
Snellius	83	3.1	I - pI	-29.5	55.7	15SS Rev 6544	40	V
						15SS Rev 6547	40	
						15SS Rev 6550	40	
Theophilus	100	4.6	C	-11.5	26.3	Ap 14 CSM Rev 7	20	IV



gravity anomaly, due solely to lateral density variations within the crust, is termed the *Bouguer* anomaly.

The interpretation of these lunar Bouguer gravity anomalies is complicated by differences in spacecraft altitude and areal coverage over each particular feature. These differences are accounted for by use of an orbit simulation procedure, identical to that used in the determination of the Bouguer gravity, which allows a net mass deficiency or excess to be related to each Bouguer anomaly, independent, within the uncertainties of this analysis, of assumptions about the density structure.

The nature of the density anomalies responsible for **variations** in the Bouguer gravity is expected to vary systematically with both the size and the age of the crater. The strategy adopted to reveal these variations is to first understand the nature of the gravity anomalies associated with the youngest lunar craters and then to apply these results to older, more degraded craters which have been subjected to a wider variety of processes. Young lunar craters are those which, within a given size range, exhibit the least amount of post-impact modification. In terms of lunar stratigraphy, these lunar craters belong to either the Copernican or Eratosthenian systems. It is assumed that all lunar craters of any given diameter range had the same original crater form as the young craters, however, simply because of their greater age, the older lunar craters have also been subjected to additional processes which either are not now operating or have had insufficient time to modify the younger craters.

The older group of lunar craters, Imbrian and pre-Imbrian in age, have been divided into two groups. The relatively unfilled old craters are those which have depth/diameter ratios similar to the ratios of the young lunar craters of the same diameter range, i.e., crater depths of several kilometers. In the second group are shallow craters whose original crater bowls have been almost completely filled, leaving only the rim of the crater visible. A small multiringed basin, Grimaldi, is also included in this work as it is the only lunar basin for which adequate topographic maps are available to compute the Bouguer gravity and as Grimaldi is comparable in size to several of the lunar craters also considered here. This small basin represents a transition in form between the smaller impacts which produced the flat-floored lunar craters and the larger impacts which resulted in the formation of multiple ring basins.

The Bouguer gravity of two non-impact related features, Lamont and Marius Hills, two probable sites for intrusive and extrusive igneous activity on the Moon, have also been determined. The major spatial extent of the intrusive activity associated with these features can be constrained by the gravity data which can then be related to the style and history of surface volcanism at each site.

The intent of this work will be to determine the nature and spatial extent of the anomalous mass or density regions and their variation with crater size and crater age and to discuss the implications that these results have in terms of characterizing the process of impact on a planetary surface and of characterizing those

processes acting on the lunar crust to modify these features. To begin, a summary of current studies of the subsurface structure of terrestrial impact features will be given as a guide to the interpretation of the lunar impact craters. Special emphasis will be placed here on understanding the nature of the anomalous mass components giving rise to the gravity anomalies associated with these terrestrial features. Next will be a description of the lunar gravity and topographic data and of the procedure used in determining and modeling the Bouguer gravity, outlining the biases and errors introduced by this analysis. In turn, the young, the old unfilled, and the shallow lunar craters will be presented and the probable nature of the Bouguer anomalies associated with these features and the possible causes for systematic changes in the mass anomaly with increasing crater diameter and increasing crater age will be discussed. The structure of Grimaldi will be presented next along with a discussion which will view the result for Grimaldi in terms of the earlier results determined for other large lunar craters which did not result in the formation of a multiringed structure. The extent of postulated intrusions associated with Lamont and Marius Hills, as determined from the gravity data, will follow and will be compared with the style of volcanism suggested by the different surface morphology at each site. The final chapter will place the study of lunar gravity anomalies in context with the results of other lunar research, exploring possible implications this work has for the formation and evolution of these lunar features and for the style of igneous activity in the lunar crust.

## CHAPTER II

## TERRESTRIAL IMPACT STRUCTURES

The recognition of impact cratering as an ongoing geologic process on the surface of the Earth and the identification of the resultant structures was one of the major advances in the geological sciences during the past several decades. It is probably no coincidence that this recognition occurred during the years immediately preceding the detailed geologic study of the Moon. In this chapter, the structure of these impact features will be summarized with particular emphases on the nature of the gravity anomalies associated with these features and on variations in their basic structure with increasing size.

The presence of iron-nickel meteoritic material or the identification of the products of shock metamorphism is considered by most to be definitive evidence for the presence of a hypervelocity impact structure (e.g., Dence et al., 1977) since no other known geologic process is capable of accounting for the presence of the iron-nickel material or of generating pressures sufficiently high to account for the presence of the products of shock metamorphism (French, 1968). Such products include the occurrence of high pressure mineral phases such as coesite or stishovite ( $> 20$  kbars, Stöffler, 1971a), the microscopic disruption of individual mineral grains (e.g., Bunch, 1968), or the morphologic features known as shatter cones described by Dietz (1968). Other characteristics which may suggest the occurrence of

an impact structure and, hence, induce the search for one of the above presumably definitive indicators, include an approximately circular structure, concentric faulting and folding, and the presence of a lens-shaped brecciated region suggested by the surface geology or by geophysical measurements revealing a negative gravity anomaly, a subdued magnetic anomaly, or anomalously low seismic velocities.

At present, some sixty sites on the Earth have been identified, on the basis of the occurrence of meteorite material or of the products of shock metamorphism, to be probable locations for impact structures varying from a fraction of a meter to 100 kilometers in diameter. Another 120 sites are possible locations for features of impact origin based on the identification of several of the other characteristics mentioned above (see Classen, 1977).

Basic to the identification and understanding of impact features is the concept of progressive shock metamorphism. For referral, this concept has been discussed in more detail than presented here by Stöffler (1971b) and in reference to Meteor Crater by Kieffer (1971), West Hawk Lake by Short (1970), and Ries Basin by Dennis (1971). Briefly, the impact velocity of a cosmic body onto a planetary surface is on the order of the planetary orbital velocity ( $\sim 10$  km/sec) which is sufficient to generate peak pressures in the megabar range. These pressures far exceed the crushing strength of rocks ( $\sim$  kilobars) so that during the initial stage of impact a region of the target material will behave hydrodynamically. Shock waves will be produced

within both the target and the projectile resulting in almost complete melting and vaporization of the latter. Within the target material the strength or peak pressure of the shock wave will be reduced as it propagates away from the penetrating meteorite owing to geometric spreading of the wave front and to attenuation within the target medium by irreversible processes, such as heating and comminution. Subsequent release of this high pressure to the ambient value will be accomplished by rarefaction or expansion waves following the passage of the shock wave. The most intensely shocked target material will be melted with a small amount vaporized. Intermixed with and concentric to this melt will be severely crushed and brecciated rock which has undergone large permanent strains and beyond this will be a region of unmixed fractured material grading into undisturbed country rock. Localized variations on this general theme of progressive shock metamorphism of material which remained within the crater will be due to inhomogeneities of the target material.

Ejected material deposited within and around the crater will not follow this simplified picture of a concentric, outwardly decreasing, peak shock history. A change in the intensity and form of the shock and rarefaction waves due to the presence of the stress-free surface alters the flow pattern from a radial and downward pattern deep within the crater to an upward and outward movement near the surface. Hence, the mode of transport and degree of mixing of the ejected material is different from the bulk of the crushed material which remained in the crater bowl.

These distinctions, based on the shock history and the mode of transport or the flow pattern and the final deposition of material, can be used to identify various components comprising the overall structure of a crater produced by impact. These components will be discussed later in this chapter as they pertain to evaluating the relative contribution of each component to the negative gravity anomalies associated with most terrestrial impact craters.

A major structural change has been recognized in terrestrial impact features with increasing size. The smaller features, termed simple craters by Dence (1965), are bowl-shaped often with raised rims and depth/diameter ratios in the range of 1/6 to 1/5 (Pike, 1974). Examples of this type of structure are Meteor Crater (1.2 km diam), Lonar Lake (1.8 km), and Brent Crater (3.5 km). Most terrestrial impact features belong to the class of larger diameter structures termed complex by Dence (1965). The greater abundance of this complex type is probably due to their larger size which favors the preservation and easier identification of the feature. These complex craters have a shallower depth/diameter ratio than that for simple craters and are usually characterized by a broad central uplift surrounded by a peripheral depression or trough and possibly a slightly raised rim. Some of the larger features of this class may be analogous to the multiringed basins on the Moon. Examples of these complex structures are the Steinheim (3.4 km diam) and Ries (22 km) Basins and the Flynn Creek (3.8 km) and Manicouagan (65 km) Structures.

Further subdivisions within each of these two categories have been presented by Krinov (1963) and Dence (1965). The transitional diameter, which is probably a gradual one, from a simple to a complex impact structure on the Earth is from two to four kilometers, dependent on the impact parameters, the nature of the meteorite and its impact velocity and angle, and on the characteristics of the target medium, its strength and inhomogeneities, especially important is the vertical stratification of the target medium.

Listed in Table III, in order of increasing diameter, are terrestrial features which have been determined to be the probable result of impact and whose subsurface structures have been at least partially examined by geophysical techniques and drill holes. For five features in Table III (Temimchat Ghallaman, Pretoria Salt Pan, Versailles, Jephtha Knob, and Skeleton Lake) an impact origin is strongly suggested, though has not been confirmed by the identification of one of the definitive indicators of impact origin. Only the results of gravimetry and drilling are summarized in Table III though magnetic and seismic surveys have also been conducted over many of these same features. These various geophysical techniques will detect different aspects of an impact structure, and, as such, are of greatest use when the results of all techniques are available. Unfortunately, this is the case for only a few of the structures listed in Table III and thus it is these features which are most relied upon to give a representative picture of the structure which results from impact cratering.



TABLE III  
SUMMARY OF TERRESTRIAL IMPACT STRUCTURES

NAME; LOCATION	DIAMETER (km)	BOUGUER ANOMALY (mgal)	MASS DEFICIENCY (gm)	$\Delta\rho$ (gm/cm <sup>3</sup> )	REFERENCE	DEPTH OF BRECCIATION (km)	REFERENCE
Odessa No. 2; Texas	0.021					0.005	Evans (1961)
Odessa (main); Texas	0.17					0.027	Evans (1961)
Aouelloul; Mauritania, Africa	0.4	-1	$-5 \times 10^{12}$	-0.3	Fudali and Cassidy (1972)		
Temimchat Ghallaman; Mauritania, Africa	0.7	-2.5	$-4 \times 10^{13}$	-0.3	Fudali and Cassidy (1972)		
Pretoria Salt Pan; South Africa	1.1	-5	$-2 \times 10^{14}$	-0.3	Fudali et al. (1973)		
Meteor Crater; Arizona	1.2	-0.6	$-3 \times 10^{13}$	-0.12	Regan and Hinze (1975)	0.335	Roddy et al. (1975)
Versailles; Kentucky	~1.5	~0			Seeger (1972)		
Lunar Lake; India	1.8					0.485	Fredriksson et al. (1973)
Tenoumer; Mauritania, Africa	1.9	-10	$-1 \times 10^{15}$	-0.3	Fudali and Cassidy (1972)		
Jeptha Knob; Kentucky	2	+1			Seeger (1968)	0.5	Seeger (1968)
Holleford; Ontario	2.3	-2	$-3 \times 10^{14}$	-0.23	Innes (1961)	> 0.35	Beals et al. (1963)
West Hawk Lake; Manitoba	2.7	-6	$-7 \times 10^{14}$	-0.3	Halliday and Griffin (1963)	0.53	Halliday and Griffin (1967)
New Quebec Crater; Quebec	2.7	-6	$-7 \times 10^{14}$		Innes (1964)		
Skeleton Lake; Ontario	3	-3	$-3 \times 10^{14}$		Robertson and Grieve (1975)		
Poplar Bay; Manitoba	3	-7	$-8 \times 10^{14}$		Trueman (1976)		

TABLE III (CONTINUED)

NAME; LOCATION	DIAMETER (km)	BOUGUER ANOMALY (mgal)	MASS DEFICIENCY (gm)	$\Delta\rho$ (gm/cm <sup>3</sup> )	REFERENCE	DEPTH OF BRECCIA (km)	REFERENCE
Steinheim Basin; West Germany	3.4	-2	-3 x 10 <sup>14</sup>		Jensch (1965); Reiff (1977)		Beals et al. (1963)
Brent Crater; Ontario	3.5	-5	-9 x 10 <sup>14</sup>	-0.17	Innes (1961)	1.2	Beals et al. (1963)
Flynn Creek; Tennessee	3.8	~0			Roddy (1968; 1977)	0.2	Roddy (1968; 1977)
Wells Creek; Tennessee	4	<0			Stearns et al. (1968)		
Gow Lake; Saskatchewan	5	-3	-4 x 10 <sup>14</sup>		Robertson and Grieve (1975)		
Serpent Mound; Ohio	6	<0			Bull et al. (1967)		
Nicholson Lake; N.W.T., Canada	9	-7.5	-2 x 10 <sup>16</sup>		Beals and Halliday (1967)		
Lake Wanapitei; Ontario	9	-15	-4 x 10 <sup>16</sup>	-0.2	Dence and Popelar (1972)		
Gosses Bluff; Northern Australia	10	-4	-1 x 10 <sup>16</sup>		Milton et al. (1972)	*1 - 2	Milton et al. (1972)
Deep Bay; Saskatchewan	12	-20	-2 x 10 <sup>16</sup>	-0.17	Innes (1961)	*2 - 4	Sander et al. (1964)
Sierra Madera; Texas	12(?)	-1.5	-2 x 10 <sup>15</sup>		Van Lopik and Geyer (1963)		
East Clearwater; Quebec	19	-10	-4 x 10 <sup>16</sup>		Dence et al. (1965)	0.725	Dence (1968)
Ries Basin; West Germany	22	-18	-7 x 10 <sup>16</sup>	-0.1	Pohl et al. (1977)	*2 - 4	Pohl et al. (1977)
Boltysh Depression; USSR	23					1	Yurk et al. (1975)

\*Seismic determination

TABLE III (CONTINUED)

NAME; LOCATION	DIAMETER (km)	BOUGUER ANOMALY (mgal)	MASS DEFICIENCY (gm)	$\Delta\rho$ (gm/cm <sup>3</sup> )	REFERENCE	DEPTH OF BRECCIATION (km)	REFERENCE
West Clearwater; Quebec	32	-6	$-5 \times 10^{16}$		Dence et al. (1965)		
Manicouagan; Quebec	65	0		-0.13	Sweeney (1978)		
Popigai; Yakutian, USSR	72	<0		-0.3	Manaytis et al. (1976)	>1.2	Manaytis et al. (1976)
Sudbury; Ontario	100	>0			Popelar (1972)		
Camelot; lunar crater	0.8					*0.2 - 0.4	Kovach and Watkins (1973)

\* Seismic determination

Magnetic surveys show an absence of magnetic anomalies and gradients associated with many of these features, especially with simple impact craters such as Meteor Crater (Regan and Hinze, 1975) which formed in sedimentary rocks and Brent Crater (Beals et al., 1963) which formed in crystalline rocks. This lack of magnetic anomalies is consistent with the notion that the metallic projectiles which formed at least some of these features were completely melted or vaporized during the impact and do not presently exist as major bodies buried beneath the surface. Furthermore, pre-existing regional magnetic trends are disrupted by these features, the result of the brecciation and movement of material by the impact with the major region of disturbance confined within the crater rim. Small scale magnetic anomalies have been detected over the central uplift of some complex craters and interpreted to be due to impact melt layers (Ries Basin, Pohl et al., 1977) and to impact-generated magnetization of underlying crystalline rock units (Manicouagan, Coles and Clark, 1978).

Seismic surveys constrain the outward extent of the fractured rock and, when a sufficiently detailed survey is available, also depict progressively decreasing variations in shock effects away from the crater, such as at Meteor Crater (Ackermann et al., 1975) and Deep Bay (Sander et al., 1964). As expected, low seismic velocities are associated with these impact features, the result of the comminution and fracturing of the rock by the large strains produced during the passage of the shock and the rarefaction waves. The values of these anomalously low seismic velocities, relative to the value for

an undisturbed sample, are not a direct function of the porosity but of the crack density (Walsh, 1965). This low seismic velocity region extends vertically a crater radius below the crater floor.

Regions of anomalous density are mapped out by measurements of the variation in gravity across the feature. The values of the Bouguer gravity anomalies over the center of several terrestrial impact features are given in Table III. In most cases the sign of this anomaly is negative indicating a predominantly low density region associated with these features. These low density regions are attributed to an increase in porosity of the shocked and brecciated target material and to later low density sedimentary units deposited within the crater bowl.

For most impact features, especially simple craters, the gravity contours are concentric with the structure and lead to a minimum in the center of the structure, such as at Meteor Crater (Regan and Hinze, 1975) and Ries Basin (see Dennis, 1971). For some complex craters, such as Wells Creek (Stearns et al., 1968) and Manicouagan (Sweeney, 1978), there is a gravity low associated with the peripheral trough and a central high region superposed on this, reaching to approximately the background gravity level, roughly coincident with the lateral extent of the broad central uplifts of these features. Other greatly eroded structures often have concentric gravity contours with many superposed small scale anomalies within the crater corresponding to

the relative displacement of different lithologic units uplifted by the impact, such as at Gosses Bluff (Milton et al., 1972).

Notable positive Bouguer anomalies are associated with the Jephtha Knob and Sudbury Structures. In the former case, this positive anomaly is the result of the dolomitization of the crushed region (Seeger, 1968). For the Sudbury Basin the complexity of the small scale gravity anomalies which exist within this structure is due to the post-impact emplacement of a nickel irruptive and to the occurrence of volcanic and sedimentary surficial rock formations (Popelar, 1972).

A variety of geological processes have acted to varying degrees to modify the remaining craters listed in Table III. In all cases, the material which comprised the original rim has been partially or totally removed and sedimentary deposits have accumulated within the crater bowl. Processes have also acted in some cases on a regional scale to lower the original pre-impact level leaving a deeply eroded structure, such as at Sierra Madera and Crooked Creek (Shoemaker and Eggleton, 1961), in which only the lower portions of the structure are still present. All of these post-impact processes will act to alter the magnitude and, in some cases, change the sign of the Bouguer anomaly. Attempts to apply corrections to the present Bouguer anomalies to determine initial values are futile since, in all but a few cases, the present structure is incompletely known and the restoration to a presumed pristine state is model dependent. It is, however, noteworthy that most of the modifying processes will act to decrease the magnitude of the original negative Bouguer gravity.

anomaly by removal of the raised rim or by the deposition of precipitates by the percolation of groundwater. An exception will be the accumulation of low density sedimentary units which may contribute up to one-half the present value of the negative Bouguer anomalies. However, this depositional process will act to approximately counter the effect on the gravity anomaly of the removal of the rim material.

Gross generalizations about the variation of the magnitude of the mass anomaly with increasing crater size can be made when complete areal gravity surveys are available. The total mass anomaly,  $\Delta M$ , is related to the observed gravity field through Gauss' theorem (Innes, 1961).

$$\Delta M = \frac{1}{2\pi G} \oint g dA = \frac{1}{2\pi G} \sum g_i A_i \quad . \quad (1)$$

The determination of this quantity is independent of assumptions regarding the density structure. However, an uncertainty in  $\Delta M$  is incurred in this summation since it is necessary to extract the localized gravity field associated with the feature of interest from the background regional field. Standard procedures which exist for performing this removal will determine  $\Delta M$  to ten percent (Innes, 1961). Values of  $\Delta M$  for most of the craters listed in Table III were estimated by graphically performing the above summation, either by the quoted sources or by this author. When only sparse coverage of the gravity field or a single profile across the feature is available, a geometrical model must be proposed for the anomalous density region to determine  $\Delta M$ . In these cases, the model was a thin ellipsoid whose

diameter was equal to the diameter of the crater. The surface density required to reproduce the available gravity data was determined and used in the computation of  $\Delta M$ .

These values of  $\Delta M$  for terrestrial impact structures are plotted in Figure 1. A monotonic increase with crater diameter is evident in this figure with a notable deviation from a cubic relation for craters larger than ten kilometers. Before proceeding with a discussion of the characteristics of this diagram and a comparison with lunar craters, it is necessary to determine the nature of the low density component(s) which give rise to these values of  $\Delta M$ .

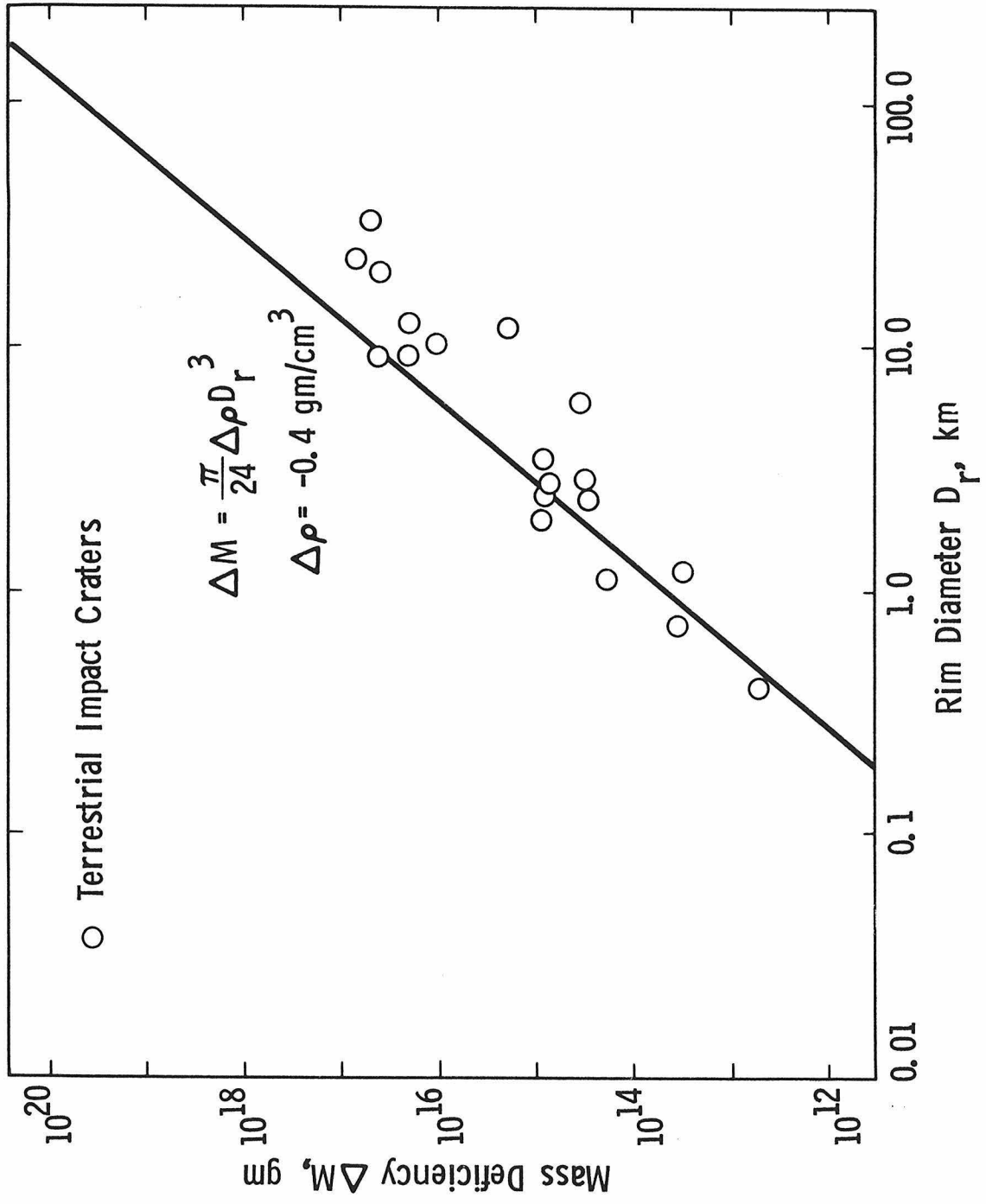
A consideration of the mechanics of the impact process, of the structure of terrestrial impact features, and of the morphology of lunar craters reveals four possible sources of low density material.

1. Material which has been ballistically transported, and subsequently well-mixed, and which has fallen back into the crater,
2. Raised rim structure which is comprised chiefly of ejected material from the crater,
3. Material, in lunar craters, derived by the large scale mass wasting or inward slumping of the interior crater walls, and
4. A lens of brecciated material within the crater which has been subjected to large strains, but which locally preserves the original stratigraphy and has not undergone ballistic transport.

An evaluation of the relative contribution of each of these four possible sources to the observed negative gravity anomalies of terrestrial impact craters will follow. This evaluation will be based



Figure 1. Variation of the mass deficiency,  $\Delta M$ , with crater rim diameter,  $D_r$ , for terrestrial impact structures. A cubic relation is shown by the solid line.



on results derived from the geophysical techniques previously described and from the examination of available drill hole samples and logs.

The first low density component listed above is material which has been ejected from the crater, but whose ballistic trajectories were insufficient to carry it beyond the rim. This interior fallback debris or mixed breccia unit has been identified at Meteor Crater (Shoemaker, 1963), Steinheim Basin (Reiff, 1977), and at several explosion craters. At Meteor Crater, this fallback debris unit exhibits the total range of shock histories and is composed of a mixture of rock fragments derived from all units revealed in the crater wall and of small fragments from the impacting object. Graded bedding of this unit is also evident at Meteor Crater. An estimate of the maximum thickness of this unit is ten meters at Meteor Crater and twenty to seventy meters at Steinheim Basin, that is, at most a fraction of one percent of the crater diameter. In terms of the mass anomaly, treating this component as a circular cylinder with a diameter equal to the crater rim diameter, the contribution to  $\Delta M$  will approximately be

$$\Delta M_{FB} \sim \Delta \rho \pi \left(\frac{1}{2} D_r\right)^2 \left(\frac{1}{100} D_r\right) = \frac{\pi}{400} \Delta \rho D_r^3 \quad (2)$$

where  $D_r$  is the diameter of the crater rim and  $\Delta \rho$  is the density contrast between the fallback unit and the undisturbed material. Impacts into unconsolidated materials, such as alluvial or eolian deposits, will change the porosity and, hence the density, very little. For competent target materials, the porosity of this well-fragmented and mixed unit may be expected to increase to 30%, so that, values of

$\Delta\rho$  ranging from zero to  $-1.0 \text{ gm/cm}^3$  may exist, dependent on the nature of the target material.

Application of the above estimate for the thickness of the fallback unit to lunar craters requires that this be amended for the effects of the difference in surface gravity,  $g$ , and for the absence of atmospheric drag on the ejected particles. The range of a ballistic trajectory is inversely proportional to the surface gravity so that the thickness of this fallback unit should be approximately proportional to  $g$ . The presence of an atmosphere will tend to reduce the range of a ballistic trajectory due to drag effects, so that, assuming flow similarity, for any given crater diameter, the effects of both gravity and atmospheric drag suggest that the thickness of this debris unit will be less on the Moon than on the Earth. Simple estimates for this drag effect are difficult since it depends in a nonlinear manner on particle size and shape and on ejected velocity (see McGetchin et al., 1974, for an illustration of evaluating this drag effect). Exclusion of this drag effect will give an upper bound on the amount of fallback material within a lunar crater.

$$\Delta M_{\text{FB}} < \frac{\pi}{400} \Delta\rho D_r^3 (g_{\text{Moon}}/g_{\text{Earth}}) \quad (3)$$

A second possible source of low density material is that comprising the crater rim structure. The surface relief of the rim is due both to ejected material and to uplifted country rock. Except possibly for a small region of maximum upward deformation near the rim crest this uplifted rock will probably be of insufficient porosity to

significantly contribute to the gravity anomaly. As evidence, a comparison of the recent gravimetric and seismic surveys of Meteor Crater (Regan and Hinze, 1975; Ackermann et al., 1975) is cited which show minor density and seismic anomalies associated with the fractured and uplifted bedrock of the rim. Overlying the uplifted bedrock is a thin layer ( $\sim 50$  m) characterized by a very low density and low seismic velocities. The thickness of this thin unit is approximately equal to that determined for the ejected material on the rim from drilling information (Roddy et al., 1975). In this work the volume of the rim ejecta is estimated by equating the volume of ejected material to the volume of the excavated crater. Following the geometric model of Pike (1967; 1976) for bowl-shaped impact craters on the Earth and the Moon, this volume is

$$V \sim \frac{\pi}{2} d \left(\frac{1}{2} D_r\right)^2 \quad (4)$$

where  $d$  is the actual depth of the crater measured from the pre-impact surface. For small lunar craters ( $D_r < 15$  km, Pike, 1977),

$$d \sim \frac{1}{5} D_r \quad (5)$$

so that, the mass anomaly contributed by the rim ejecta is

$$\Delta M_R \sim \Delta \rho \frac{\pi}{40} D_r^3 \quad (6)$$

The depth/diameter ratio for large lunar craters is less than that stated above for small craters,

$$d \sim \frac{1}{25} D_r \quad \text{to} \quad \frac{1}{50} D_r \quad (7)$$

so that, the volume of the crater bowl, and hence, the volume of the

surrounding rim, will be relatively less than that derived for the bowl-shaped craters. Taking into account this shallowing of large lunar craters, the expected contribution of the rim to the mass anomaly is

$$\Delta M_R \sim \frac{\pi}{200} \Delta \rho D_r^3 . \quad (8)$$

The third possible component of low density material associated with lunar craters is that resulting from the large scale mass movement or slumping of the crater interior suggested by the presence of scalloped and terraced walls (Mackin, 1969). This component has not been clearly recognized in terrestrial impact craters, probably due to the highly degraded state of these features. Orbital photographic identification of either impact melt or fallback debris overlying the lunar wall terraces at very young craters indicate that this inward collapse was a short term event (Hawke and Head, 1977). It is unknown whether this slumped component is distinct from the large lens of breccia underlying terrestrial impact craters, to be discussed next, or whether it is gradational with this breccia lens, representing a basic characteristic of larger impacts, and is not to be distinguished from it. Here this component will be treated separately to determine its contribution to the observed lunar gravity anomalies.

To estimate the amount of material resulting from the inward collapse of the crater walls, the existence of a transient cavity at the end of the excavated stage of cratering (see Gault et al., 1968) is postulated which, in this estimation, will be assumed to be

similar in form to the present parabolic form of the small bowl-shaped craters. The transient existence of a cavity at complex terrestrial craters is suggested by the reorientation of shatter cones at Sierra Madera and by the reconstruction of stratigraphic horizons at Gosses Bluff (Dence et al., 1977). At these two sites a depth/diameter ratio of 1/4 to 1/5 for this transient stage was estimated, roughly corresponding to the present depth/diameter ratio of bowl-shaped craters (Pike, 1977).

In this estimation the transient shape is reconstructed from the present shape by removing material from the center of the crater and building up the crater walls in a manner similar to that discussed by Settle and Head (1976) and Malin and Dzurisin (1978). This transient shape is assumed to be parabolic with a depth-diameter ratio of 1/5 and with a surrounding rim ejecta deposit which falls off with radial distance as  $(1/r)^3$  (McGetchin et al., 1973). The present shape is idealized to be a flat-floored crater with a constant interior slope. Given the present crater floor diameter,  $D_f$ , rim diameter,  $D_r$ , rim-to-floor depth,  $d_i$ , and rim height,  $d_e$ , the diameter of the transient cavity,  $D_o$ , will be

$$D_o = \frac{5}{2} D_r^3 d_i (\eta^2 + \eta + 1 - 3\xi)^{1/4} \quad (9)$$

where  $\eta = D_f/D_r$  (10a)

and  $\xi = d_e/d_i$  (10b)

For most large lunar craters (Pike, 1976),

$$\eta \sim 0.7 \quad (11a)$$

$$\xi \sim 0.2 \quad (11b)$$

$$\text{and } d_i \sim \frac{1}{25} D_r \quad (12)$$

$$\text{so that } D_o \sim 0.6 D_r \quad (13)$$

$$\text{and } (d_o - d_i) \sim 0.1 D_r \quad (14)$$

where  $d_o$  is the depth of the transient cavity. Then the contribution to the mass anomaly will be, assuming a parabolic geometry,

$$\Delta M_s \sim \Delta \rho \frac{\pi}{2} \left(\frac{1}{2} D_r\right)^2 \left(\frac{1}{10} D_r\right) = \frac{\pi}{80} \Delta \rho D_r^3 \quad . \quad (15)$$

The three low density components already considered, expressed in eqs. (3), (8), and (15), will be shown to be relatively minor contributions to the gravity anomalies associated with terrestrial impact craters. The major contribution is due to a large lens of brecciated and crushed material underlying the crater and laterally confined to lie within the crater rim crest. This component is characterized by moderately shocked material which has undergone relatively little mixing of the pre-existing strata. Drill logs of this region in terrestrial craters show a general correlation between density variations and the degree of shock damage (Short, 1970). Near the center of the crater the vertical distribution of shock effects is erratic with maximum shock damage near the top and bottom of the breccia unit and with the intensity of shock damage falling off rapidly toward the rim. There is very little small scale mixing of lithologic units in this breccia lens. A melt zone, sometimes containing iron-nickel fragments, found near the basal portion of



this unit and confined to the center at Brent Crater (Dence, 1965), Meteor Crater (Shoemaker, 1963), Lonar Lake (Fredriksson et al., 1973), and West Hawk Lake (Short, 1970), is interpreted as the maximum depth of the transient cavity formed at the end of the excavation stage in the cratering process. The vertical distribution of shock effects and the presence of the basal melt zone, but the lack of small scale mixing, indicates that the material which comprises this breccia lens flowed or heaved outward and returned before the final deposition of the fallback mixed breccia unit (Shoemaker, 1963).

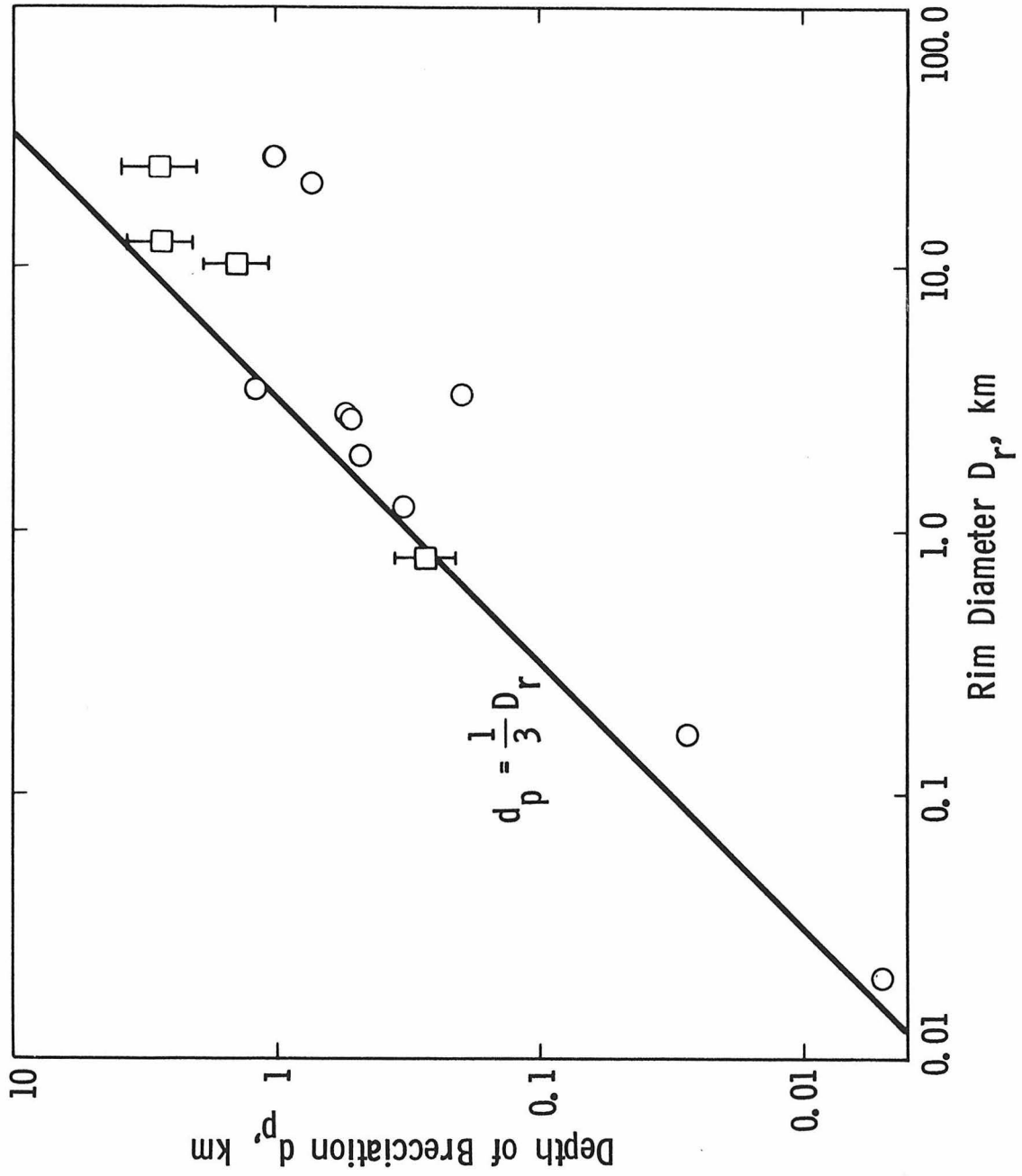
No comparable basal melt zone has yet been identified at complex craters, probably due to the disruption which occurred during the creation of the central uplift. The timing of the formation of the central uplift was short-term and preceded the raining down of the fallback mixed breccia, as is suggested at Steinheim Basin (Reiff, 1977) and at Gosses Bluff (Milton et al., 1972). However, it is not clear whether the central uplift is due to a rebound response of the target to the passage of the shock and rarefaction waves (e.g., Milton et al., 1972) or due to gravitational collapse (Dence, 1968).

For some very large terrestrial impact features, there is an annulus of brecciated material instead of a central lens which surrounds the uplift (e.g., Manicouagan, Sweeney, 1978). Present studies have not determined whether this annulus is due to ejecta fallback (i.e., mixed breccia) or is analogous to the lens of breccia associated with smaller impact features.

The depths of brecciation as measured from the pre-impact surface have been determined for many terrestrial impact features and are listed in Table III. Most of these determinations are based on information obtained from drill holes near the center of the structure or, for the two smallest craters, from trenches. However, for three craters in this list - which includes one lunar crater at the Apollo 17 landing site - for which this depth was estimated, drilling information was not available. In these cases, seismic data were used. As mentioned earlier, the low seismic velocity region associated with an impact feature is not confined to the lens of severely brecciated material, but extends beyond and includes the surrounding fractured region. The extent of this fractured region is two to four times the extent of the brecciated unit at Meteor Crater (Ackermann et al., 1975) and at Deep Bay (Sander et al., 1964). Using this as a rough approximation, the depths of brecciation have been estimated, within an uncertainty of a factor of two, for these three craters from the available seismic data and are noted in Table III.

All of these depths of brecciation are plotted versus crater diameter in Figure 2. Notice that most of the small craters ( $< 10$  km) fall along a line defined by a constant depth/diameter ratio of approximately one-third. The notable exception is the Flynn Creek Structure (3.8 km diameter). Small deviations about this line may be due to erosion or to variations in the impact velocity and angle or to different meteorite and target material properties at the various sites. Using this value of one-third, the mass anomaly contributed

Figure 2. Maximum depth of brecciation versus crater diameter. Circles denote depths determined by drilling; squares denote depths determined by seismic surveys, corrected for the deeper extent of these seismic determinations (see text).



by this lens-shaped brecciated component will be

$$\Delta M_B \sim \Delta\rho \frac{\pi}{2} \left(\frac{1}{2} D_r\right)^2 \left(\frac{1}{3} D_r\right) = \frac{\pi}{24} \Delta\rho D_r^3 \quad . \quad (16)$$

A comparison of the above expression with eq. (3), (8), and (15) confirms the earlier statement that this component is the major contribution to the negative Bouguer anomalies associated with terrestrial impact craters.

The density contrast between this breccia lens and the surrounding rock will be less than that for the fallback units discussed earlier since this component is much less shocked and mixed. An upper bound of  $-0.5 \text{ gm/cm}^3$  is placed on acceptable values for the density contrast based on the largest values determined for this unit in terrestrial impact features (see Table III). This bound corresponds to a maximum increase in porosity of 20%. Equation (16) is shown in Figure 1 with  $\Delta\rho$  equal to  $-0.4 \text{ gm/cm}^3$ .

The larger terrestrial impact features ( $> 10 \text{ km}$ ) plotted in Figure 2 fall systematically below the linear trend defined by the small terrestrial craters. A similar deviation from the cubic relation between crater mass deficiency and diameter defined by the small terrestrial craters also begins at a diameter of ten kilometers in the plot of  $\Delta M$  versus crater diameter shown in Figure 1. Some of these larger terrestrial features are multiringed structures. In these cases, the apparent shallowness is possibly due to the choice of a crater diameter which corresponds to an outer ring of the structure, but which does not correspond to the actual crater rim. This is

probably the case for Ries Basin. For this feature the diameter listed in Table III is that for the major circular topographic depression. However, a less conspicuous inner ring, eight to ten kilometers in diameter, is more in line with the linear trend in Figure 2 and the cubic trend in Figure 1. Further support for this inner ring representing the actual crater rim at Ries Basin is inferred from the inverted stratigraphy identified in drill holes between the ten and twenty-two kilometer diameter rings, evidently part of an exterior ejecta blanket (Dennis, 1971). Unfortunately, similar detailed drilling information is not available for the other large terrestrial impact features.

In summary, gravimetric surveys of terrestrial impact structures show that a negative anomaly, that is, a low density region, is associated with most of these features. Surface geology together with drilling information indicates that these gravity anomalies are primarily due to a lens of brecciated material confined within the crater rim and extending vertically to approximately a depth of one-third the crater diameter. The maximum density contrast between this unit and undisturbed country rock is  $-0.5 \text{ gm/cm}^3$ . Other low density components associated with impact structures were described in this chapter and will be considered in the evaluation of the gravity anomalies associated with young lunar craters.

## LUNAR GRAVITY AND TOPOGRAPHIC DATA

The lunar gravity and topographic data are discussed in this chapter along with a description of the procedure used in computing the topographic contribution to the local gravity field and the model calculations to the Bouguer gravity. Included within this discussion will be an outline of the uncertainties in determining the lunar gravity field contributed by the surface topography and by proposed models for the subsurface density structure.

Lunar Gravity Data

The Doppler shift of a transponded radio signal from a spacecraft in lunar orbit as measured by the Earth-based tracking system is directly proportional to the relative line-of-sight (i.e., Earth-to-spacecraft) velocity component of the spacecraft. The details of making these measurements and deriving acceleration values from them are given by Sjogren et al. (1972b; 1976) and will only be summarized here.

The resolution of these Doppler shift measurements is approximately 0.01 Hz which, at an operating frequency of 2300 MHz, corresponds to a change in spacecraft velocity of 0.65 mm/sec. For most orbits the sampling rate is usually chosen to be ten seconds, though for some orbits sampling rates ranging from one to thirty seconds are used. For each orbit an initial state, consisting of the six orbital parameters (i.e., three positional and three velocity components) are

estimated from these Doppler measurements by a least-squares procedure for a model which includes perturbations by the Earth and Sun, Earth rotation, and finite signal transit time and takes into account the presence of a third order lunar gravity field. The choice of the order of this lunar gravity field for this analysis is unimportant as long as the resolution of this global field is much larger than the scale of the features being examined (see Gottlieb et al., 1970). The resulting Doppler residuals, which may amount to as much as 20 Hz, are primarily due to unmodeled variations in the lunar gravity field. The errors incurred in correcting the original Doppler measurements and in determining the orbital parameters are generally less than 0.003 Hz (Phillips et al., 1978).

The line-of-sight accelerations are derived from the residual Doppler values by differentiating with respect to time an analytic patched cubic spline to the Doppler residuals. The choice of a spline window which is too large will have systematic second-order residuals while a window which is too small may fit the data perfectly but have severe excursions (ringing) between data points. It has been determined that a thirty second spline window produces second-order residuals which are comparable to the 0.01 Hz resolution limit of the Doppler measurements (Phillips et al., 1978).

The major sources of error in the determination of the line-of-sight gravity values are the noise associated with receiver phase jitter, troposphere and ionosphere effects, quantization error, antenna



variations, and timing errors, and is typically less than 0.01 Hz for a ten second sample rate (Phillips et al., 1978). This estimate has been substantiated by examination of the Doppler measurements during the trans-Earth stage when the spacecraft motion is not influenced by small scale variations in the lunar gravity field. The contribution of this high frequency noise to the determination of the lunar acceleration values is derived from an examination of the second-order residuals remaining after the spline fit to the Doppler residuals and is used as the basis for estimating the formal error of the lunar gravity values (Phillips et al., 1978). A standard six-point numerical operation has been used in this estimation to time difference these second-order Doppler residuals (Milne-Thomson, 1951)

$$\begin{aligned}
 s f'(x) &= \frac{1}{6} \left[ f(x + 3s) - f(x - 3s) \right] \\
 &\quad - \frac{3}{4} \left[ f(x + 2s) - f(x - 2s) \right] \\
 &\quad + \frac{3}{2} \left[ f(x + s) - f(x - s) \right]
 \end{aligned} \tag{17}$$

where 's' is the sampling rate and the prime denotes the derivative. For a ten second sample rate, accelerations of order ten milligals are typical for this noise source.

Since these acceleration values are the line-of-sight component of the lunar gravity field, they contain both a local vertical and horizontal component. The effect of this will be to modify the gravity signature as one moves from the sub-Earth point, where the line-of-sight component is predominantly vertical, toward the limb, where this component is predominantly horizontal. This change is illustrated in

Figure 3. Note that this geometric effect tends to position the peak in the gravity anomaly away from the center of the feature which gives rise to the anomaly and toward the sub-Earth point.

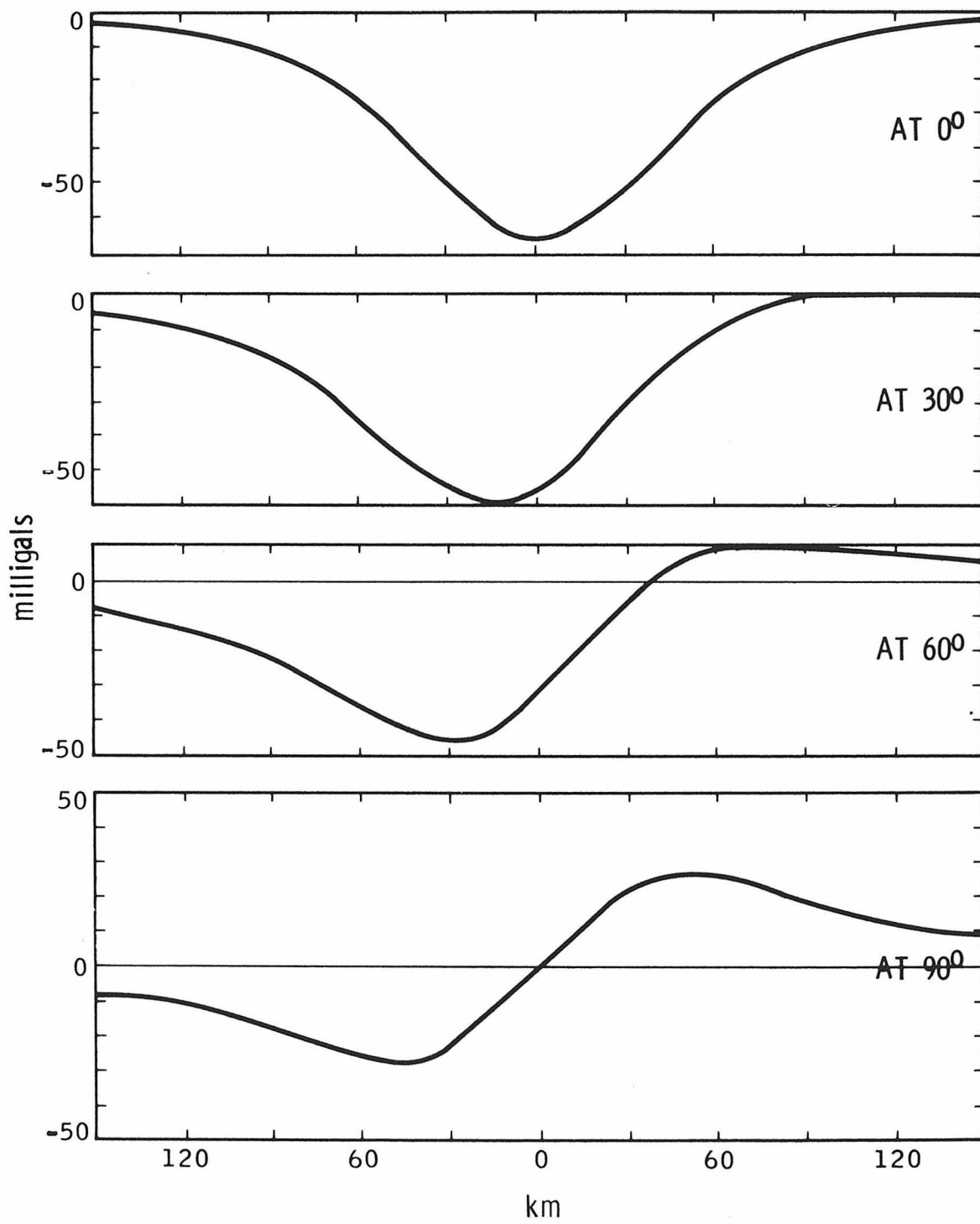
The accelerations derived from the Doppler residuals are termed the *free-air* gravity and are due to the combined gravitational effect of the lunar surface topography and lateral density variations within the Moon. The small scale of the gravity anomalies analyzed in this work requires that the lateral density variations which give rise to these anomalies reside within the lunar crust. Deeper density variations will give rise to broader anomalies than those considered here. Furthermore, due to the small scale of these anomalies, only the relative change in gravity, appropriate to the wavelength character of the feature of interest, is considered here, not the absolute value which is, in part, related to the broader regional structure of that portion of the Moon.

#### Lunar Topographic Data

The best determination of detailed local topography on the Moon comes from the Apollo Control Network (ACN), which includes the laser altimetry data (Kaula et al., 1973;1974), and from the Lunar Topographic Orthophotomaps (LTO) produced from the photography of the Apollo metric camera system. Unfortunately, dual areal coverage of these sources of lunar topographic data and of low altitude spacecraft gravity data is very limited so that additional coverage of detailed lunar topography is necessary to fully utilize the existing low altitude gravity data. This has been provided by the Earth-based radar topographic (ERT) maps of Zisk (1972a).

Figure 3. Change in the line-of-sight gravity signature for a ninety kilometer crater as one moves along the lunar equator from the sub-Earth point ( $0^{\circ}$ ) to the eastern limb ( $90^{\circ}$ ).

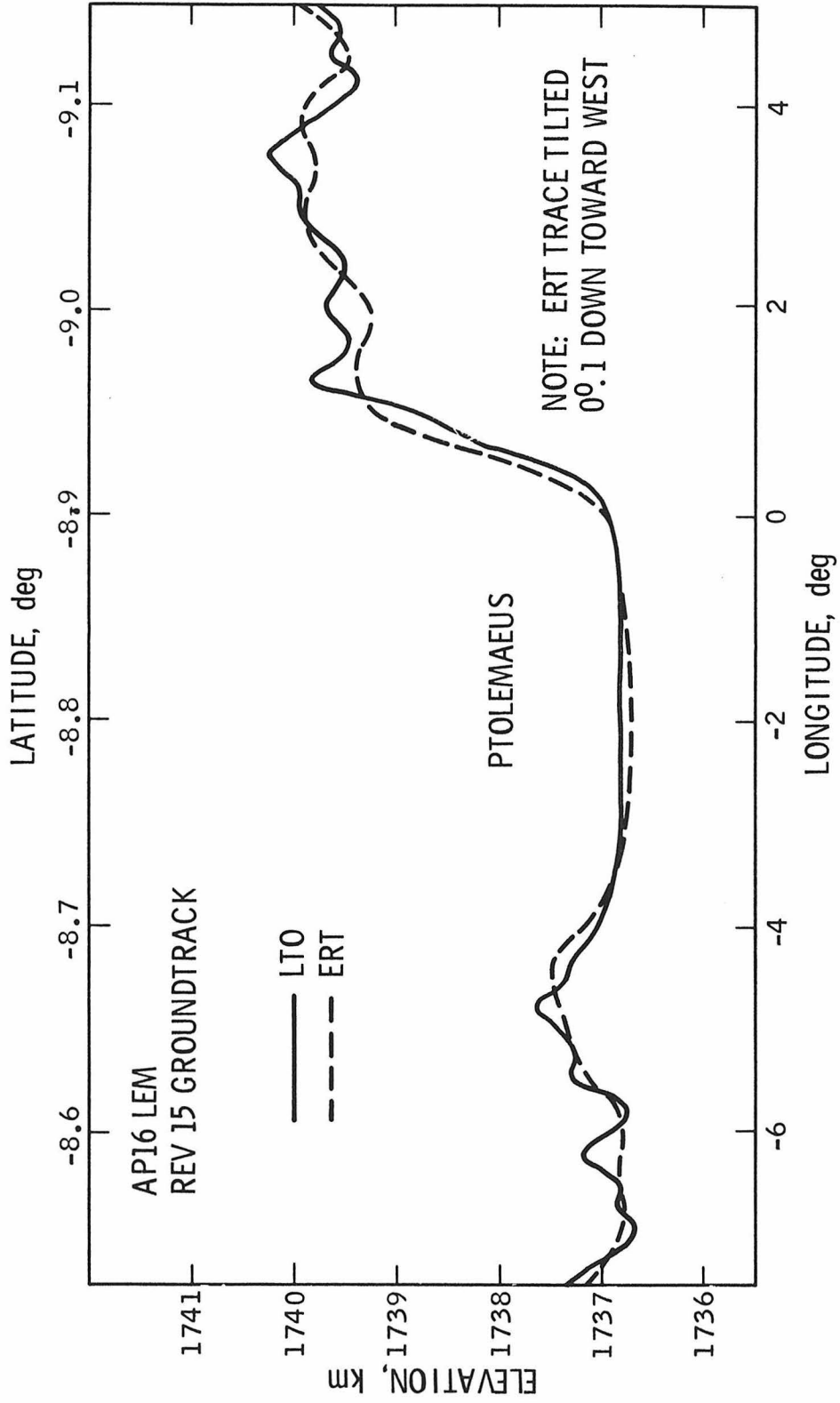
## GRAVITY vs LONGITUDE



The radar method makes use of an interferometer technique to measure relative relief over most of the lunar nearside, extending up to 80 degrees from the sub-Earth point. Location on the lunar surface of a returned echo is determined by using constant range rings and Doppler strips which have an approximate resolution of one-by-two kilometers on the lunar surface. The phase displacement measured between two interferometer antennas for the returned echo from the same resolution element is used to determine the relative relief over a localized region ( $\sim 400$  km diam) of the Moon (Shapiro et al., 1972; Zisk, 1972b). Topographic maps derived by this procedure are shown in Figures 26 (p. 143) and 31 (p. 172). Two difficulties with this method are the suppression of topographic features comparable to or smaller than the resolution elements by averaging over the resolution size and the inability of the presently available lunar ephemeris to tie these radar data to an absolute lunar topographic datum level. The latter difficulty will introduce regional slopes in the ERT data of typically 1:200 to 1:400 (Zisk, private communication).

An error analysis of the ERT data shows that relative heights can be determined by the radar method to an accuracy of  $\pm 200$  meters (Shapiro et al., 1972; Zisk, 1972b). A comparison of topographic profiles across Ptolemaeus determined by LTO and ERT data sets is shown in Figure 4. An arbitrary datum and a regional slope of 1:300 have been added to the ERT profile. From this figure

Figure 4. A comparison of relative elevations determined from the Lunar Topographic Orthophotomaps (LTO) and the Earth-based Radar Topographic (ERT) data across the crater Ptolemaeus. The elevations read from the LTO maps are referenced to the center of mass of the Moon. A linear trend was removed from the ERT trace before it was superimposed on the LTO trace.



it can be seen that the ERT trace recovers the basic features of this topographic profile but fails to record the irregular small scale variation. Another comparison of the LTO and ERT profiles is shown in Figure 5 across a deeper lunar crater, Langrenus, which lies nearer the lunar limb than Ptolemaeus. Again, an arbitrary datum has been added to the ERT profiles in this figure, but no regional slope has been introduced in this comparison. The ERT data again recovers the basic topographic features but fails to record the small scale variations; in particular, note the suppressed rim crests and the smoothing of the central peak.

A final comparison of the ERT data with other lunar topographic sources, in this case, LTO, photogrammetry, and shadow measurements, is shown in Figure 6. In the upper diagram, plotted as a function of the crater rim diameter, is the difference in crater rim-to-floor depths determined by Pike (1976) from these other topographic sources and determined by the ERT data and in the lower diagram is the difference in the actual crater depths determined by Pike and by the ERT data for these same craters. These values are tabulated along with a listing of the crater names in Table IV. The large difference exhibited in the upper diagram is due primarily to the suppression of the crater rim crest by the ERT technique, evident in the crater profile shown in Figure 5. This effect has been essentially removed by considering the actual crater depths in the lower diagram. However, there still remains for the smaller craters a 200 to 400



Figure 5. A comparison of the relative elevations determined from the LTO maps and the ERT data across Langrenus. Elevations read from the LTO maps are referenced to the center of mass of the Moon. An arbitrary constant background level was added to the ERT traces.

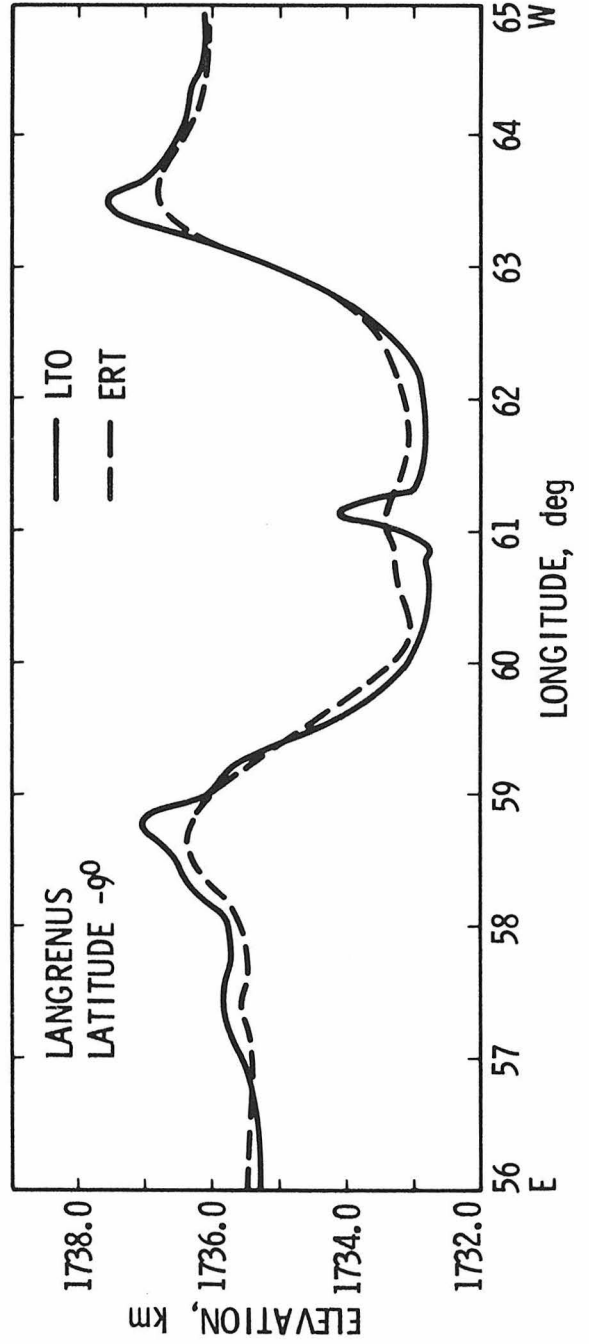
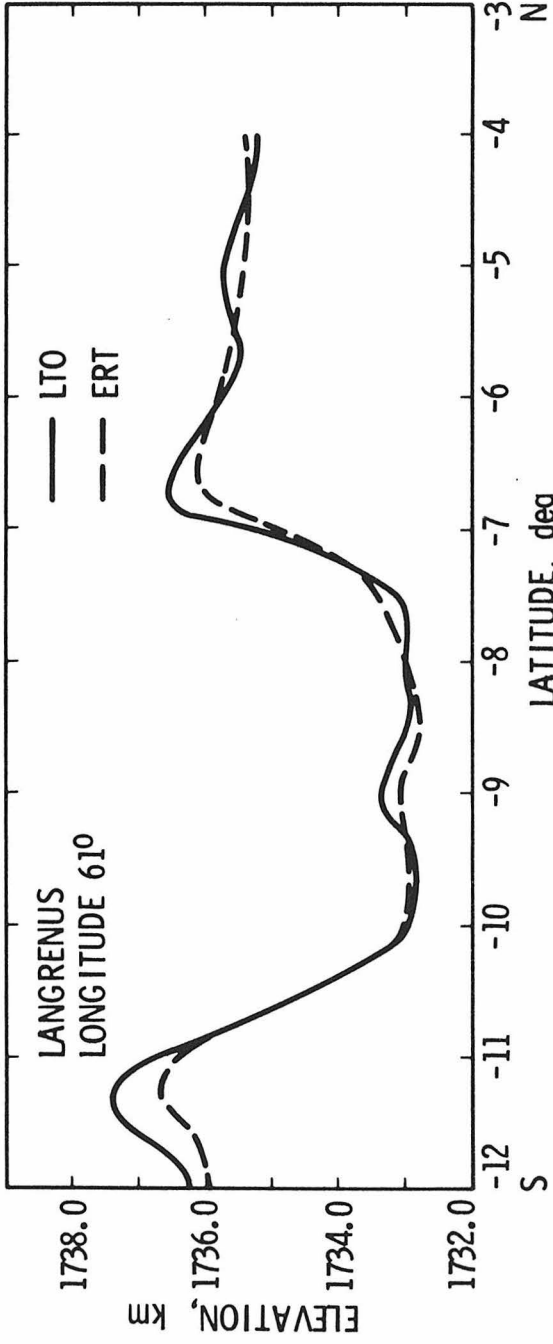


Figure 6. A comparison of crater depths determined by the Earth-based Radar Topographic data (ERT) with crater depths determined by other methods and reported by Pike (1976). The difference in the determination of crater depths are shown as a function of the logarithm of the crater diameter. The solid points denote crater depths determined by Pike from either LTO maps or USGS photogrammetry. The open circles are shadow measurements. In the upper diagram are differences in rim-to-floor depths and in the bottom diagram are differences in the actual crater depths. The larger scatter in the upper diagram is due to a suppression of the rim crest elevations by the radar technique.

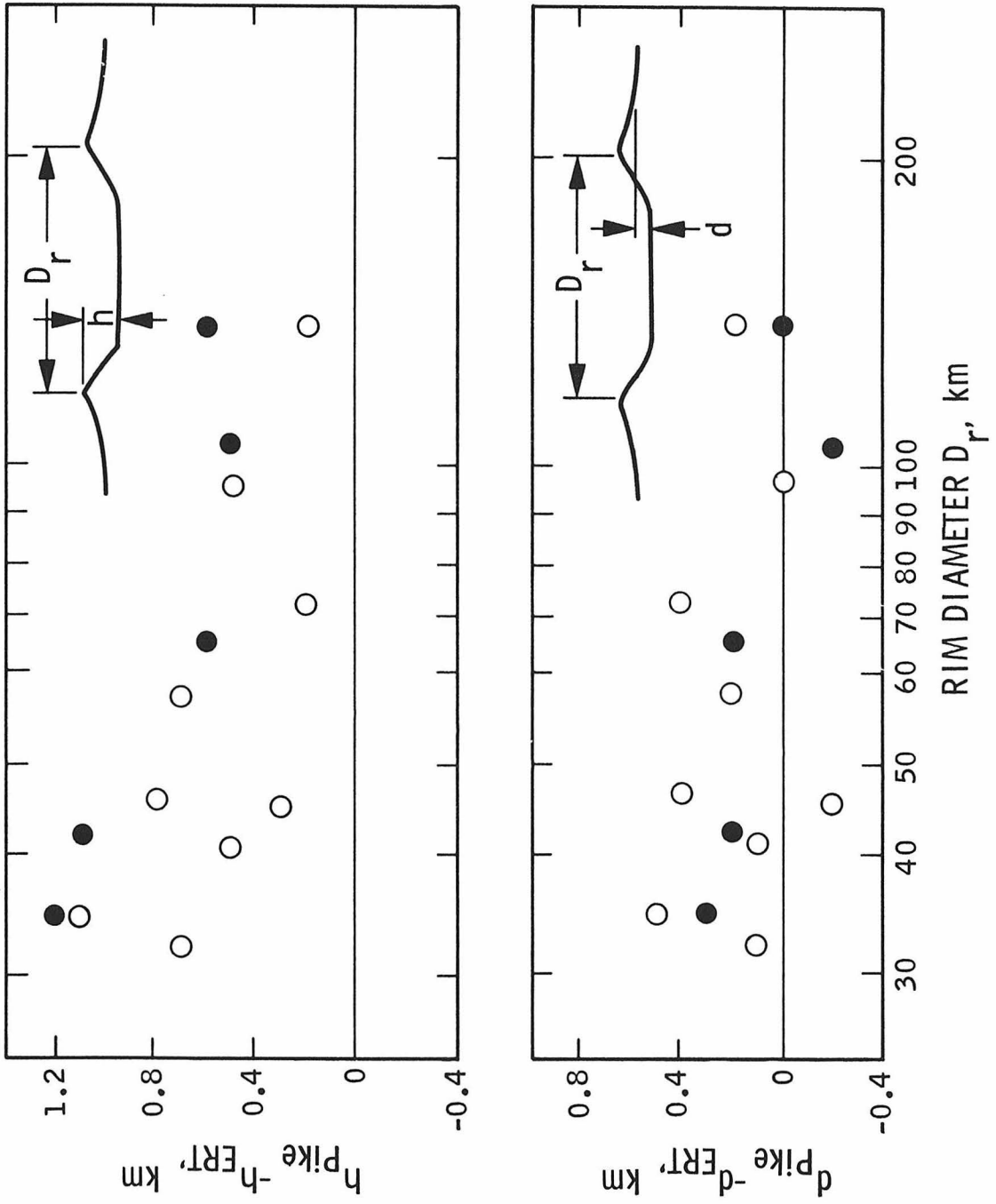


TABLE IV

## COMPARISON OF CRATER DEPTH DETERMINATIONS

Pike (1976) vs. Zisk (Radar)

<u>Crater Name</u>	<u>Diam. (km)</u>	<u>Rim-to-Floor</u>		<u>Surroundings-to-Floor</u>	
		<u>Pike</u>	<u>Zisk</u>	<u>Pike</u>	<u>Zisk</u>
*Langrenus	136	4.5	3.9	3.0	3.0
Albatengnius	135	3.2	3.0	2.2	2.0
*Theophilus	102	4.1	3.6	2.8	3.0
Copernicus	93	3.8	3.3	2.7	2.7
Werner	71	4.2	4.0	3.4	3.0
*Macrobius	65	4.0	3.4	2.8	2.6
Eratosthenes	58	3.4	2.7	2.0	1.8
Agrippa	46	3.0	2.2	2.2	1.8
Reinhold	45	2.7	2.4	1.9	2.1
*Herschel	42	3.3	2.2	2.4	2.2
Marius	41	1.5	1.0	0.9	0.8
*Tisserand	35	2.9	1.8	1.9	1.6
Godin	35	3.2	2.0	2.5	2.0
Kepler	32	2.7	2.0	1.9	1.8

\* Denotes use of either LTO maps or USGS photogrammetry by Pike (1976).

In all other cases shadow measurements were used.

meter bias in the ERT determination of the crater floor level; for large craters (>90 km) there is no detectable systematic bias in the determination of actual crater depths by the ERT technique and by other sources. The 200 meter accuracy of the ERT data, which for small lunar craters is a 400 meter bias, is a major source of error in the analysis of the lunar gravity anomalies and has been included in estimating the uncertainty in determining the Bouguer gravity. For a two kilometer deep crater, the uncertainty in topography will contribute roughly ten per cent to the determination of the Bouguer gravity.

#### Orbit Simulation Procedure

The least-squares estimate of the orbital parameters is the major step in the reduction procedure described earlier which introduces a significant nonlinear corruption of the Doppler residuals, and hence, lunar gravity values. This least-squares orbit estimation will absorb ten to thirty per cent of the magnitude of the high frequency gravity field and will cause, in the residual gravity values, spurious negative (positive) accelerations to flank positive (negative) anomalies (Gottlieb, 1970). The amount of this compression is variable for each feature, dependent mainly on the distance of the anomaly from the sub-Earth point with less compression for features nearer the limb, and must be accounted for in any computational scheme which is used to model the lunar gravity values. However, the inclusion of the full details of the data reduction procedure in a modeling scheme, taking into account the relative motion of the spacecraft and the Earth-based

tracking system, the effect of the Earth and the Sun, etc., to compute the Doppler residuals is a very costly procedure. To circumvent this difficulty a simplified orbit simulation procedure has been developed which takes into account, in an approximate manner, the nonlinear bias introduced by the least-squares estimate of the orbital parameters and which allows comparisons to be made directly with the derived lunar gravity values but is able to ignore the remaining details of the data reduction procedure (Phillips et al., 1978).

In this orbit simulation procedure, a density distribution is specified,  $\rho(r, \theta, \phi)$ , where  $r$ ,  $\theta$ , and  $\phi$  are radius, latitude and longitude, respectively, in a Moon-centered spherical coordinate system. The resultant gravity field is obtained by integrating the product of  $\rho(r, \theta, \phi)$  and the spherical Green's function over a prescribed volume of the Moon

$$g(x, y, z) = \text{GTV} \int_{V'} \frac{\rho(r', \theta', \phi') r'^2 \cos \theta' d\theta' d\phi' dr'}{\left\{ r^2 + r'^2 - 2r'(\cos[\phi - \phi'] \cos \theta \cos \theta' + \sin \theta \sin \theta') \right\}^{\frac{1}{2}}} \quad (18)$$

where  $G$  is the gravitational constant and  $\nabla$  is the gradient operator. The unprimed coordinates are the spacecraft position as previously determined by the orbit determination procedure. This volume integration is first carried out analytically in longitude, numerically in latitude and then radially integrated numerically.

The resultant gravity vectors are rotated by the transform matrix  $\bar{T}$  into the standard lunar Cartesian coordinate system, and then read

as a "force table" in an orbit simulation program. A simplified numerical integrator is used in this program (without perturbations from the Earth or the Sun, station motion, or signal transit time calculation) to simulate the Doppler measurements, integrating in the presence of the "force table". The line-of-sight component is approximated by the line connecting the center of masses of the Earth and the Moon taking into account the lunar librations. The Doppler values are then fit in the least squares sense with a Keplerian orbit. This processing approximately reproduces the same distortion in the simulated Doppler values as are imposed on the real data. These simulated Doppler residuals then undergo the same cubic spline fitting procedure as the real data in computing the accelerations. The use of the simplified numerical integrator to compute the Doppler measurements as well as the fitting with a conic rather than an integrated orbit in this procedure introduces long-term biases in the Doppler residuals and in the position of the spacecraft but does not significantly change the character of the high frequency gravity due to local features (Phillips et al., 1978). Positional biases of the spacecraft along the orbital track introduced by the above approximate simulation procedure may amount to as much as ten kilometers, so that modeled gravity profiles computed in this manner must be freely matched to the minimum or maximum of the observed gravity profiles within this range of uncertainty.

#### Bouguer Gravity

The Bouguer gravity is determined by differencing the topographic contribution to the gravity field from the free-air gravity. This



topographic contribution is determined by use of the orbit simulation procedure described in the previous section in which the density distribution is taken to be the observed surface height variations derived from one of the sources of local lunar topography discussed earlier. In the analysis of lunar craters, the major contribution, in most cases, is due to the central bowl of that particular crater.

The exact choice of the topographic background level is of little importance in this analysis of localized gravity anomalies as long as the edge effects of the topographic model are insignificant, that is, the topographic model must extend a few times the spacecraft altitude beyond the feature of interest. The effect of this choice of the topographic datum is shown in Figure 7 for a gravity profile across the crater Langrenus. Both of these two curves are the contribution of the surface topography to the local gravity field differing only in the choice of the topographic background level. As can be seen in this figure, the signature and amplitude of these profiles are almost identical. The major difference is in the absolute value of the accelerations indicating that a much larger wavelength component, as expected, is being altered by a change in the topographic datum.

The choice of the value for the lunar crustal density used in the topographic correction also has a small effect on the determination of the Bouguer gravity. To illustrate, the free-air gravity data for an orbital pass across Langrenus is shown in Figure 8. The solid lines are the topographic contribution parameterized by assumed values for the crustal density ( $\text{gm/cm}^3$ ). It is seen that the choice of crustal

Figure 7. Effect of changing the topographic background level for the same orbital pass. The two solid lines show the topographic contribution to the gravity field for two different datum levels measured in kilometers from the center of the Moon.

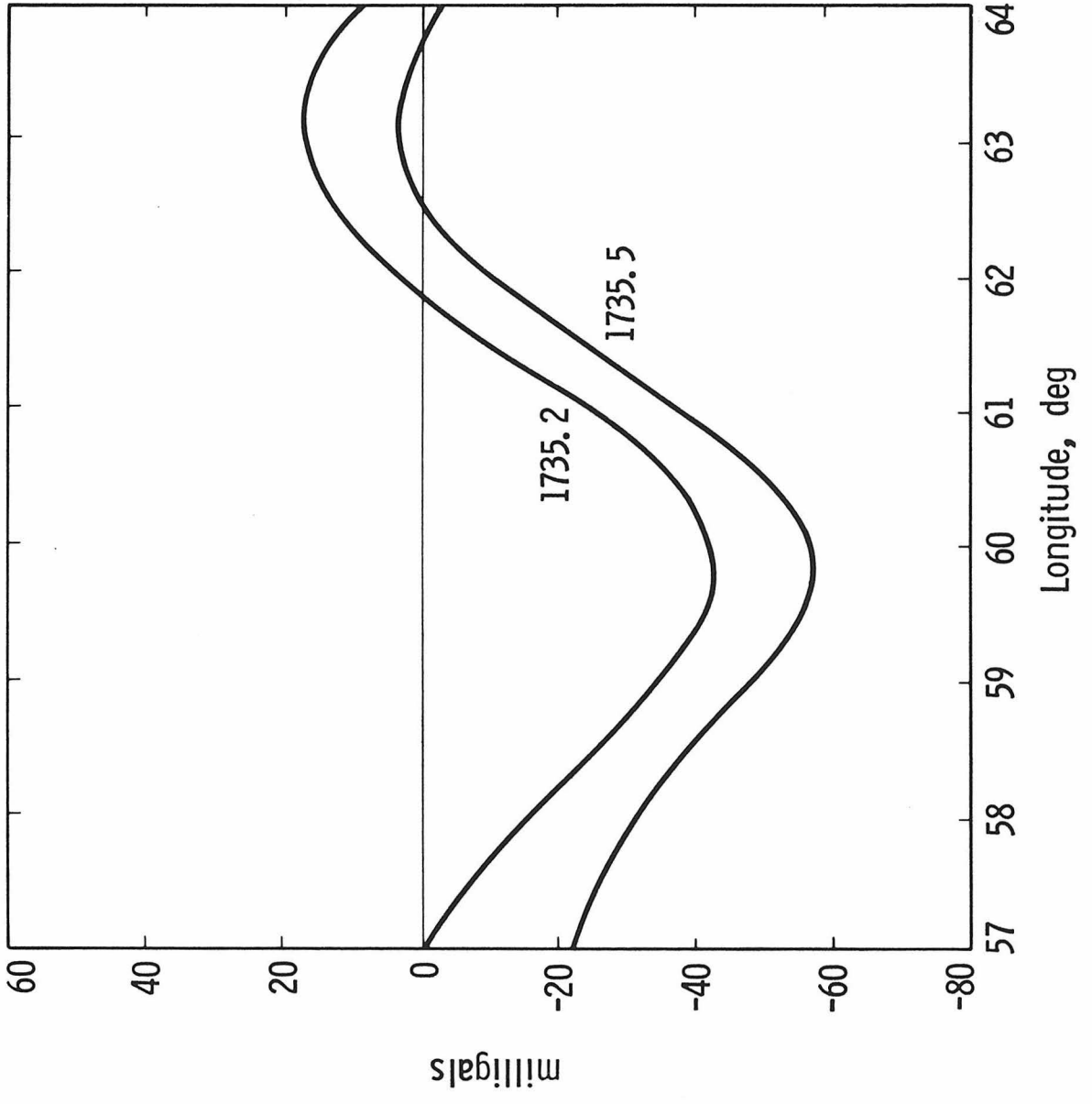
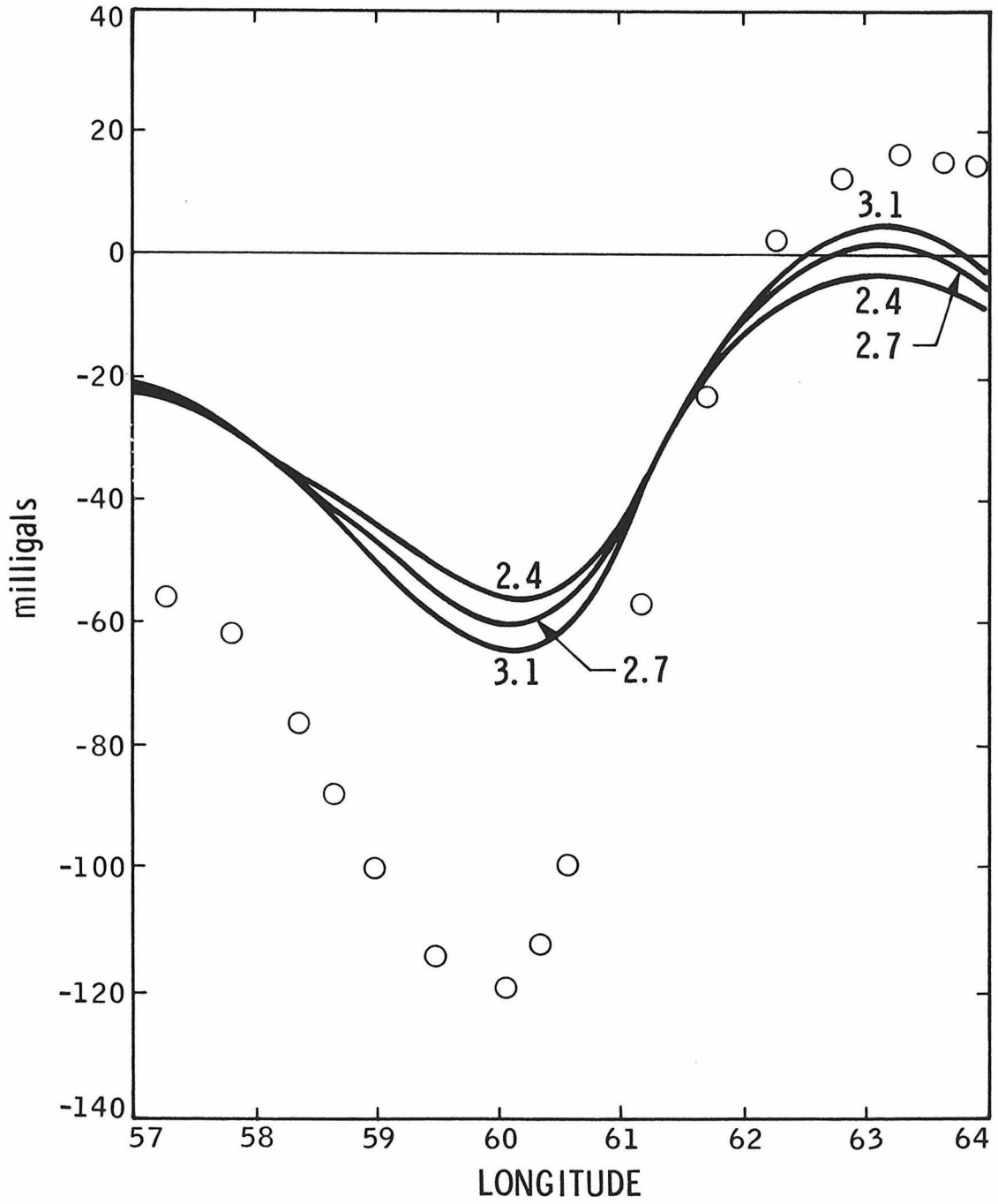


Figure 8. Dependence of the topographic correction on assumed values for the lunar crustal density. The circles are the free-air gravity data and the solid lines are the topographic contribution to the gravity field parameterized by assumed values for the lunar crustal density ( $\text{gm/cm}^3$ ).

# LANGRENUS APOLLO 16 REV 4



density is not critical, and in this particular example, is incapable of matching the peak-to-peak variation in the free-air gravity. For all lunar craters, a value of  $2.7 \text{ gm/cm}^3$  has been adopted for the lunar crust. This is close to the median value determined by Talwani et al. (1973) for returned samples of the lunar anorthositic highlands and to the value of  $2.9 \text{ gm/cm}^3$  determined for the lunar Apennines by Ferrari et al. (1978) from spacecraft gravity data. For the two non-impact features included in this analysis, which are probably chiefly composed of material similar in composition to the lunar mare that surrounds them, a higher value of  $3.0 \text{ gm/cm}^3$  has been adopted in computing the Bouguer gravity. This higher density is consistent with measured values determined for samples returned from the lunar mare regions (Talwani et al., 1973).

The resultant Bouguer gravity profiles for each of the lunar features considered in this work are presented in the Appendix. For each feature the groundtracks of most of the orbits analyzed are shown in the upper diagram and the free-air (solid lines) and Bouguer (dashed lines) gravity profiles are shown beneath as a function of longitude. The Bouguer gravity has an arbitrary background level. The error bars shown along the Bouguer profiles are the square root of the sum of the squares of the uncertainties in the determination of the Bouguer gravity (averaged in approximately one degree longitude increments) contributed from uncertainties in the topography, in the assumed value for the lunar crustal density ( $\pm 0.3 \text{ gm/cm}^3$ ), and in the intrinsic noise of the Doppler data. These various contributions for the lowest altitude

orbit analyzed over the center of each feature are listed in Tables V, VI, and VII (pp. 73, 88, 128, respectively). Not included in the estimation of these error bars, but listed in these tables and included in the estimation of  $\delta g$ , is an estimate of the objective uncertainty in extracting the gravity signature of the feature of interest from the regional background level. This uncertainty will also be included in constraining the range of acceptable model calculations.

Two techniques have been used to try to model this regional background level, but with poor results. The first was the use of the spherical harmonic expansion of the lunar gravity field (Ferrari, 1977) applied to the orbits analyzed here. The difficulty with applying this harmonic expansion is that the downward continuation of the gravity field did not always adequately reproduce the regional trend of the free-air gravity. The second technique used a point model for the nearside lunar mass distribution (Wong et al., 1971). The difficulty here is that the point model specifically included many of the lunar features which are being analyzed here, and as such, the regional background field determined from this point model absorbed some of the gravity signature arising from the feature of interest. As a result of these difficulties, neither technique was used.

#### Model Calculations

Many of the lunar features analyzed here have detectable Bouguer anomalies (see Appendix). The interpretation of these Bouguer anomalies is hampered by the inability to invert gravity data in terms of a

unique density structure. However, the determination of the total mass deficiency or excess,  $\Delta M$ , giving rise to the Bouguer anomaly is, within the uncertainties of this analysis, independent of the density structure. Using this mass parameter, various hypotheses regarding the nature of the anomaly can be tested by prescribing the geometry of the anomalous mass and solving for the density contrast required to reproduce the observed Bouguer gravity anomaly. For the lunar craters, models are proposed on the basis of the generalities made about terrestrial impact features in the previous chapter. Those models which require an unrealistically large density contrast are eliminated as possible solutions. Ranges of realistic values for the density contrast will be discussed when appropriate in the following chapters. For the non-impact features, the Bouguer gravity is used to limit the lateral spatial extent, and hence, constrain the geometry of the anomalous mass which can then be related to surface features. In the analysis of Grimaldi, a single anomalous mass component does not adequately reproduce the observed gravity signature, so that multiple components are introduced.

To illustrate the independence in determining  $\Delta M$ , four paraboloidal models are proposed to explain the negative Bouguer gravity across Copernicus. A detailed description of the rationale for these models with respect to the crater shape is given in the next chapter and a sketch of each model is shown in Figure 9. The appropriate dimensions of each of these models for Copernicus are listed in Figure 10 along with the density contrast ( $\text{gm/cm}^3$ ) necessary in each case to reproduce the

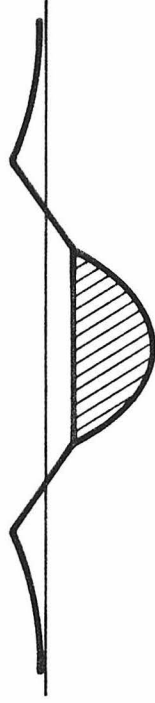


Figure 9. Schematic diagram of four models for the mass deficiencies associated with young lunar craters. Dashed line outlines the postulated transient crater geometry used in estimating the thickness of the slump models (see Chapters II and IV).

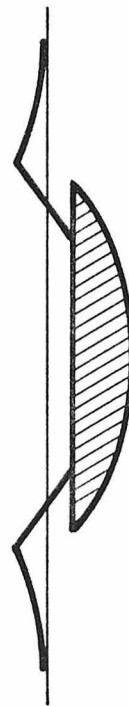
1. SLUMP MODEL A



3. BRECCIA LENS A



2. SLUMP MODEL B



4. BRECCIA LENS B

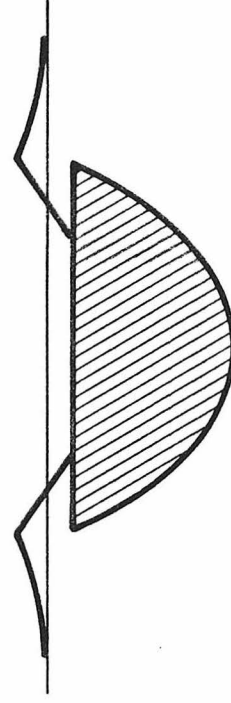
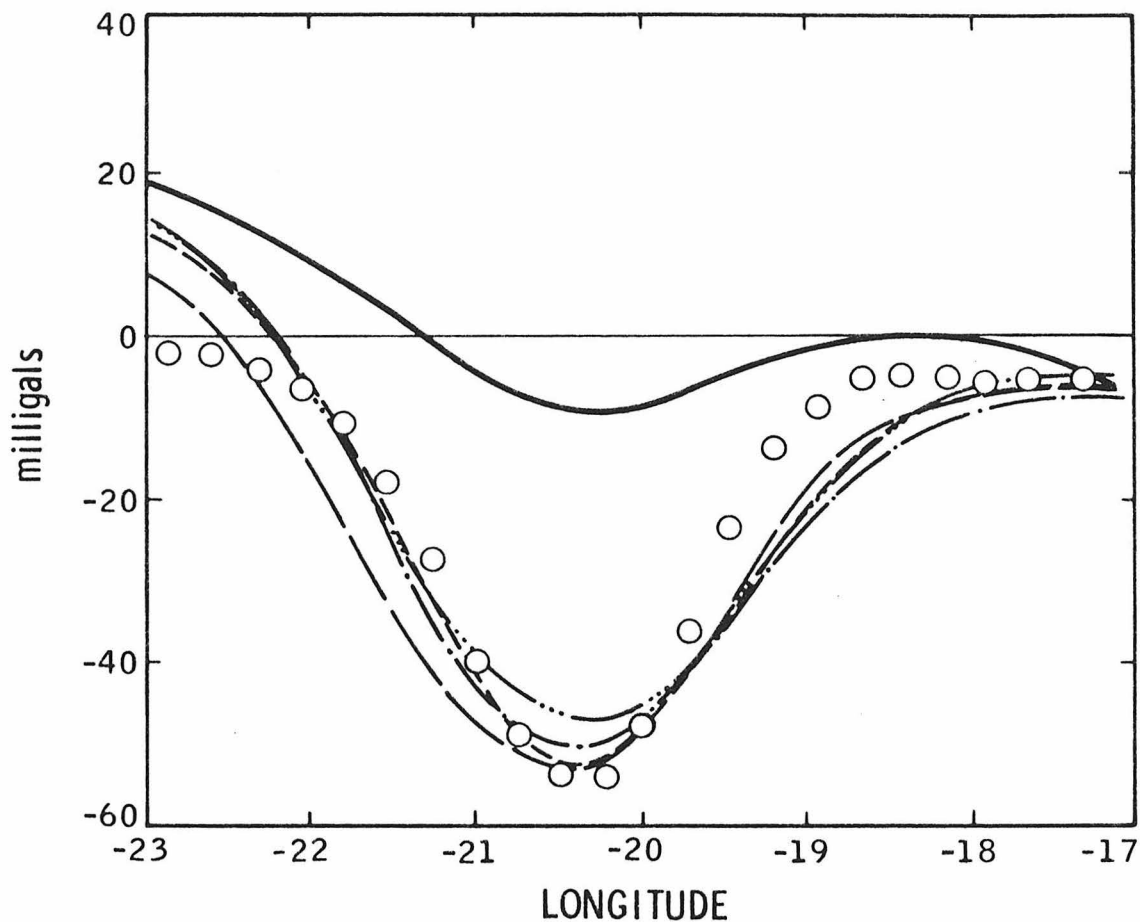


Figure 10. Comparison of four model calculations described in the text with the free-air gravity data for a single profile across Copernicus. The sum of the gravitational effects of the subsurface and topographic models are matched to the free-air gravity. The density contrast is expressed in ( $\text{gm/cm}^3$ ). The models refer to those in Figure 9.



○ FREE AIR GRAVITY DATA

— TOPOGRAPHY MODEL

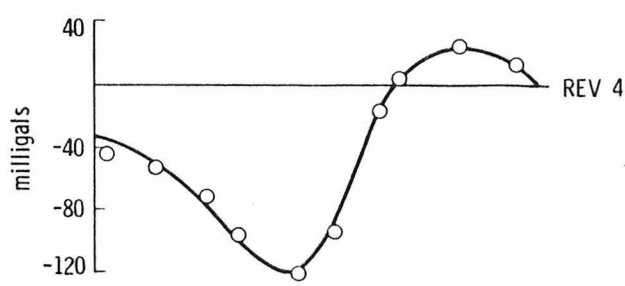
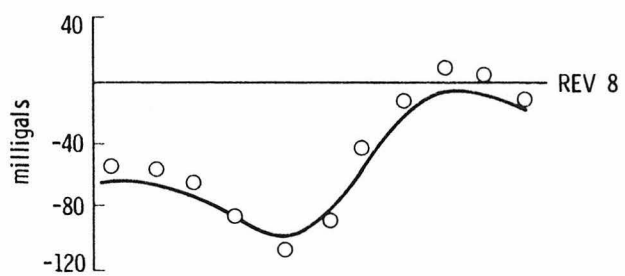
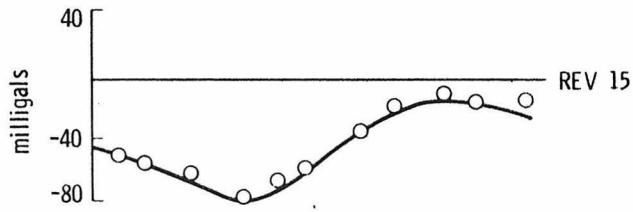
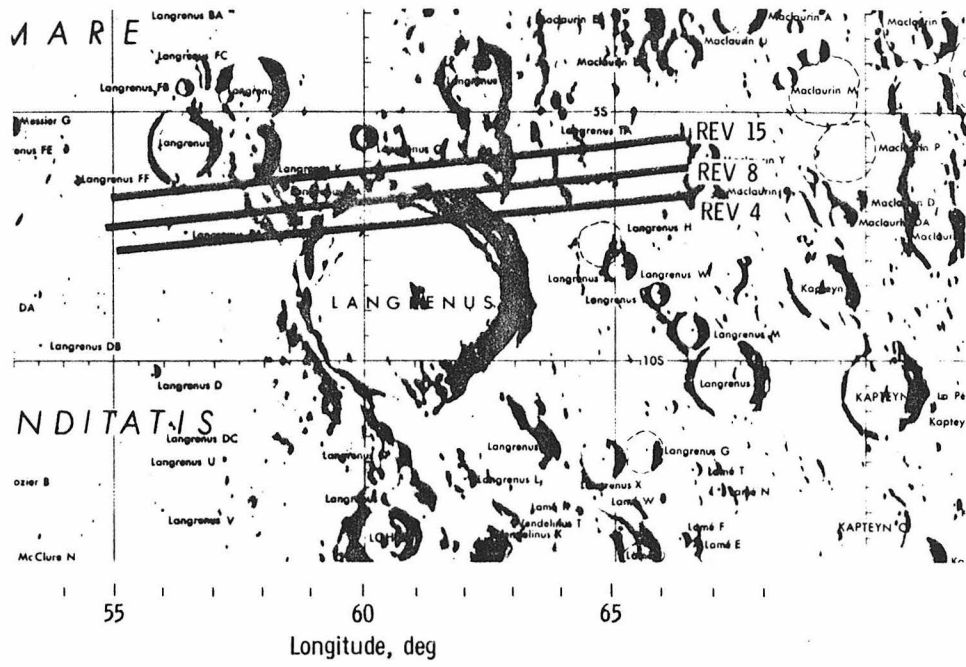
	<u>RADIUS</u> (km)	<u>THICKNESS</u> (km)	<u>DENSITY</u> <u>CONTRAST</u>	<u>MODEL</u>	<u><math>\Delta M</math> (gm)</u>
-----	25	10	-2.5	SLUMP A	$2.5 \times 10^{19}$
-...-	45	10	-0.75	SLUMP B	$2.4 \times 10^{19}$
———	25	18	-1.5	BRECCIA A	$2.6 \times 10^{19}$
·-·-·	45	30	-0.4	BRECCIA B	$3.8 \times 10^{19}$

observed gravity anomaly. The topographic contribution has been included in this computation. The total mass deficiency,  $\Delta M$ , for each model is also listed. Notice that while the volume of the anomalous low density region increases by an order of magnitude over this range of model dimensions,  $\Delta M$  changes by less than a factor of two.

The analysis of multiple orbits has not helped to alleviate this non-uniqueness problem as is evident in Figure 11. Shown here are the results of a topographic and subsurface model, similar to the fourth model computed above for Copernicus, computed for three orbital tracks across Langrenus. Use of the other three model geometries shown in Figure 9 will give almost identical gravity signatures with little variation in the values of  $\Delta M$ . Unfortunately, the available orbital coverage over all of the lunar features considered here is too confined to allow a better constraint, within the uncertainties of this analysis, of the spatial extent of the anomalous masses by the analysis of multiple orbits. However, Figure 11 does demonstrate the consistency of this analysis when applied to several gravity profiles across the same feature.

Values of  $\Delta M$  for most of the lunar features, assuming a single anomalous mass component and solving for the mass excess or deficiency which gives the magnitude of the nominal value for the Bouguer gravity, are listed in Tables V, VI and VII. The geometry used to determine these values of  $\Delta M$  was a thin cylindrical disk of similar diameter to the diameter of the feature of interest. The possible range of values

Figure 11. A comparison of identical model and topographic calculations for several different orbital tracks across Langrenus. The free-air gravity data are shown as circles (only every other data point is plotted) and the sum of the topographic and model calculations to each profile is shown as a solid line.



for this mass parameter is given in the last column of these tables. This range was determined from  $\delta g$  which is the square root of the sum of the squares of the uncertainties contributed by the topography, by an objective estimate of the ability to separate the gravity anomaly of interest from the regional background trend, by different assumed values for the density of the lunar crust in computing the Bouguer gravity, and by the intrinsic noise of the Doppler data.



CHAPTER IV  
YOUNG LUNAR CRATERS

Introduction

In this work, young lunar craters are those which exhibit at most a slight modification of the original crater form which existed shortly after the end of the impact process. No long-term endogenic or exogenic processes seem to have significantly altered the appearance of these lunar craters. The major difference in appearance of the large lunar craters considered here from the bowl-shaped form of smaller lunar craters (<15 km) is probably due to the inward collapse of material from a short-term bowl-shaped transient stage (Mackin, 1969; Malin and Dzurisin, 1978). In terms of lunar stratigraphy, these young lunar craters belong to either the Copernican or Eratosthenian systems (Wilhelms and McCauley, 1971).

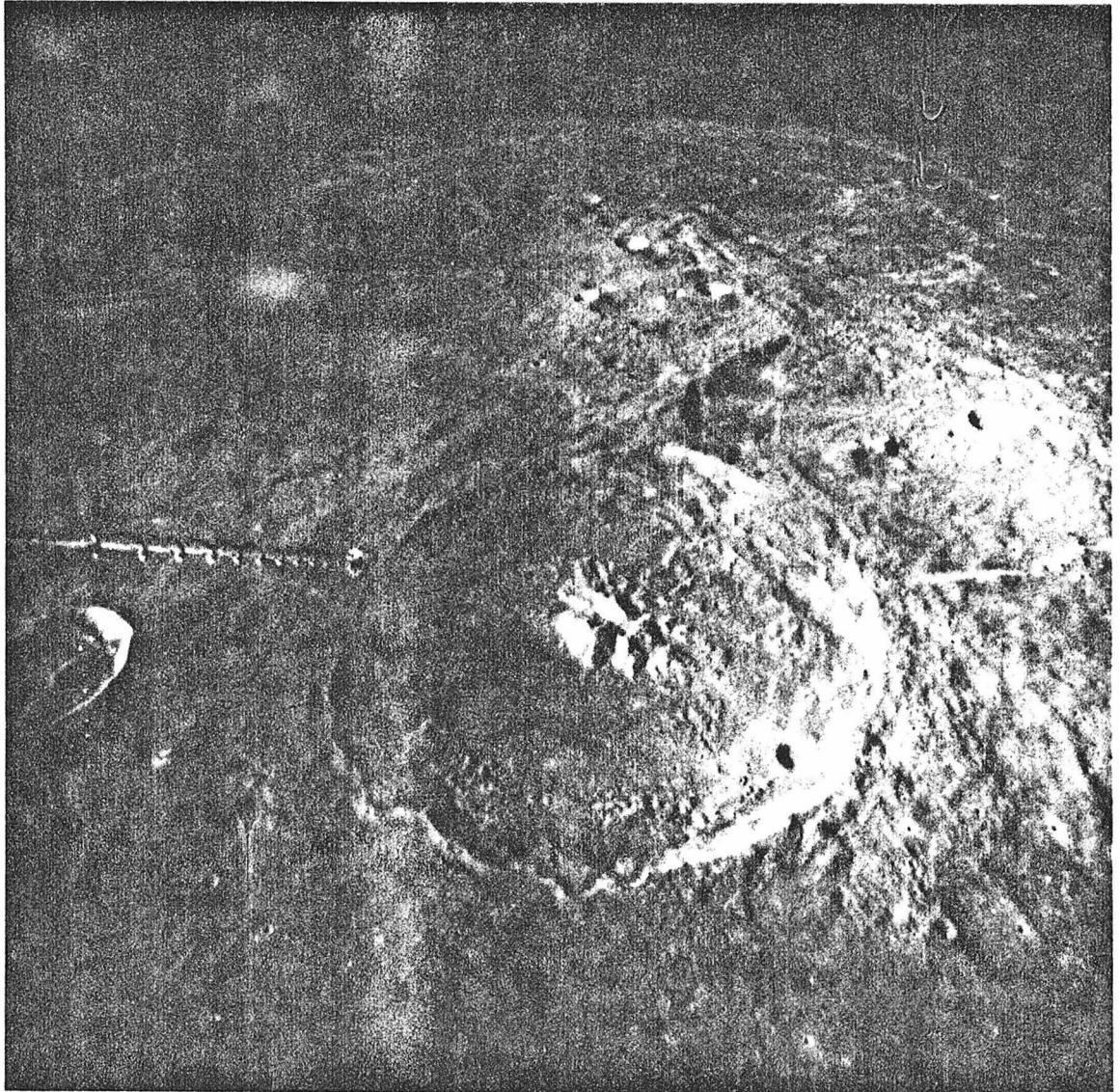
Due to the limitations of the lunar gravity and topographic data described in the earlier chapters, only a limited range of young crater sizes, from 32 to 135 kilometers, is available for this analysis. Smaller craters are below the detectable range of the lunar gravity data and larger craters are beyond the areal coverage of this same data set. A listing of the craters considered in this chapter, in order of increasing diameter, is given in Table V.

Characteristics common to each of these young craters include the presence of a sharply defined rim crest, steep inner slopes, a relatively flat floor and well-preserved interior terraces, exterior ejecta blanket, and secondary crater field (Figure 12). Many of the craters of this group have central peaks which rise one to two kilometers above

TABLE V  
SUMMARY OF YOUNG LUNAR CRATERS

NAME	DIAMETER (km)	TOPOGRAPHY meters	REGIONAL mgal	"CRUST "PURE NOISE" mgal	$\delta g$ mgal	$\Delta M$ grams	$\delta M$ grams
Kepler	32	400	5	1	8	$-4.8 \times 10^{18}$	$-3/-8 \times 10^{18}$
Herschel	42	400	10	2	10	-4.0	-2/-8
Agrippa	46	400	10	2	15	-3.7	-2/-8
Eratosthenes	58	400	5	2	15	-7.9	-3/-20
Copernicus	93	300	5	3	15	-38	-20/-80
Theophilus	100	200	30	10	10	-47	-20/-100
Langrenus	135	300	5	6	8	-90	-60/-120

Figure 12. Apollo 16 oblique metric photograph (AS16-692) of Theophilus (100 km). View is to the south. Note the pronounced central peak complex, interior wall terraces, and the shallow appearance of this crater.



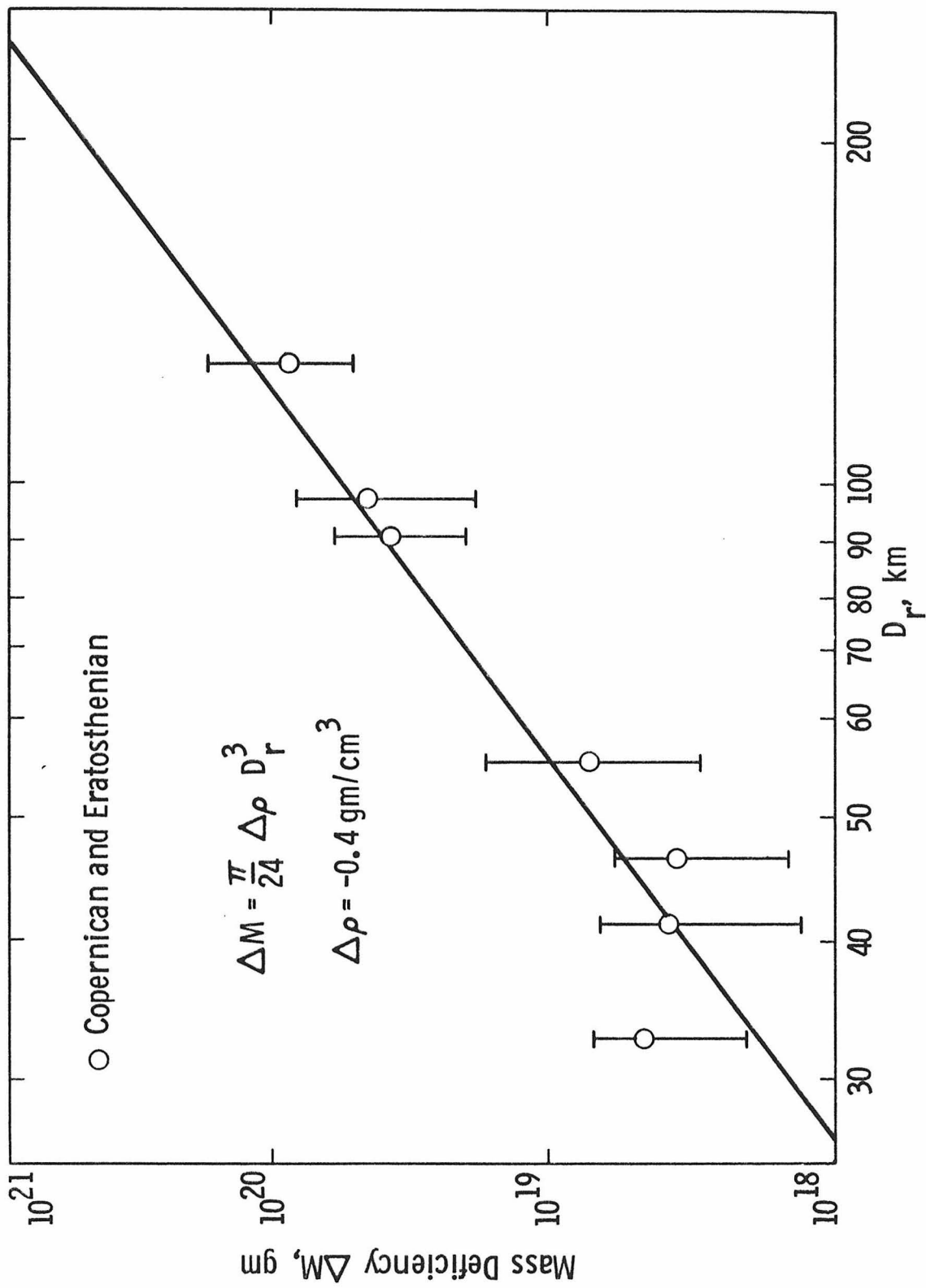
the crater floor. There is also a distinct lack of medium size craters (5-10 km diam) superposed on these large young craters. The rim-to-floor depths of these young lunar craters (see Table II) range from three to four kilometers, so that these craters are significantly shallower than crater depths extrapolated from the constant 1/5 depth/diameter ratio of small bowl-shaped craters (see Pike, 1974).

Each of these young lunar craters has a mass deficiency, that is a negative  $\Delta M$ , associated with it. These values of  $\Delta M$  are listed in the second column from the right in Table V and are plotted versus crater rim diameter in Figure 13. The range of possible values of  $\Delta M$  for each crater,  $\delta M$ , is given in the last column in Table V and is also depicted in Figure 13. This range was determined by estimating the magnitude of the uncertainty in determining the relative acceleration values,  $\delta g$ . As discussed in the previous chapter, these values of  $\delta g$  listed in Table V are the square root of the sum of the squares of the uncertainties, which are also listed in Table V, contributed by the topography, by a range of plausible values for the density of the lunar crust in computing the Bouguer gravity, and by the intrinsic noise of the Doppler data. These various error contributions for each crater are also listed in Table V.

#### Model Calculations

As discussed in Chapter III, the inversion of gravity data in terms of a density structure is nonunique, however, the determination

Figure 13. Variation of the mass deficiency with crater rim diameter for young lunar craters. The solid line is the same as shown in Figure 14.



of the mass parameter,  $\Delta M$ , is, within the uncertainties of this analysis, independent of assumptions made about the density structure. This value for  $\Delta M$  is then used to evaluate various classes of subsurface structures by prescribing the geometries and solving for the density contrasts required to give the observed value of  $\Delta M$ . Those classes of models which yield unrealistically large values for the density contrast are eliminated as possible models. These geometries are proposed on the basis on inferences made from the surface geology and, for these young lunar craters, from an examination of the subsurface structure of terrestrial impact features (see Chapter II).

To illustrate this procedure, consider the mass anomaly associated with the crater Copernicus. In Chapter II, four possible low density components were identified which contributed to the negative mass anomaly associated with terrestrial and lunar craters. The first two components considered in that chapter were those contributed by the fallback debris within the crater,  $\Delta M_{FB}$ , and by the rim structure,  $\Delta M_R$ . From the value of  $\Delta M$  for Copernicus (Table V), the volumes of both of these two components (Equations 3 and 8) are insufficient by themselves to explain the observed negative mass anomaly since these require absurdly large values for the density contrast. Hence, other low density components must be considered to account for the observed value of  $\Delta M$  for Copernicus.

The material which is responsible for the shallow depths of these craters, presumably derived by the inward slumping of the crater walls,



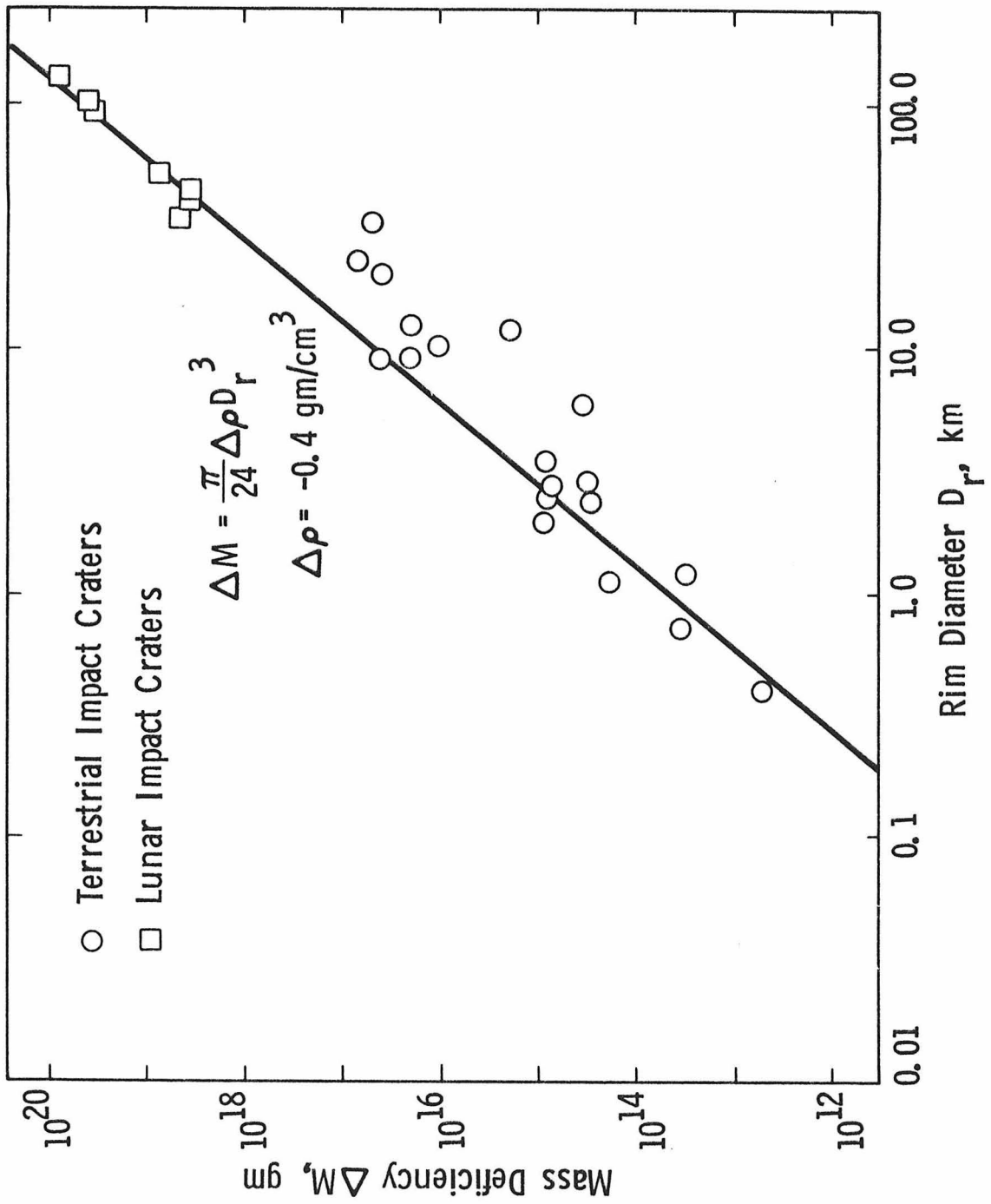
is volumetrically much larger for a given crater diameter than either the interior fallback debris or the rim deposits (Equation 15) as is the potential contribution from the lens of brecciated material which underlies bowl-shaped terrestrial craters (Equation 16). These two components have actually already been considered for Copernicus in the previous chapter. Whether the lateral extent of these two components should extend only as far as the present crater floor, which is roughly the same as the diameter of the postulated transient bowl-shaped geometry (see Chapter II), or as far as the present rim cannot be clearly decided from the surface geology. This leads to the testing of the four paraboloidal models shown in Figure 9. Models 1 and 2 in this figure are representative of the crater fill material derived by the inward collapse or slumping of the postulated transient crater walls. The dashed line in the first model outlines the assumed transient cavity geometry. The vertical extent of this component was taken to be 10% of the final crater rim diameter, in accordance with the estimates made in Chapter II. In the first model the lateral extent was confined to lie within the present crater floor diameter and in the second within the present crater rim diameter. The third and fourth models are representative of the large lens-shaped brecciated region underlying most terrestrial impact craters, also discussed in the previous chapter. For these lunar craters, this also included the slumped material represented by the first two models. In both of these models, this lens of brecciated material extends to a depth of one-third its diameter. In the third model, this region is confined to lie

within the crater floor diameter, which, as mentioned above, approximately corresponds to the diameter of the postulated transient bowl-shaped cavity. The last model represents the brecciated region extending outward to the present crater rim crest, similar in horizontal extent to most terrestrial impact craters.

A comparison of the lunar gravity values computed for each model, including the topographic contribution, with the actual free-air gravity values is shown in Figure 10. As pointed out earlier, there is no preferred subsurface model based on the degree of fit to the observed gravity values. For these two components, an upper bound is placed from terrestrial experience on the negative density contrast associated with impact craters of  $-0.5 \text{ gm/cm}^3$ . Under this constraint, the first three models are unacceptable (Figure 10) and, thus, the anomalous mass must extend to at least a region as large as that shown in the fourth model. This result was also obtained for each of the other young lunar craters analyzed here.

Further support for this large breccia lens beneath lunar craters is given in Figure 14 which shows a comparison of the mass anomalies associated with terrestrial and young lunar craters. The lunar craters fall along the same cubic trend defined by the smaller terrestrial craters. For similar values of the density contrast produced by terrestrial and lunar impacts, the extent of the mass anomaly is similar, and, hence, probably due to the same component, namely a lens of brecciated material extending laterally to the rim crest and vertically to a depth of one-third the crater rim diameter. So that for Langrenus,

Figure 14. A comparison of the variation in the mass deficiency associated with terrestrial and young lunar impact craters with the crater rim diameter. The solid line shows a cubic relation between the mass deficiency and the crater rim diameter.



this extends to a depth of forty kilometers.

### Discussion

Figure 14 suggests that for a given impact crater diameter the volume of brecciation is the same on the Earth and on the Moon and, hence, for a similar geometry of this brecciated region, so is the depth of brecciation. Recall that the results of drilling logs and recovered cores at several terrestrial sites indicated that the maximum depth of the transient cavity, as inferred from the erratic vertical distribution of shock effects and the existence of a basal melt layer, is close to the maximum depth of brecciation, within about 80%, so that the maximum depth of the transient cavity associated with these lunar craters probably extended to similar scaled depths into the lunar crust, roughly one-fourth of the present crater rim diameters. During the penetration of the meteorite, material was ejected and deposited on the surface. Experimental hypervelocity impacts, producing craters in the ten centimeter diameter range, have shown that the bulk of the material ejected beyond the crater rim comes from a depth of roughly one-third the inferred depth of the cavity at the end of the excavated stage (Stöffler et al., 1975). A similar scaled depth of origin may also be true for the bulk of the ejecta surrounding lunar craters. However, local inhomogeneities within the target material may allow small amounts of material to be derived from depths as great as that of the transient cavity and to be found in the fallback or mixed debris unit.

The ability, as determined by the relative time available, to eject material from these greater depths will decrease with increasing crater diameter since the gravitational effects producing the inward return flow become more important earlier in the impact process. To demonstrate this, the ratio of the characteristic time for material to slump inward,  $\tau_s$ , to the time required for the ejecta to travel from the crater bottom to the surface,  $\tau_e$ , is estimated. The time for the inward return of material by gravitational forces is approximated by the free-fall time from the surface to the bottom of the crater.

$$\tau_s \sim \sqrt{2d_p/g} \quad (19)$$

Here  $d_p$  is the maximum depth of the transient cavity which is approximately equal to one-fourth the final crater diameter,  $D$ . The time for material to be ejected from a depth of  $d_p$  is

$$\tau_e \sim d_p/v_e \quad (20)$$

where  $v_e$  is the ejection velocity which is typically some fraction of the impact velocity. Here, as a rough approximation,  $v_e \sim \frac{1}{10} v_i$  is used where  $v_i$  is the impact velocity. The ratio of these two time scales will give the relative time available to eject material from craters of different diameters.

$$\begin{aligned} \tau_s/\tau_e &\sim \sqrt{2v_e^2/gd_p} = \frac{1}{5} \sqrt{\frac{1}{2}v_i^2/gd_p} \\ &\sim \frac{1}{5} \sqrt{\frac{2v_i^2}{gD}} \end{aligned} \quad (21)$$

Assuming an impact velocity of 10 km/sec,

$$\tau_s/\tau_e \sim 30 \text{ for Meteor Crater and}$$

$$\tau_s/\tau_e \sim 7 \text{ for Copernicus.}$$

That is, there is a longer relative time interval available during the formation of Meteor Crater than Copernicus to eject material during the excavation stage of cratering before the occurrence of the inward slumping of material. This ratio also suggests that there is sufficient time available in almost all impacts on the Moon to eject at least small amounts of material from depths much greater than the shallower source for the bulk of the deposits comprising the rim material.

Extrapolating this to large lunar basins, this suggests that for an Imbrium size event ( $D_r \sim 300$  km), the transient cavity penetrated well below the lunar crust and small amounts of material from the lunar mantle were probably excavated and reside on the lunar surface. Hence, the dunite fragments collected at the Apollo 17 landing site (Dymek et al., 1975) could possibly be derived from the lunar mantle and not necessarily represent a "cumulate" rock that formed within the lunar crust.

## OLD UNFILLED LUNAR CRATERS

Introduction and Description

This chapter extends the analysis of the lunar gravity anomalies to those craters which, according to the geologic map of the lunar nearside (Wilhelms and McCauley, 1971), belong to either the Imbrian or pre-Imbrian systems. A listing of these craters in order of increasing diameter is given in Table VI.

These particular Imbrian and pre-Imbrian age craters are similar in some aspects to the morphology of the younger lunar craters which have been considered in the previous chapter. Craters of both age groups have relatively flat floors and terraced interior walls and central peaks. More importantly, the depth/diameter ratios of the craters listed in Table VI are not greatly different from values for younger lunar craters within the same diameter range (e.g., Pike, 1976), that is, these particular craters have not been significantly shallowed by either endogenic or exogenic processes to the extent the craters to be considered in the next chapter have been shallowed. The major distinction between craters in these two age groups is the more subdued appearance of the older craters (Pohn and Offield, 1970) and the superposition of one or more craters of medium-size (~10 km) upon these older craters. It is these indicators which have been used as the major criterion in assigning an Imbrian or older age to those craters listed in Table VI. However, this approach of relative age dating of



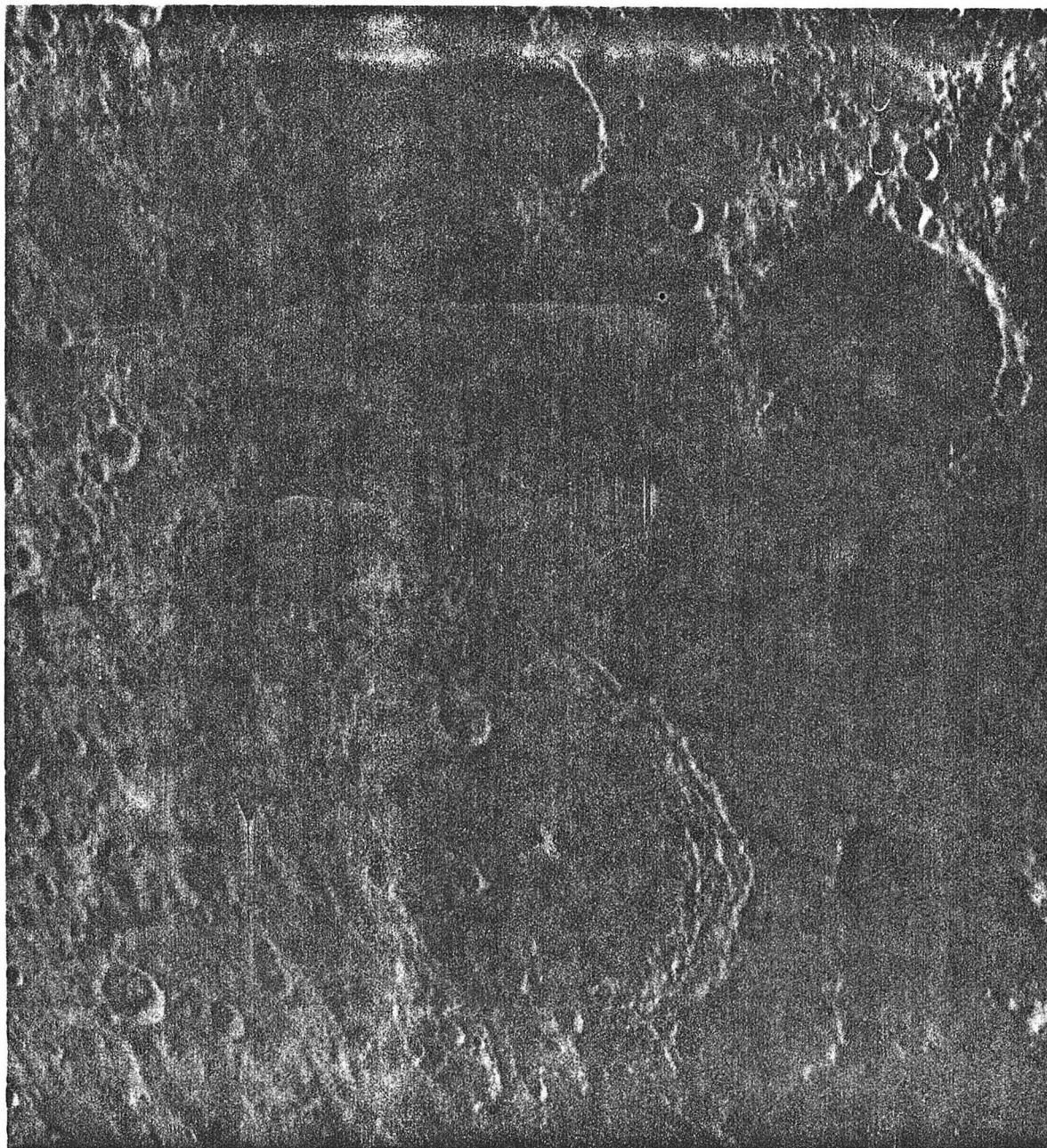
TABLE VI  
SUMMARY OF OLD UNFILLED LUNAR CRATERS

NAME	DIAMETER (km)	TOPOGRAPHY meters	REGIONAL mgal	$\rho$ CRUST "PURE NOISE" mgal	$\delta$ g mgal	$\Delta M$ grams	$\delta M$ grams
Macrobius	65	400	10	3	14	0	-2/+2 x 10 <sup>18</sup>
Snellius	83	300	5	3	8	0	-6/+6
Piccolomini	89	300	10	3	12	-20 x 10 <sup>18</sup>	-12/-30
Sacrobosco	96	200	5	2	7	0	-5/+5
Hecataeus	120	400	5	8	15	0	-10/+10
Neper	150	500	5	9	19	0	-20/+20
Petavius	176	300	5	5	10	0	-10/+10
Humboldt	200	400	5	6	17	0	-30/+30
Pasteur	240	400	5	7	19	0	-30/+30

lunar craters suffers from regional biases due to proximity to the most recent lunar multiringed basins and to the complex emplacement sequence of the lunar mare lavas. It is emphasized that clear relative age relationships do not exist between each of these craters and the defined time interval of the Imbrian period, in particular, the occurrence of the Imbrium event.

For each of the craters listed in Table VI which are adjacent to or superposed by volcanic units, the formation of the crater predates the last occurrence of surface volcanism in that locale. This includes all of these craters except Piccolomini, Sacrobosco, and Pasteur which lie well within the lunar highlands far removed from any nearby evidence of surface volcanism. The floors of three of the largest craters listed in Table VI are superposed to varying amounts by dark volcanic units. Neper (Figure 15) has a broad domical structure extending across the crater floor, the maximum relief of which is a few hundred meters. This domical structure was revealed by the Apollo Lunar Sounder Experiment (ALSE) which provided a continuous radar profile of the lunar surface along portions of the Apollo 17 CSM groundtrack. This experiment also revealed similar domical structures associated with the floors of Hevelius and Aitken (Elachi et al., 1976), two craters of similar age and diameter to Neper. These similarities make it impossible to determine whether this floor doming is characteristic of all large lunar craters, possibly produced in connection with the inward slumping of the crater walls, or, alternatively, due to their greater age perhaps the result of volcanic intrusion raising the crater

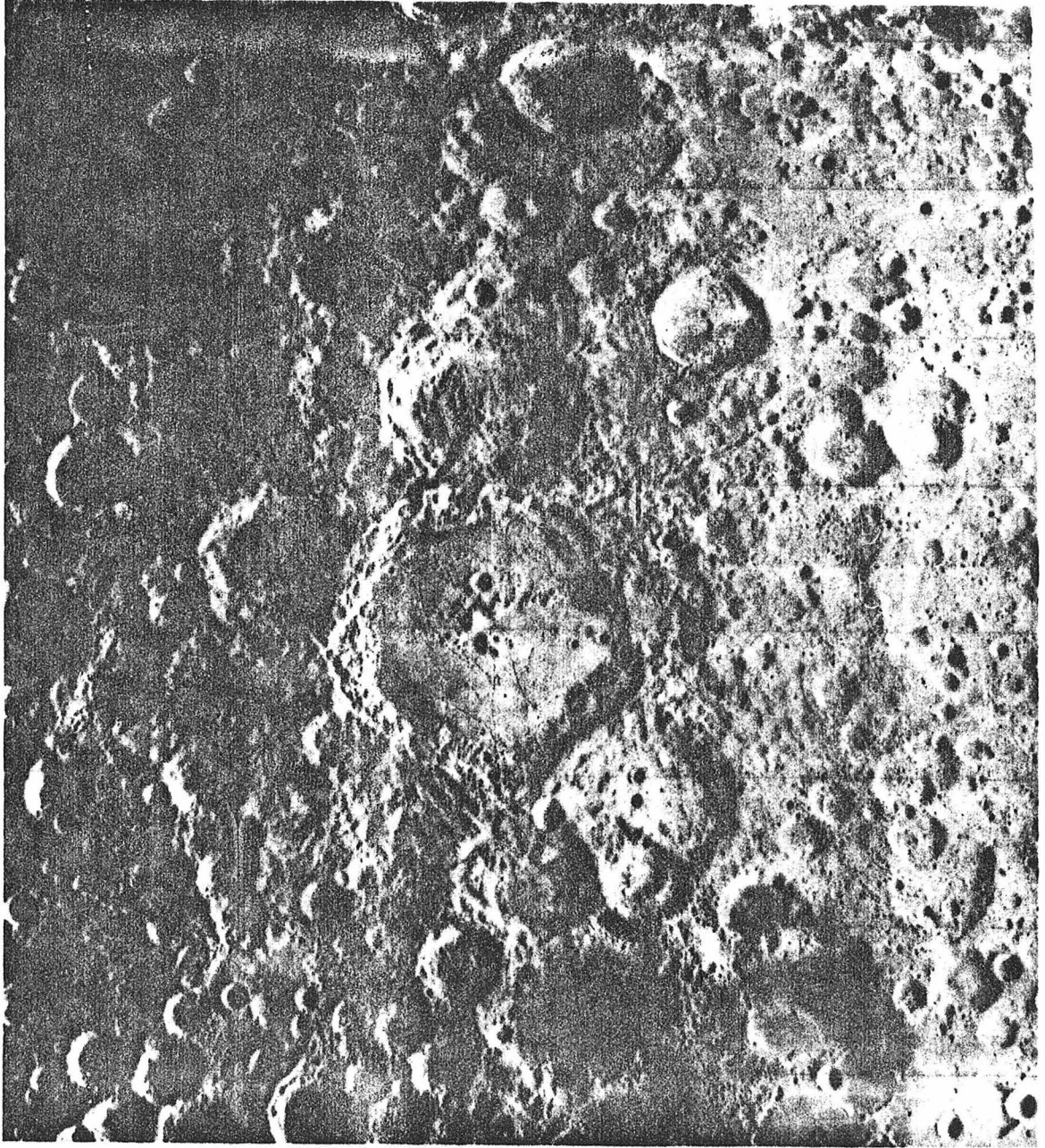
Figure 15. Lunar Orbiter photograph (IV-165-H3) of Neper (bottom center). Note that the floor of this crater is completely covered with dark mare units with the central peak protruding through these units. The present depth of this crater (4.4 km) suggests that the total thickness of these mare units is at most a few hundred meters.



floor. Floor doming in Petavius and Humboldt is suggested by the photography provided by Lunar Orbiter spacecraft. Small patches of dark volcanic units lie discontinuously along the crater floor-wall contact in both Petavius and Humboldt (Figure 16). The depth/diameter ratios for these two craters are somewhat shallower than for the other craters listed in Table VI indicating that the floors of these two craters have been uplifted the most of any of this group, from one to two kilometers. Also evident on the floor of Petavius is a radial rille pattern suggestive of the presence of a concentric or hoop tensile stress field produced by the doming and uplifting of the crater floor and resulting in failure of the lunar crust. A more extensive radial rille pattern is present on the floor of Humboldt (Figure 16) complemented by a concentric rille pattern. The pre-mare floor of Neper is possibly similarly patterned by straight lunar rilles, though these are not evident since the present floor of this crater, except for the central peak, is completely covered by mare units.

Macrobius is the smallest crater listed in Table VI and its morphologic distinctions from the other craters in this list are probably attributed to this difference. It lacks a well developed central peak and interior wall terraces. There is no clear evidence of volcanism associated with the floor of this crater which lies two kilometers below the level of the nearby mare units mapped by Scott and Pohn (1972).

Figure 16. Lunar Orbiter photograph (IV-012-M) of Humboldt. The floor of this crater is only partially covered by dark volcanic units appearing as patches along the floor-wall contact. The radial and concentric rille pattern interior to the crater is suggestive of a tensile stress field produced by the upward doming of the floor of this crater, probably the result of volcanic intrusion.



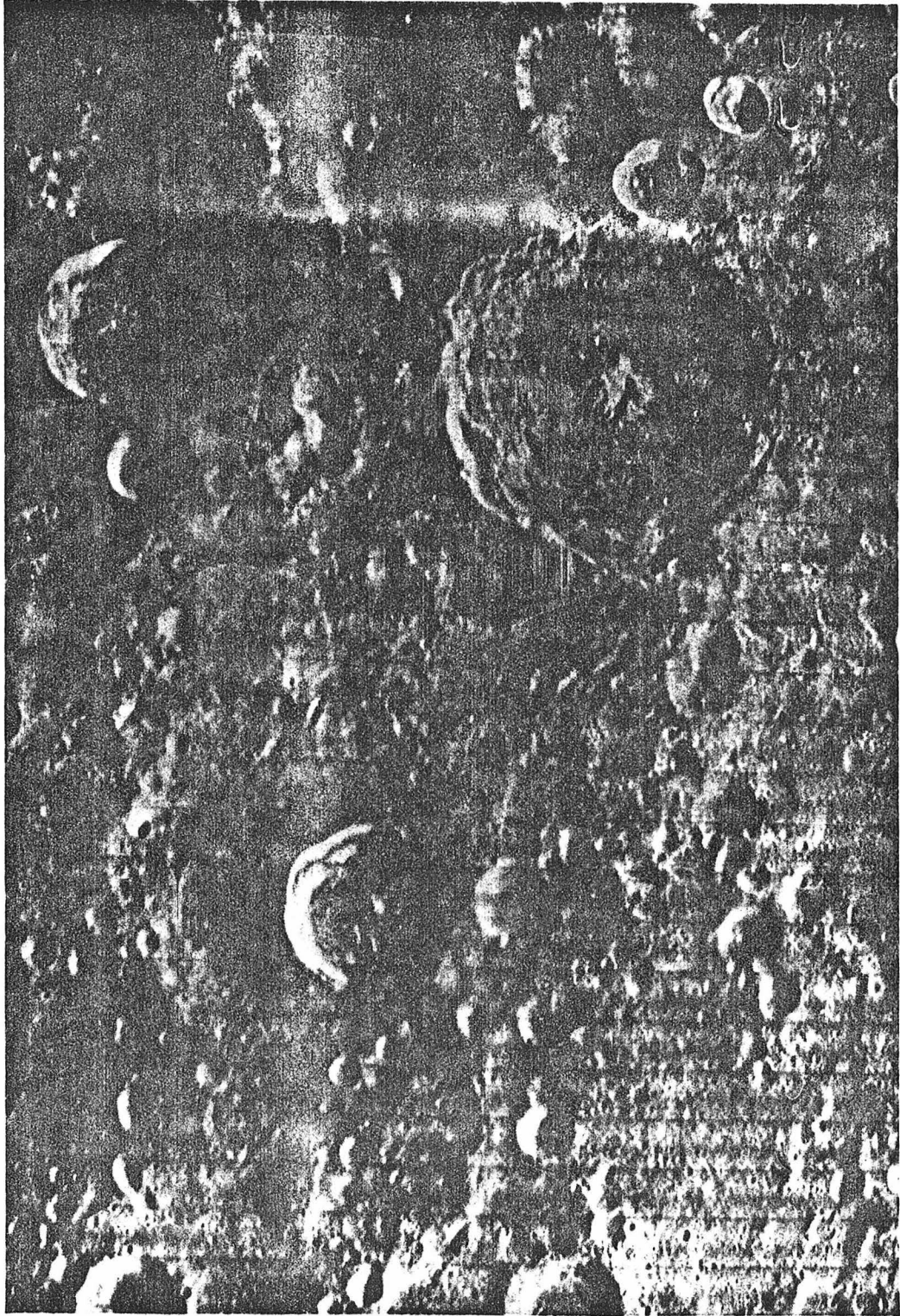
Possibly the two oldest craters in this group, based solely on relative crater morphology and degradation among all of the craters of this group, are Sacrobosco and Pasteur. These two craters lie well within the lunar highlands far removed from any evidence of surface volcanism such as dark mare material, dark-mantling pyroclastic debris, or dark halo craters. Furthermore, the floors of these craters lack straight rille patterns which would have been suggestive of volcanic intrusion (Schultz, 1976).

The morphology of Piccolomini (Figure 17) is very different from the other craters considered here. This crater is also situated well within the lunar highlands far removed from any evidence of surface volcanism and the floor of this crater also lacks a rille or fracture pattern and lies at about the same level as the mare material in the Nectaris Basin to the north. Morphologically, it appears to be much younger or at least less modified and degraded, than the other craters in this group with the exception of Macrobius.

With one exception, Piccolimini, all of the craters listed in Table VI have zero Bouguer gravity anomalies, that is, there are no detectable net mass excesses or deficiencies associated with these features. The uncertainty or range,  $\delta M$ , in the determination of the magnitude of the mass anomaly,  $\Delta M$ , is also listed in Table VI along with the contributions to the local gravity field from different error sources (see Chapter III). In the cases of zero Bouguer anomalies,



Figure 17. Lunar Orbiter photograph (IV-076-H1) of Piccolomini (upper right). The general, though more subdued, appearance of this crater compared to Copernican and Eratosthenian age craters of similar diameter (see Figure 12) suggests that the major process of post-impact modification has been by small impacts with little, if any, endogenic processes modifying the original structure of this crater.

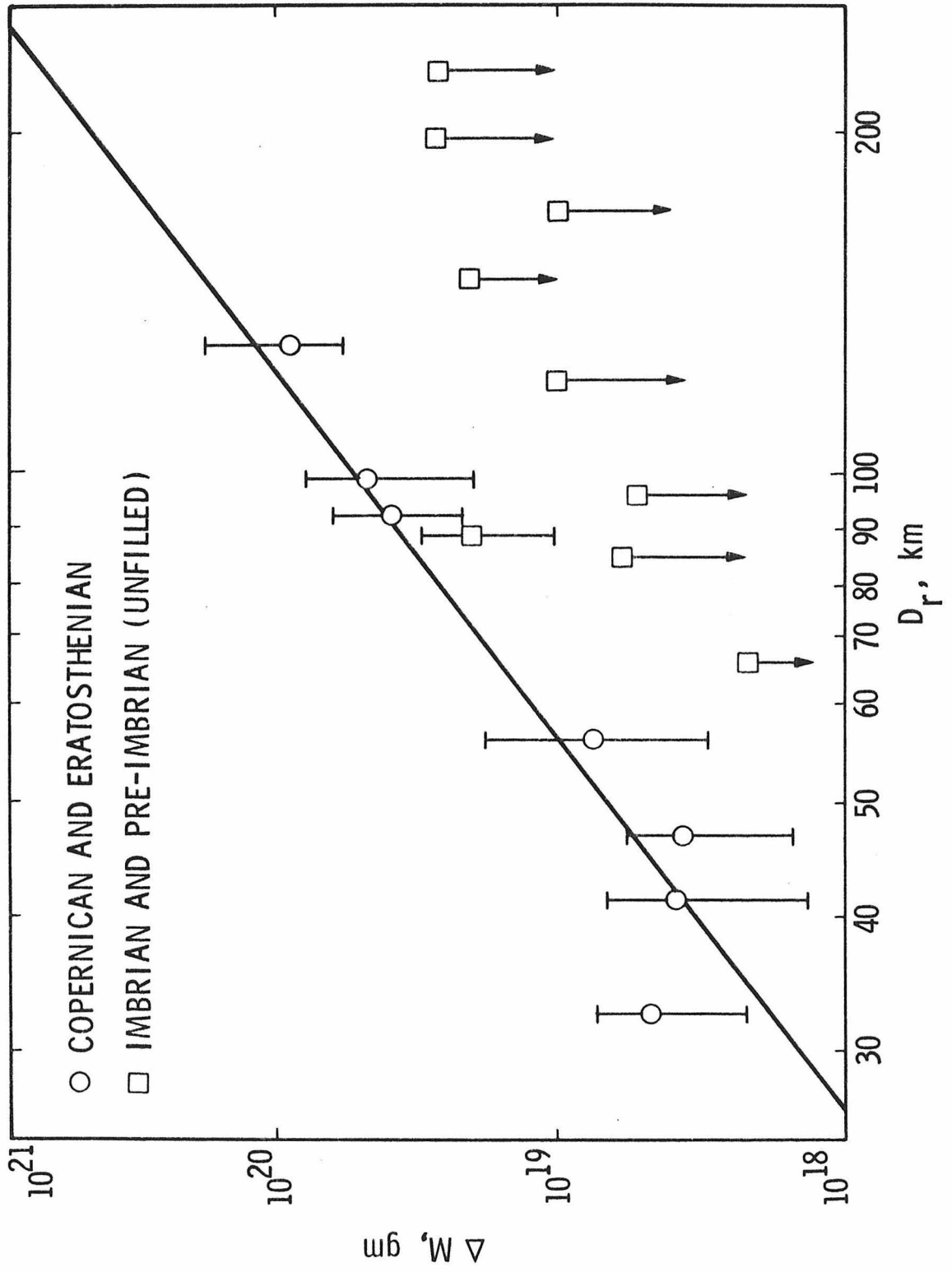


the upper bound for  $\Delta M$  is compared with values of  $\Delta M$  for young lunar craters in Figure 18. The exception for this older group of lunar craters is Piccolomini which has a negative Bouguer gravity anomaly which corresponds to a mass deficiency of  $-2 \times 10^{19}$  grams, a nominal value slightly below the trend for young lunar craters (Figure 18) which may be due to a smaller density contrast associated with this highland crater.

### Discussion

It is assumed that all of the lunar craters analyzed so far, including the seven young lunar craters in the previous chapter and the nine craters presented here, are a representative sample of other lunar craters of similar ages, diameters, and gross morphology. The basic morphologic distinction among the Copernican and Eratosthenian and the Imbrian and pre-Imbrian age craters have been summarized and contrasted in the previous section in an effort to be aware of possible subsurface structural differences which may affect the density structure or mass anomaly. The characteristic common to each of the lunar craters discussed here is that they are all relatively deep craters whose present floor is a few kilometers below the pre-impact level. Whatever processes have acted to modify these craters have not resulted in drastically reducing their depths to the extent exhibited in such craters as Ptolemaeus, Hipparchus, or Fra Mauro to be considered in the next chapter.

Figure 18. Comparison of  $\Delta M$  values determined for young lunar craters (Chapter IV) with upper bound values of  $\Delta M$  for unfilled Imbrian and pre-Imbrian age craters. The negative value of  $\Delta M$  for Piccolomini is also shown. The solid line is the same as shown in Figure 14.



The basic observation is that all seven of the young craters and one Imbrian age crater situated in the lunar highlands have negative Bouguer anomalies. As discussed in the previous chapter, these negative anomalies are probably due to an increase in porosity of the lunar crust, presumably the result of brecciation and fracturing by the impact event. For the remaining Imbrian and pre-Imbrian age craters, at least 80% of the gravitational effect of this original porosity has been removed. It is proposed that this removal occurred either by a compaction process reducing the initial porosity or by the presence of a separate high density component resulting in a net zero mass anomaly. In the latter case this may be due to either intrusion of magmatic material or isostatic uplift of the lunar mantle. These various mechanisms will be evaluated next.

#### Isostatic Uplift

The upwelling of the lunar mantle in response to the shear stresses generated beneath lunar craters, due mainly to the presence of the crater bowl, has been suggested as a mechanism to account for changes in crater depths and rim height with increasing crater age (Baldwin, 1970; Pike, 1967; Kunze, 1974). This mechanism is analogous to the treatment of the glacial rebound problem in terrestrial studies (e.g., Walcott, 1970; McConnell, 1965), that is, there is a slow isostatic response of the planetary interior relieving the differential stresses produced by uncompensated surface loads. Craters

produce predominantly negative (i.e., upward) surface loads which, depending on the rheologic behavior of the lunar crust and upper mantle, may result in a net upward movement of higher density mantle material displacing crustal material. This net upward flow of higher density mantle material to an isostatic state should produce a systematic variation in the observed mass anomaly with crater diameter.

This variation has been calculated for the Imbrian and pre-Imbrian age craters considered here assuming a depth of sixty kilometers to the lunar mantle and estimating the amount of uplift necessary to relieve the differential stresses at this depth produced by the crater bowl and by the presence of the low density breccia lens. This depth was chosen since this is, presumably, the location of the major density contrast in the outer regions of the Moon, and, hence would primarily be responsible for the isostatic relief of interior stresses. The expected Bouguer gravity anomalies, assuming a completely isostatic state, for the orbits across these craters listed in Table I, including the contribution of the breccia lens, would range from -20 milligals for Macrobius to +30 milligals for Neper to +70 milligals for Humboldt, a trend clearly distinguishable from the zero Bouguer anomalies observed for each of these craters (see Table VI).

Amending these assumptions to include the possibility of a deeper depth of compensation would have the effect of increasing the value of the expected Bouguer anomaly at a greater rate with crater diameter than that determined in the above calculation. This would result,

assuming a threshold stress, since a deeper depth of compensation would act to preferentially relieve the stresses and, hence, produce more uplift, beneath craters of larger diameter or greater spatial extent. Similarly, partial compensation of these craters will have this same effect since the degree of compensation will increase, at a faster rate with crater diameter than in the calculation given above, again assuming a threshold stress and assuming a viscous response in which the amount of relaxation will be inversely related to the wavelength (McConnell, 1965).

In view of this, no support is found for a significant amount of isostatic upwelling of higher density lunar mantle material beneath any of these lunar craters.

#### Volcanic Intrusion

As mentioned earlier, where such relationships do occur, each of the Imbrian and pre-Imbrian age craters which have zero Bouguer anomalies also predate the last occurrence of surface volcanism in that locale. For three of the largest craters dark volcanic units partially or totally cover these crater floors, however, the amount of this extruded material is in each case insufficient by itself to mask the negative gravitational effect of the porous brecciated region. So that, if a volcanic process is responsible for the observed net zero Bouguer anomalies, then most of the higher density component must have been intruded beneath the crater, presumably into the cracks and



fractures produced by the impact.

A simple model of passive fluid flow through a porous medium under hydrostatic pressure, similar to the movement of groundwater on the Earth, is an inadequate mechanism for the transport of magma through a planetary crust (Turcotte and Ahern, 1978) since heat is rapidly transferred from the melt to the surrounding cold rock resulting in solidification of the magma and a halt to its migration. To illustrate, the velocity,  $v$ , at which a fluid will migrate through a porous medium, is given by Darcy's law (DeWiest, 1965).

$$v = k\rho g/\eta \quad (22)$$

where  $k$  is the permeability of the porous medium, and  $\rho$  and  $\eta$  are the density and viscosity of the fluid, respectively. The permeability will be a function of porosity and particle size. Maximum values measured for the permeability of natural materials range from  $10^{-5}$  to  $10^{-3} \text{ cm}^2$  (Chow, 1964). This latter value corresponds to clean gravels with 20% porosity (Linsley et al., 1958). Using typical values for the density and viscosity of lunar magmas,

$$\rho = 3.0 \text{ gm/cm}^3 \quad (\text{Solomon, 1975})$$

$$\eta = 30 \text{ poises} \quad (\text{Murase and McBirney, 1970})$$

the velocity given by Equation (17) may be as great as 5 km/yr. So that it would take at least six years for magma to flow by this mechanism through a breccia lens thirty kilometers thick. However, the minimum crack size which would allow the magma to migrate at this

rate over this distance without solidifying by conduction of heat to the surrounding cold crust in this time interval is determined from the diffusion equation to be  $\sim 10$  meters (Jaeger, 1968), probably an absurdly large value for the major void space beneath these craters. The transport of magma through a planetary crust requires the formation of large igneous bodies and structures, such as dike, sill, and sheet complexes, to overcome this transfer of heat away from the magma.

The intrusion of sufficient quantities of magma may deform and fracture the crust. Indeed, several investigators have suggested that the major floor fractures in many lunar craters, such as Humboldt (Figure 16), and the anomalously low depth/diameter ratios of many of these same craters may be the surface expression of intrusive activity (Whitford-Stark, 1973; Schultz, 1976).

If it is assumed that the uplift of the crater floor is due to the intrusion of magma into a horizontal sill, then it is possible to estimate the amount of intruded material necessary to balance the gravitational effect of the low density breccia lens and predict the expected amount of floor uplift. Compaction of the porous brecciated region by this predominantly horizontal intrusive geometry is assumed to be negligible since the vertical stresses produced are probably insufficient to compact the overlying crust. The mass anomaly contributed by the breccia lens,  $\Delta M_{br}$ , is given by Equation (16)

$$\Delta M_{br} \sim \frac{\pi}{24} \Delta \rho_{br} D_r^3 \quad (16)$$

$$\Delta \rho_{br} = -0.4 \text{ gm/cm}^3$$

where  $D_r$  is the crater rim diameter and  $\Delta \rho_{br}$  is the density contrast between the breccia lens and normal lunar crust. Modeling the geometry of the horizontal sill as a right cylinder with a diameter equal to the crater rim diameter, the contribution to the mass anomaly will be

$$\Delta M_{in} \sim \frac{\pi}{4} \Delta \rho_{in} t D_r^2 \quad (23)$$

where  $\Delta \rho_{in}$  is the density contrast between the solidified intruded material and normal lunar crust and  $t$  is the average thickness of the sill. In order to result in a new zero mass anomaly, these two contributions must be of similar magnitude.

$$-\Delta M_{br} \sim \Delta M_{in}$$

Using a value of  $+0.6 \text{ gm/cm}^3$  for  $\Delta \rho_{in}$ , the thickness of the sill, and the expected amount of uplift of the crater floor, will be

$$t \sim (1/6) (\Delta \rho_{br} / \Delta \rho_{in}) D_r = (1.10) D_r \quad (24)$$

For a 100 kilometer crater, the uplift will be  $\sim 10$  kilometers, a value much in excess of the original depth of the crater and much larger than the one to two kilometer maximum uplift of the floors of Petavius and Humboldt estimated from a comparison of their present depths ( $\sim 2$  km) with the depths of young lunar craters ( $\sim 4$  km) of a similar diameter range (Pike, 1974).

The situation is worse for the crater Neper, whose present rim-to-floor depth (4.4 km) is comparable to depths of younger lunar craters. The broad doming of the floor of this crater, revealed by the lunar sounder profile (Elachi et al., 1976), is the only evidence of vertical uplift associated with the floor of this crater. Assuming that this domical structure is the result of magmatic intrusion, the volume necessary to produce the observed amount of doming may be estimated. Treating the lunar crust as an elastic half space and modeling the intrusion as a spherical cavity, the vertical deformation,  $\Delta h$ , will be (Mogi, 1958)

$$\Delta h = \frac{3 a^3 \Delta P}{4\mu} \frac{f}{(f^2 + r^2)^{3/2}} \quad (25)$$

where  $a$  is the radius of the sphere,  $\Delta P$  is the change of the hydrostatic pressure in the sphere,  $f$  is the depth to the center of the sphere from the surface,  $r$  is the radial distance, and  $\mu$  is the rigidity of the lunar crust. For an incompressible medium, integration of the above equation gives the volume of the intruded material in terms of  $f$  and the maximum amount of uplift,  $\Delta h_{\text{MAX}}$ .

$$\Delta V = 2\pi \Delta h_{\text{MAX}} f^2 \quad (26)$$

If the radial distance at which the vertical deformation falls to one-half its maximum value,  $r_{\frac{1}{2}}$ , is known, then  $f$  may be determined independent of the other parameters.

$$f = 1.3 r_{\frac{1}{2}} \quad (27)$$

For Neper, from the lunar sounder profile (Elachi et al., 1976)

$$\Delta h_{\text{MAX}} = 0.2 \text{ km}$$

$$r_{\frac{1}{2}} = 30 \text{ km}$$

$$f = 40 \text{ km}$$

so that  $\Delta V = 1800 \text{ km}^3$ .

Again assuming a density contrast of  $+0.6 \text{ gm/cm}^3$ , the contribution of the intruded material to the mass anomaly will be  $+1 \times 10^{18}$  grams, a value much too small to balance the mass deficiency of  $-2 \times 10^{20}$  grams, estimated from Equation (16), contributed by the breccia lens.

Part of the difficulties presented by the above two calculations may be removed if the geometry of the intrusion resulted in principally an outward radial deformation or compression with only a minor component of vertical movement. This may be accomplished if most of the material was intruded as vertical or slightly inclined sheets somewhat analogous to the emplacement of cone-sheets (Anderson, 1936). It is difficult to make simple estimates of the amount of surface deformation expected from this intrusive geometry and, hence, to determine whether there should be a noticeable amount of surface displacement.

A magmatic stoping process (Daly, 1903; 1933), which requires a continual replenishing of hot material as the magma rises to the

surface, combined with localized injection of magma into and partial assimilation of the brecciated regions of the lunar crust is an alternative means to fill most of the pore space of the breccia lens without major surface disturbance or uplift. A stoping process is invoked in terrestrial studies to account for the intrusion of magmatic material without significant deformation of the country rock, however, a pure stoping process is believed to be responsible for only the completion of the intrusive process (Daly, 1933). Magmatic stoping may be more efficient in the lunar crust due to the lower viscosity of the lunar magmas (Murase and McBirney, 1970), which would more readily allow for the renewed supply of hot magma to the front of the intrusion. However, the higher density of the lunar magmas compared to the density of the lunar crust (Solomon, 1975) will not allow portions of the lunar crust to fall through the magma, instead they will float upon the magma reservoir.

A possible remaining difficulty with the volcanic hypothesis as a mechanism for explaining the lack of negative mass anomalies associated with the Imbrian and pre-Imbrian age craters is the presence of zero mass anomalies associated with two pre-Imbrian highland craters, Sacrobosco and Pasteur, which show no recognizable floor fractures or volcanic units. For these two cases, either the amount of intruded material was comparable in intensity to that associated with Neper and Humboldt, but did not result in any surface expression of this activity, or a different mechanism must be

invoked to remove the initial negative gravity anomalies associated with these highland craters. An alternative mechanism is discussed in the next section.

### Seismic Shaking

Much attention has recently been paid to the modification of lunar surface features by seismic waves produced by large impacts (Schultz and Gault, 1975; 1976). Though the seismic efficiency of these events is low, there is sufficient energy in an Imbrium-size event to globally affect the lunar crust (Hughes et al., 1977). In this section the possibility will be explored that seismic waves produced by these events were capable of compacting the porous brecciated regions beneath the older lunar craters and, subsequently, removing the negative gravity anomalies.

Experiments show that the ability to reduce the porosity,  $n$ , by vibration is determined by the acceleration ratio,  $(a/g)$ , where  $a$  is the acceleration and  $g$  is the surface gravity, and also by the coefficient of vibratory compaction,  $\alpha$  (Barkan, 1962), which depends on the grain size and the confining pressure. For loose sand under no confining pressure

$$\alpha \sim 0.4 \text{ to } 0.8.$$

Almost complete compaction will be accomplished by a single seismic event (Newmark and Rosenblueth, 1971). For a medium of low porosity the above parameters are related to the initial and final porosities in the following manner.

$$n_f = n_i \exp [-\alpha(a/g)] \quad (28)$$

If the initial porosity beneath lunar craters is 15% and if approximately 80% of this must be removed to give undetectable mass anomalies,

$$\alpha(a/g) \sim 2.$$

Using an intermediate value of  $\alpha$  for loose sand, determined from laboratory measurements, then

$$(a/g) \sim 4.$$

Values of  $\alpha$  for other particle sizes are not available, however, qualitatively, the larger particle size associated with the porous breccia lens of impact craters will probably decrease  $\alpha$  and increase the required acceleration ratio. The effect of confining pressure will be to increase  $\alpha$ , and, hence, decrease the required accelerations for compaction, so that this mechanism is more efficient at greater depths in the Moon.

From measurements of large underground explosions (Carder and Cloud, 1959), seismic waves produced by these events having periods of 0.5 seconds or greater will have amplitudes of

$$A \text{ (cm)} \sim 4(a/g).$$

For the required acceleration ratio, the amplitudes must be of the order of a few centimeters over most of the Moon. Extrapolating the impact-generated ground motion studies of Latham et al. (1970)



and using their one-third energy scaling relation, these amplitudes require minimum impact energies of  $\sim 10^{32}$  ergs, that is, an Imbrium size event (O'Keefe and Ahrens, 1976).

The above estimates merely demonstrate the possibility that the seismic energy generated by an Imbrium-size event may be capable of reducing the initial porosity beneath lunar craters. The largest uncertainty is in the appropriate value to be used for the parameter  $\alpha$ .

This seismic mechanism may not only account for the zero mass anomalies associated with the pre-Imbrian craters but also with the **Imbrian** craters discussed in this chapter since relative age relationships do not rule out the possibility that these Imbrian craters predate the Orientale event and, in many cases, may also predate the Imbrium event. However, a difficulty with any type of compaction process invoked to remove the initial porosity associated with these craters is that this must result in a large subsidence of the crater floor. For a 100 kilometer crater the floor must have subsided roughly two kilometers below its original level; a result apparently inconsistent with the present depth/diameter ratios for these craters, though this difficulty may be alleviated by a simultaneous shallowing of the crater by the inward collapse of the crater walls initiated by the same strong ground motion.

Summary

The Bouguer gravity or mass anomalies associated with the Imbrian and pre-Imbrian age craters analyzed here are very different from the values of the mass anomalies associated with younger lunar craters discussed in the previous chapter. In the latter case a negative mass anomaly (i.e., a low density region) had previously been shown to be associated with each of these features, presumably due to an increase in porosity resulting from brecciation of the lunar crust by the impacts which formed these craters. One Imbrian age crater situated in the lunar highlands, Piccolomini, far removed from any clearly identified evidence of surface volcanism, also has a negative anomaly of similar magnitude to the mass anomalies of the younger lunar craters. This crater also appears to be younger, or at least less modified, than the other craters considered in this chapter. The Bouguer gravity anomalies for each of the remaining Imbrian and pre-Imbrian age craters are zero, that is, there is no detectable net mass excess or deficiency associated with any of these features.

The cause for this change in the value of the mass anomaly with increasing crater age is expected to be related to the more modified appearance of these craters. The processes responsible for the post-impact modification of these Imbrian age craters may also be responsible for removing the negative mass anomalies initially associated with these features.

Several investigators have previously suggested that these modifications were the result of an isostatic process which relieves the differential stresses produced at depth by the initial crater bowl. This mechanism would predict a systematic increase in the mass anomaly with crater diameter, a trend which would be clearly distinguishable from the zero Bouguer anomalies observed independent of crater diameter. The absence of this trend argues against the modification of lunar craters by this process.

The intrusion of higher density volcanic material into the cracks and fractures beneath these impact craters may be responsible for part or all of the net zero mass anomalies associated with Imbrian and pre-Imbrian age craters. This mechanism is particularly attractive since surface volcanism postdates the formation of each of the Imbrian age craters which have zero mass anomalies and since the absence of surface volcanism could account for the negative mass anomaly associated with the one Imbrian age highland crater analyzed, Piccolimini. However, this mechanism cannot operate simply by the passive rise of magma under hydrostatic pressure, as was suggested by Minear (1977), since the magma would have solidified before rising any substantial distance within the breccia lens. Furthermore, the required volume of high density intruded material necessary to balance the gravitational effect of the porous breccia lens cannot be provided by the observed amounts of crater floor uplifts. So that, a difficulty with the volcanic mechanism is that the amount of intruded material

must have been sufficient to balance the gravitational effect of the porous brecciated region without completely shallowing the crater. This requirement may be circumvented either by an intrusive geometry similar to terrestrial cone-sheeting or by a large scale magmatic stopping process which might operate more efficiently on the Moon due to the lower viscosity of the lunar magmas. A possible remaining difficulty with a volcanic mechanism is that there are two pre-Imbrian age highland craters which show no evidence of intrusive or extrusive volcanic activity. In these cases, either the amount of intruded material was comparable to that associated with the other Imbrian and pre-Imbrian craters, but did not result in any surface expression of this activity, or a different mechanism is responsible for removing the negative gravity anomalies initially associated with these craters.

A possible alternative mechanism is the seismic shaking of the lunar crust resulting from the formation of the last multiringed basins (Orientale and Imbrium). Rough estimates of the g-forces generated by these events suggest that accelerations a few times the lunar surface gravity may have been produced throughout most of the crust. At depths greater than a few kilometers, these accelerations may be sufficient to remove by compaction most of the initial porosity associated with the brecciated regions beneath these older craters. The lack of clear relative age relationships between these craters and the last two impact basin-forming events allows this to be a

possible mechanism for removing the porosity beneath the craters presented in this chapter. However, the difficulty with any compaction process is that the present floors of these craters should have subsided  $\sim 2$  kilometers below the original floor levels; an amount inconsistent with the present depth/diameter ratios for these craters, though this difficulty may be alleviated by a simultaneous shallowing of the crater by the inward collapse of the crater walls initiated by the same strong ground motion.

## CHAPTER VI

## SHALLOW LUNAR CRATERS

Introduction

A second class of older lunar craters considered in this work are those which have crater depths much shallower than the depths of young lunar craters of the same diameter range. Of this class there are only two craters which have adequate topographic and gravity data coverage to determine a usable Bouguer gravity anomaly: Ptolemaeus and Hipparchus. The shallow crater Fra Mauro will also be considered in this chapter since it has a detected free-air gravity anomaly (Sjogren et al., 1974b) and since its geologic setting is very different from Ptolemaeus and Hipparchus. However, a radar topographic map is not yet available for Fra Mauro, so that topography derived from shadow measurements (Pike, 1976) must be used to place some restriction on the Bouguer gravity, but this is inadequate to compute a detailed topographic correction to the free-air gravity.

The nature and characteristics of the crater fill material responsible for the anomalously low depth/diameter ratios of these craters, as constrained by the lunar gravity data, is the main purpose of this chapter. A description of these craters is followed by a presentation of the Bouguer gravity and by a discussion of these results in terms of the results determined in the previous two chapters for other lunar craters.

### Description

Ptolemaeus and Hipparchus are pre-Imbrian in age since they are both clearly superposed by radial Imbrium Basin sculpture (Figure 19), though their relative ages with respect to the older lunar basins, in particular Serenitatis, is not clearly defined. Both of these craters lie within the nearside central lunar highlands within a crater diameter of mare regions whose emplacement postdates the formation of these craters. The circular rim structure of Ptolemaeus is almost completely unbroken, though it has been severely eroded by many small (~1 km) impacts (Figure 20). In contrast, major sections of the rim of Hipparchus have been totally removed by medium-sized impacts (~10 km) which suggests that Hipparchus (Figure 21) is significantly older than Ptolemaeus.

The major feature of these two craters which makes them distinct from most other lunar craters, especially those which belong to the youngest age class, that is those which are the least modified, are the very shallow depths of these craters for their diameters. Ptolemaeus has a rim-to-floor depth of 1.8 kilometers and Hipparchus a depth of 1.1 kilometers, much less than the 4.7 kilometer depth of young lunar craters of 150 kilometer diameter (Pike, 1974). This difference requires accounting for crater fill material amounting to three to four kilometers.

The floor levels of these two craters are approximately at the same level as Mare Nubium to the west and Sinus Medii to the north.

Figure 19. Lunar Orbiter photograph (IV-108-M) of the central lunar nearside. Ptolemaeus and Hipparchus (150 km) are shown in the bottom of this picture and the Imbrium Basin in the upper left corner. The Imbrium sculpture, appearing as linear features radial to Imbrium, is apparent in this photograph.



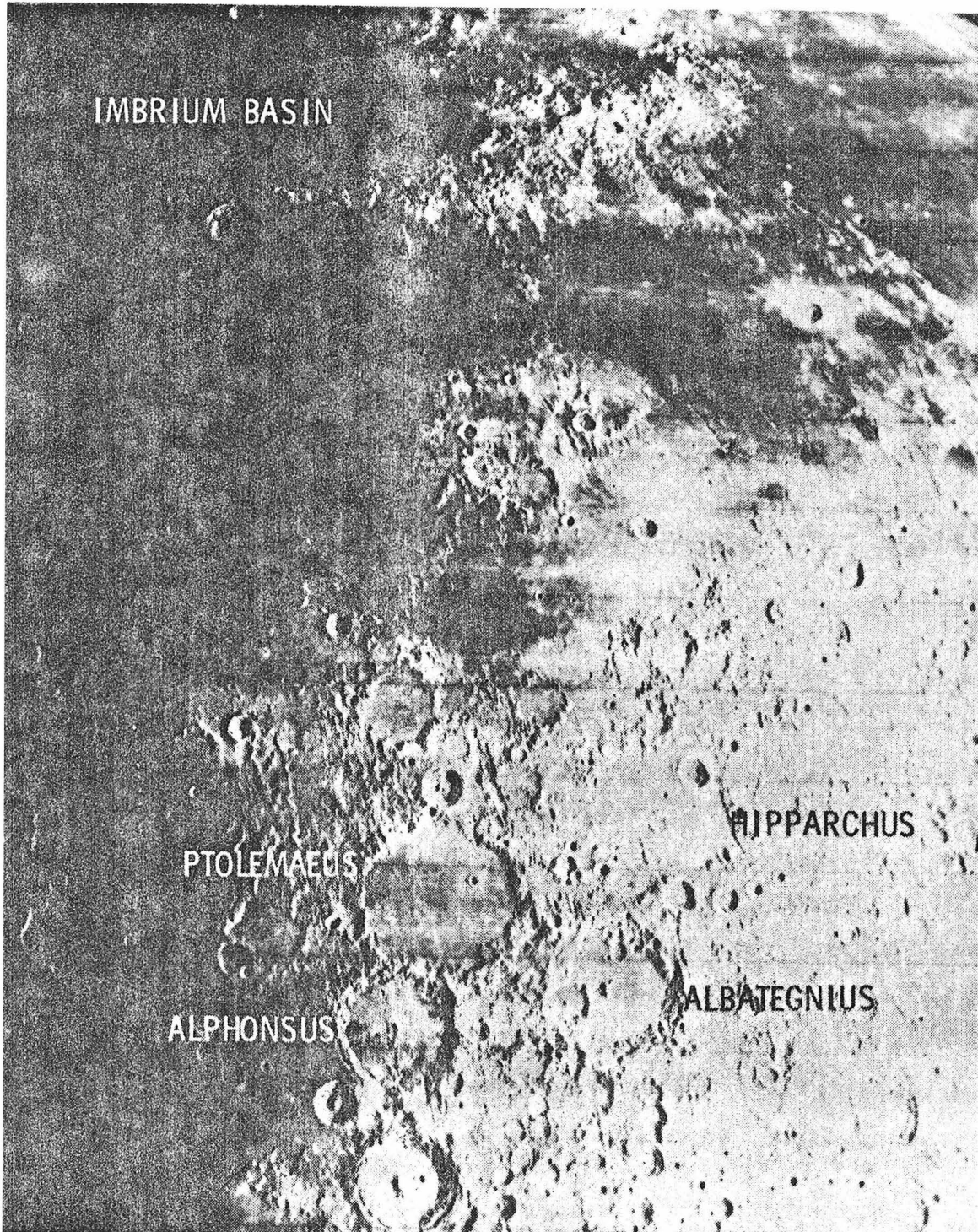


Figure 20. Apollo 16 metric photograph (AS16-989) of Ptolemaeus. North is to the top. Picture width is 170 kilometers. Note the smooth undulating appearance of the crater fill material.

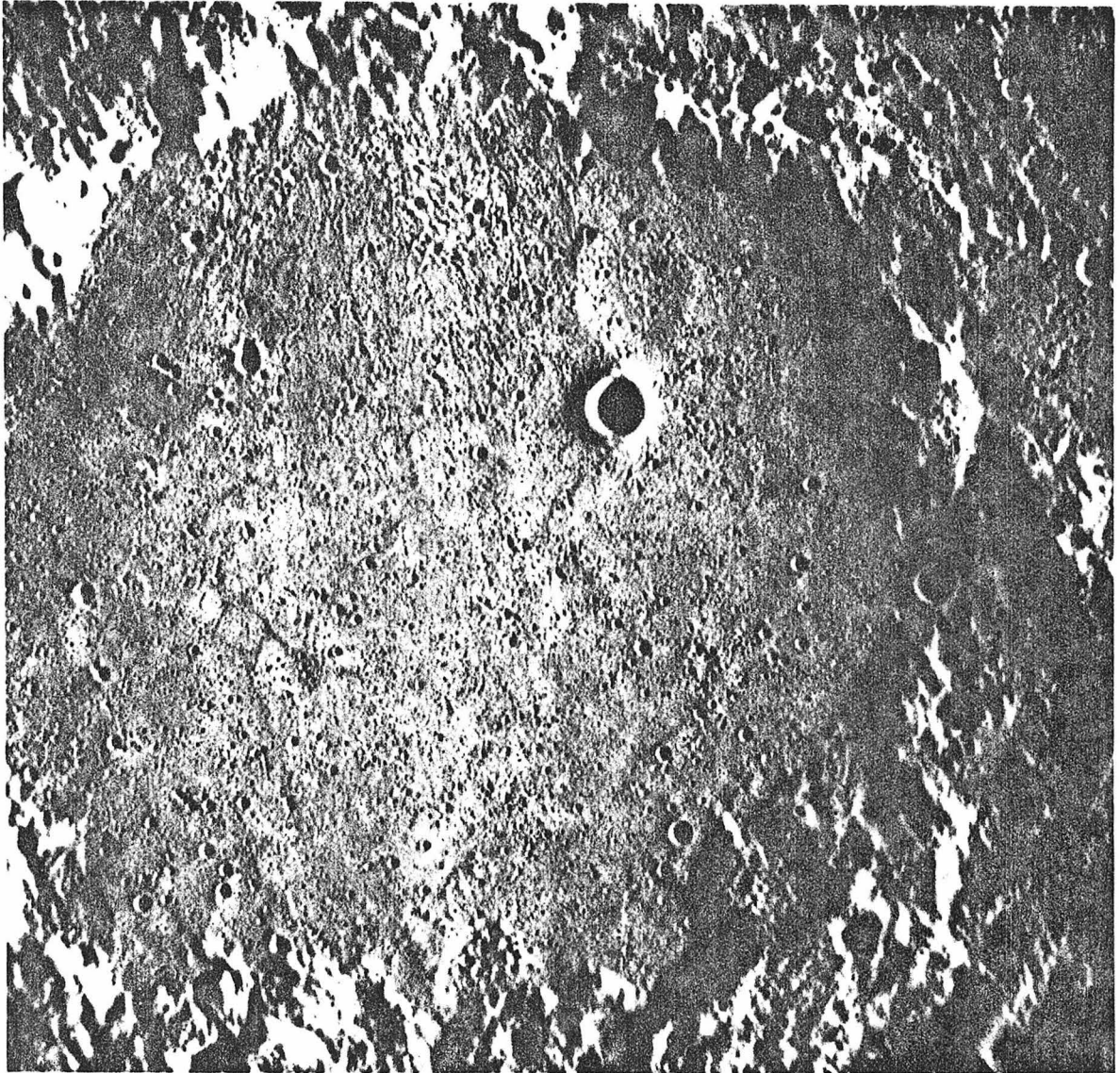
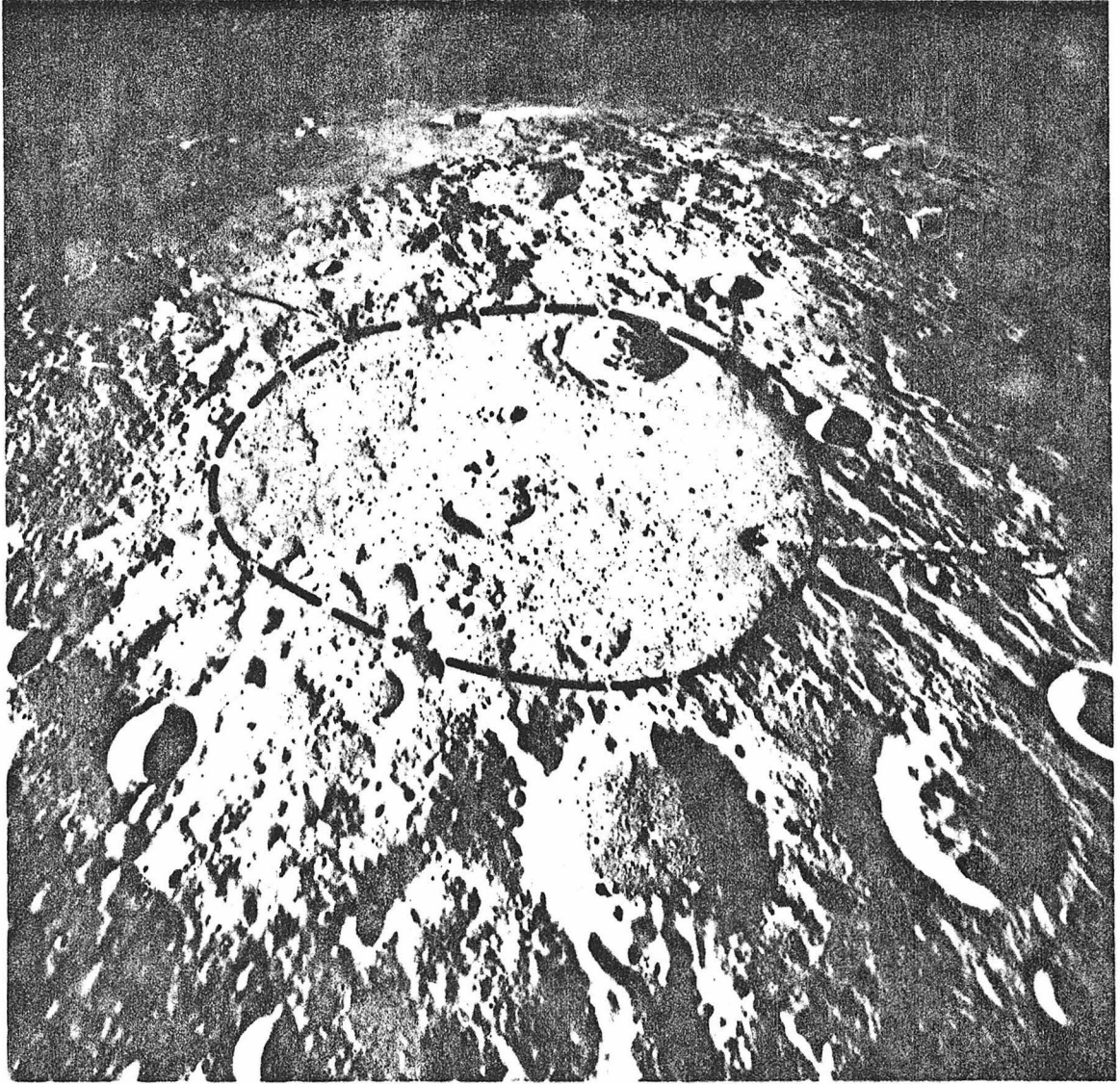


Figure 21. Apollo 16 oblique metric photograph (AS16-839) of Hipparchus (150 km). View is approximately to the north. The rim of Hipparchus is much **more** broken by later impacts than Ptolemaeus (Figure 19). Note the many small scattered peaks interior to Hipparchus.



The floors of two nearby pre-Imbrian craters of similar size, Alphonsus and Albategnius, lie 0.4 and 1.2 kilometers respectively below this level.

The floor material of Ptolemaeus and Hipparchus is characterized by a smooth slightly undulating surface with occasional small scattered peaks but no evidence of a dominating central peak, ruling out the possibility that this is simply the original crater floor uplifted to approximately the pre-impact level by some endogenic process, such as probably occurred at the crater Gassendi north of the Humorum Basin. This is further supported by the lack of rille structures or floor fractures associated with these crater floors (Schultz, 1976), structural features also associated with the floor of Gassendi. This crater fill material has a relatively high albedo, much higher than that typical for lunar mare regions though less than much of the lunar highlands, and represents a highly cratered surface, older than most of the lunar mare (Wilhelms and McCauley, 1971).

Prior to the return of lunar highland samples, these lunar light plains were interpreted to be the result of volcanic activity of a different character from the mare-style volcanism. However, the Apollo 16 landing, which was located at a site similar to the floor of Hipparchus, returned surface samples which were almost entirely impact-derived breccias (Muehlberger et al., 1972). Further studies have presented evidence for the origin of the lunar light plains by

fluidized ejecta deposited by the multiringed basins (Eggleton and Schaber, 1972), not the result of volcanic activity. In view of this, it may be expected that a sufficient thickness of low density material is deposited in Ptolemaeus and in Hipparchus to be detectable by the lunar gravity data.

The geologic setting of the pre-Imbrian crater Fra Mauro is very different from Ptolemaeus and Hipparchus. Fra Mauro lies adjacent to and is partly superposed by mare material, though the major surface material is probably Imbrium ejecta, similar to the light plains within the other two craters (Wilhelms and McCauley, 1971). Fra Mauro is comparable in size (95 km) to Ptolemaeus and Hipparchus, and, hence, had a similar initial depth, though its present depth of fifty meters (Pike, 1976), determined from shadow measurements, is much less than that of the two shallow highland craters. Fra Mauro is also situated about the same distance from the center of the Imbrium Basin as Ptolemaeus and Hipparchus, so that, any significant difference in the Bouguer gravity anomalies associated with these three craters is presumably due to their different post-impact histories which is chiefly controlled by their geologic settings.

#### Bouguer Gravity

The Bouguer gravity for Ptolemaeus and Hipparchus was determined in the manner described in Chapter III and the resultant profiles are shown in the Appendix. This analysis indicates a negative Bouguer anomaly associated with each of these two craters. In the same manner

as previously presented for the other lunar craters, Table VII lists the total mass deficiency,  $\Delta M$ , and the possible range of this parameter,  $\delta M$ , for each of these two craters. As can be seen from this table, the uncertainties in determining the Bouguer gravity is very large so that a wide range of possible models will fit the data. A comparison of these values of  $\Delta M$  for Ptolemaeus and Hipparchus are shown with  $\Delta M$  for the young lunar craters in Figure 22. Note that even within the large range of uncertainty, the values of  $\Delta M$  for these two shallow pre-Imbrian craters are significantly less than that for the young craters.

Employing the use of a simple model for these mass anomalies of a right cylinder 150 kilometers in diameter, that is, equal to the crater diameter, gives a surface density of  $-0.85 \text{ gm-cm}^{-3}\text{-km}$  for the nominal values of  $\Delta M$  for both Ptolemaeus and Hipparchus and a possible range from  $-0.3$  to  $-2.5 \text{ gm-cm}^{-3}\text{-km}$ . For a density contrast of  $-0.5 \text{ gm/cm}^{-3}$ , this corresponds to a range in thickness from 0.6 to 5 kilometers.

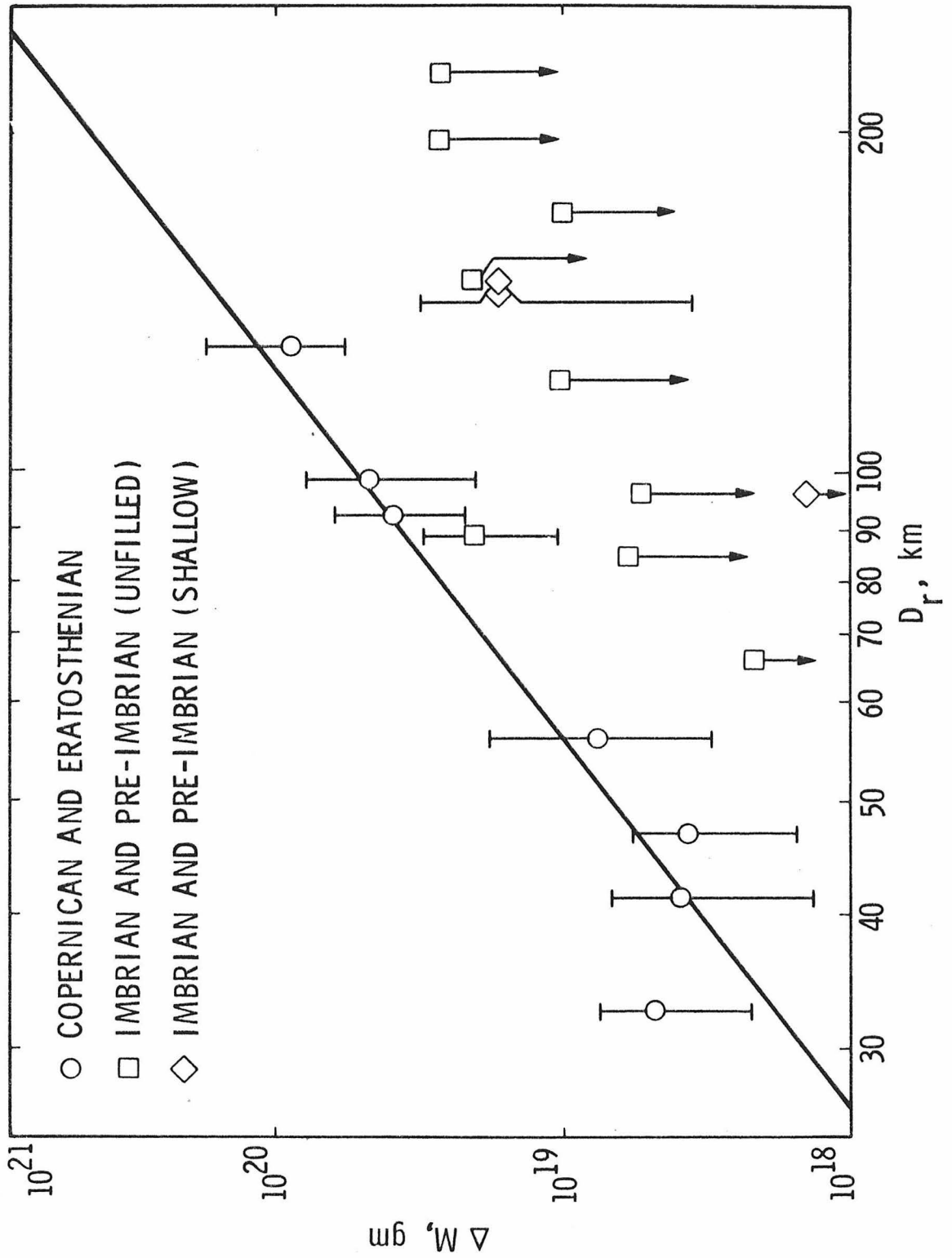
For Fra Mauro the nominal value for the surface density is considerably less. Modeling to the free-air gravity, a right cylinder with a diameter equal to the crater diameter gives a value for  $\Delta M$  of  $-1.6 \times 10^{18}$  grams which corresponds to a surface density of  $-0.2 \text{ gm-cm}^{-3}\text{-km}$ , slightly beyond the allowable range for the two shallow highland craters. If there is as much as fifty meters of negative



TABLE VII  
SUMMARY OF SHALLOW LUNAR CRATERS

NAME	DIAMETER (km)	TOPOGRAPHY meters	REGIONAL mgal	$\rho$ CRUST "PURE NOISE" mgal	$\delta g$ mgal	$\Delta M$ grams	$\delta M$ grams
Hipparchus	150	200	15	6	25	$-15 \times 10^{18}$	$-5/-45 \times 10^{18}$
Ptolemaeus	150	200	15	5	23	-15	-6/-40

Figure 22. Comparison of  $\Delta M$  values for Ptolemaeus and Hipparchus with values for young lunar craters and upper bound values of  $\Delta M$  for unfilled old lunar craters. The upper bound value of  $\Delta M$  determined from the free-air gravity for Fra Mauro (95 km) is also shown.



relief associated with Fra Mauro (Pike, 1976), then this is further reduced to  $-0.05 \text{ gm-cm}^{-3}\text{-km}$  which, within the uncertainties in the gravity and topographic data, is essentially zero, suggesting a zero Bouguer anomaly associated with Fra Mauro.

### Discussion

In the previous chapter, the analysis of two unfilled pre-Imbrian highland craters, Sacrobosco and Pasteur, indicated that these features had zero Bouguer anomalies. This implies that the gravitational effect of the porous breccia zones originally beneath these craters has been removed and, hence, suggests that the slight negative anomalies associated with Ptolemaeus and Hipparchus are not due to the breccia zones but due to another low density component, presumably the crater fill material derived from the ejecta of the Imbrium event. However, it is not possible to completely rule out the possibility that these slight negative anomalies are due entirely to remanent breccia lenses greatly reduced in porosity or in volume to the same degree as at the two unfilled highland craters since the upper bound of  $\Delta M$  for Sacrobosco and Pasteur are well within the range of possible values of  $\Delta M$  for Ptolemaeus and Hipparchus (Figure 22). This possible detection of the remanent breccia lenses at Ptolemaeus and Hipparchus and the lack of detection at the other two pre-Imbrian highland craters would be due to the lower spacecraft altitude over the former two craters.

However, the claim that these negative anomalies for Ptolemaeus and Hipparchus are due primarily to the crater fill material is supported by the value for the upper bound of  $\Delta M$  for Fra Mauro estimated

from the free-air gravity. Presumably, the low density crater fill material derived from material ejected by Imbrium is much thicker in Ptolemaeus and Hipparchus than in Fra Mauro, possibly due to the almost complete filling of Fra Mauro by mare material, similar to present day Plato or Archimedes, prior to the Imbrium event. Recall that at present there is a small patch of mare material within Fra Mauro which post-dates the deposition of the Imbrium ejecta.

## GRIMALDI: LUNAR MULTIRINGED BASIN

Introduction

It has been known for the past ten years that large positive free-air gravity anomalies, called mascons, are associated with mare-filled nearside basins (Muller and Sjogren, 1968). The mascons are generally thought to be shallow disk-shaped masses due to the mare fill (Conel and Holstrom, 1968; Phillips et al., 1972) or to a mantle plug (Wise and Yates, 1970; Bowin et al., 1975), though the relative contribution of these two components has been debated. Previous studies have been restricted to only a consideration of the free-air gravity data since adequate topographic coverage has not been available over these features to yield Bouguer gravity anomalies. Further, the large size of the lunar basins previously considered did not allow for adequate depth discrimination of the anomalous mass components. These two major difficulties are partially circumvented in the analysis of Grimaldi, the smallest known lunar mascon, since almost total topographic coverage is now available for this lunar basin and since the small size of this feature allows for a better discrimination of the depth of burial of the anomalous mass components.

Included in this chapter will be a brief description of the geologic setting of Grimaldi, a summary of the lunar gravity and topographic data, and a comparison of the lunar gravity data with several model calculations proposed for Grimaldi based on inferences

made about the structure of this basin from the surface geology. The final section discusses the results for Grimaldi in view of the analyses of the Bouguer gravity anomalies associated with lunar craters presented in the preceding chapters.

#### Description

Grimaldi is a multiringed basin, partially filled by mare material, which lies near the western limb of the Moon between the larger Orientale Basin to the west and the vast mare covered region of Oceanus Procellarum to the east. The local geologic setting of Grimaldi is shown in Figure 23. A generalized geologic and tectonic map of this same region is shown in Figure 24. The inner ring lies slightly outside the dark central patch of mare material; the outer ring is best preserved to the south and southeast (Figure 25). The diameter of the inner ring is roughly 200 kilometers and that of the outer ring about 400 kilometers. The radar topographic map of this area (Figure 26) shows that the region within the inner ring is 1.0 to 1.5 kilometers below the level of the immediate surroundings and the region between the two ring structures probably lies no more than a few hundred meters from the pre-impact level. The mare interior to Grimaldi is at a level 1.0 kilometer below the mare in Riccioli to the northwest and the mare in Oceanus Procellarum to the east.

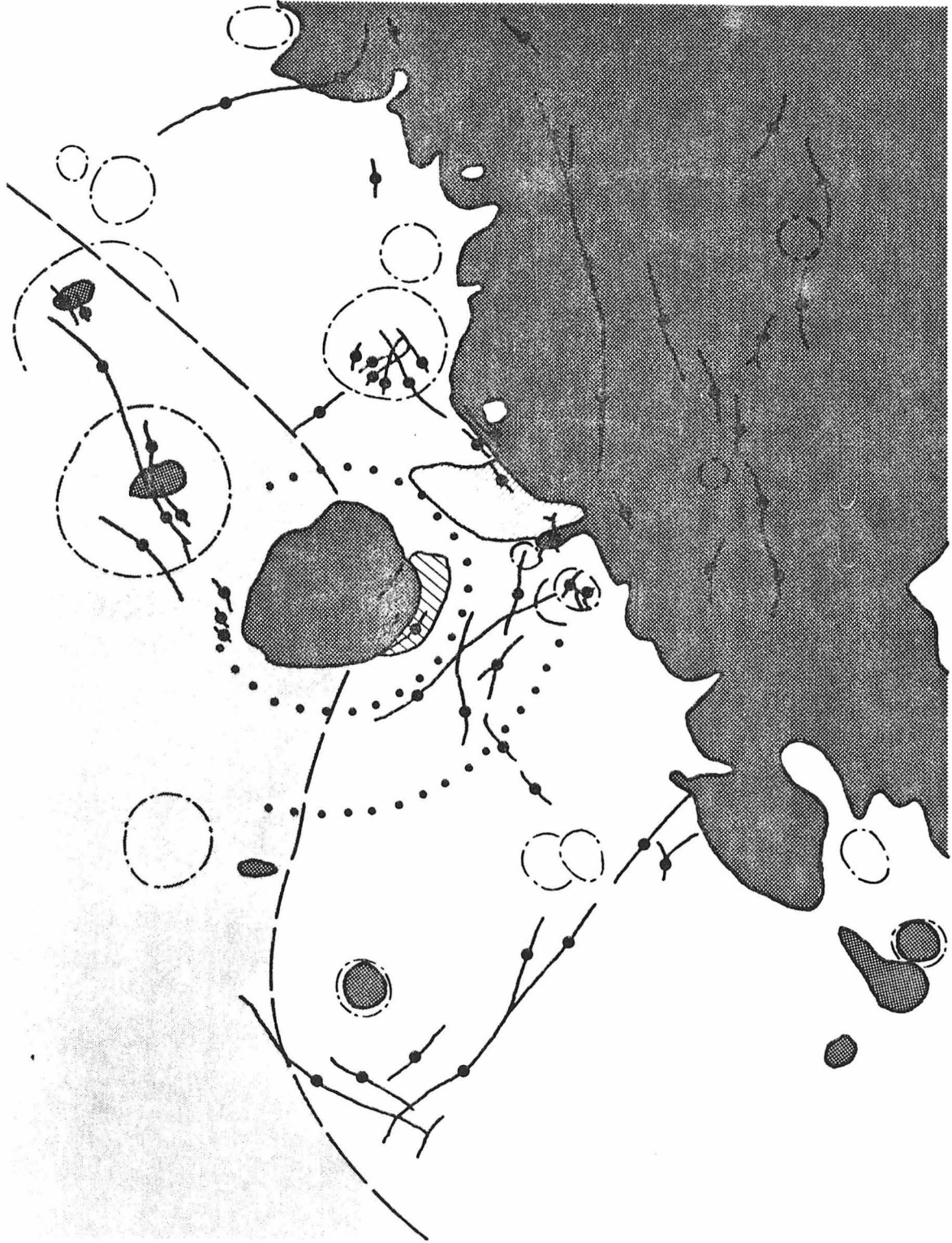
Grimaldi is pre-Orientale in age since the Hevelius Formation which has been interpreted as impact ejecta from the Orientale event,

Figure 23. Lunar Orbiter photograph (IV-161-M) of a portion of the western limb of the Moon centered at  $(2^{\circ}\text{S}, 65^{\circ}\text{W})$ . North is at the top. Grimaldi is the basin near the center of the photograph. The Cordillera Mountains, which form the outer ring of the Orientale Basin, are to the lower left and Oceanus Procellarum is the vast mare region to the right. The picture width is 900 kilometers.





Figure 24. Schematic geologic and tectonic map of the same region shown in Figure 23 highlighting the concentric ring structures of Grimaldi, regional mare ridge and straight lunar rille patterns, regions of mare volcanism, and possible remanent ejecta facies associated with the Grimaldi event.



EXPLANATION







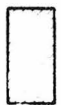

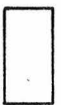
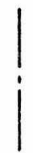
	MARE MATERIAL		RILLES
	ORIENTALE EJECTA (CONCENTRIC AND RADIAL FACIES)		SCARP (DOT ON DOWNTHROWN SIDE)
	GRIMALDI EJECTA (CORRUGATED FACIES)		MARE RIDGE
	GRIMALDI EJECTA (DOMICAL FACIES)		RING STRUCTURE
	UNDIFFERENTIATED HIGHLAND MATERIAL (INCLUDES SMOOTH PLAINS)		CRATER RIM CREST

Figure 25. Lunar Orbiter photographs (IV-161-H3 and IV-168-H3) detailing the multiringed basin Grimaldi. North is to the left. Total picture width (east-to-west) is 350 kilometers.

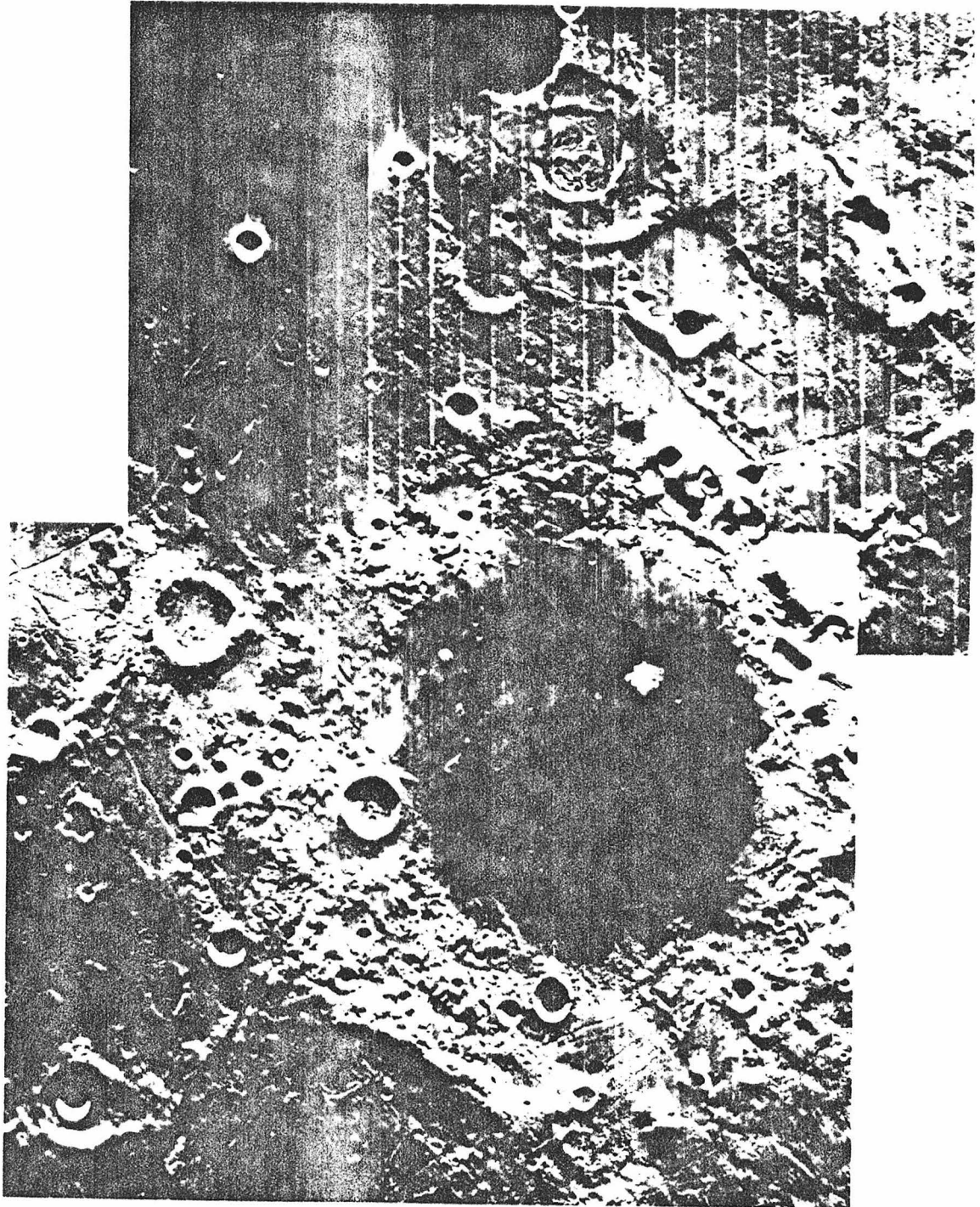
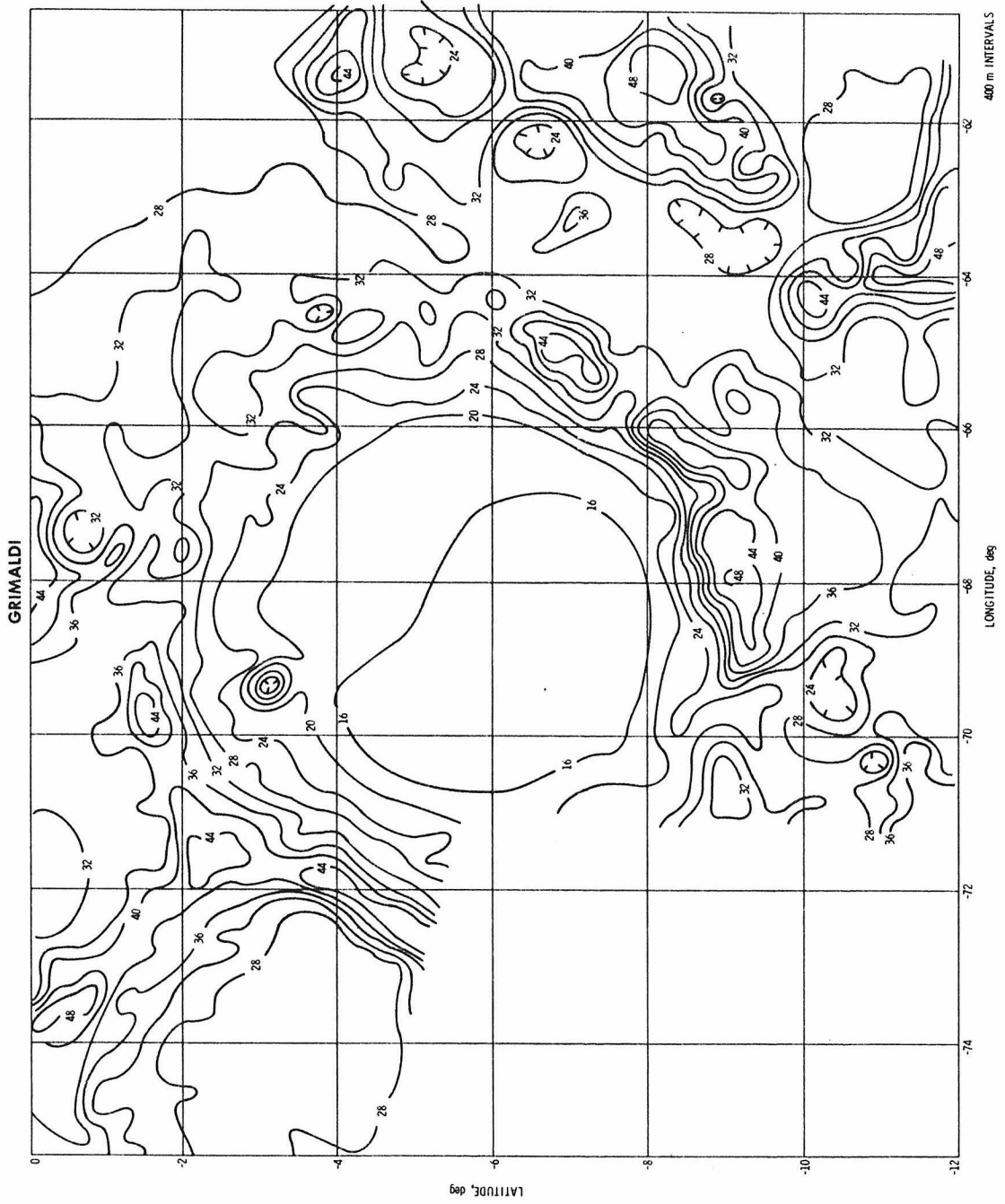


Figure 26. Earth-based radar topographic (ERT) map of Grimaldi provided by S. Zisk of the Haystack Observatory (slightly modified). This topographic map covers approximately the same region shown in Figure 25. The original map contour interval was 200 meters. It is evident from these two figures that the topographic crater bowl of Grimaldi is constrained within the inner ring structure.





analogous to the Cayley Formation surrounding Imbrium (Eggleton and Schaber, 1972), superposes Grimaldi in the west (Wilhelms and McCauley, 1971). Based on relative crater statistics Hartmann and Wood (1971) determined Grimaldi to be approximately contemporaneous with the Nectaris Basin.

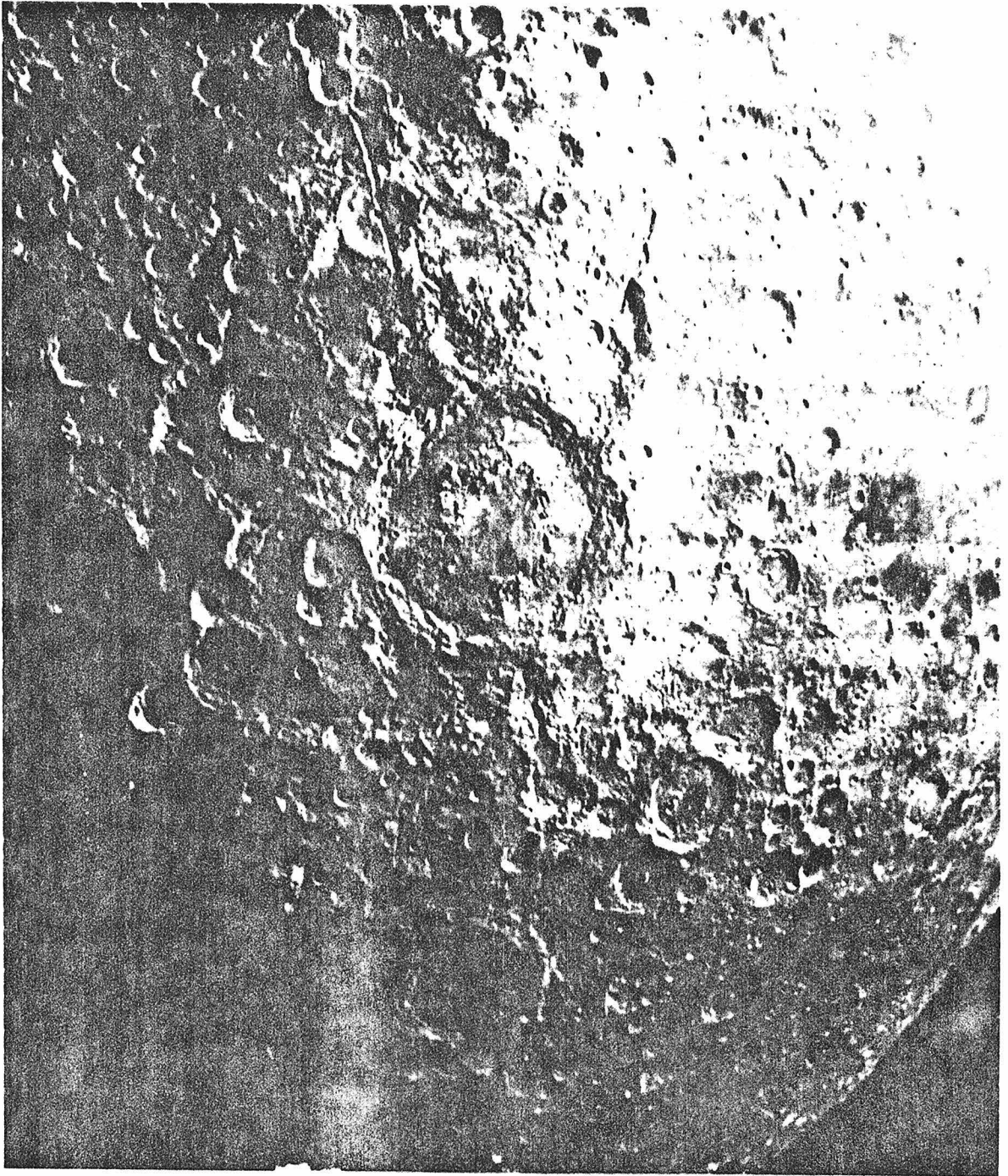
The inner ring of Grimaldi, which rises three kilometers above the level of the interior mare and to almost the maximum height reached by the outer ring, resembles the outer Rook Mountains of the Orientale Basin in that it is composed of a partial angular ring of massifs which lie exterior to a small region (Figure 25) which may correspond to the corrugated facies described by Head (1974) for Orientale. This small region is laced with large surface cracks though, possibly due to the more advanced stage of degradation, lacks the pitted and crackled appearance exhibited at Orientale.

Morphologically, the outer ring of Grimaldi is similar to the Cordillera Mountains, which form the outer ring of Orientale, in that they both have a steep inward facing continuous scarp which rises a few kilometers above the interior. A terrain similar to the domical facies between the outer Rook and the Corillera Mountains described by Head (1974), composed of rolling and hilly terrain with a slight radial texture and interpreted as fallback ejecta, also occurs between the inner and outer rings of Grimaldi to the northeast (Figure 25), though this may instead be a portion of the radial ejecta facies which surrounds the Orientale Basin (Moore et al., 1974).

The concentric two-ring structure of Grimaldi is not analogous to the two-ring structure of Schrödinger Basin (Figure 27), as had been suggested by Head (1977), since the outer ring of Grimaldi lacks any evidence of wall terracing which is well developed at Schrödinger and since the inner ring of Grimaldi does not lie within the major central depression as does apparently the inner ring of Schrödinger. Instead, as mentioned earlier, the inner ring of Grimaldi surrounds the major central depression. At Schrödinger the inner ring is probably a ring of expanded central peaks and the outer ring is the crater rim crest modified by terracing (Head, 1977). At Grimaldi there is no identifiable central peak ring lying within the central depression possibly due to the more advanced stage of degradation or more extensive interior volcanic flooding of Grimaldi than at other basins. On the basis of a comparison of the topography and the morphology of Grimaldi with Orientale and Schrödinger, the inner ring of Grimaldi is interpreted to approximate the crater rim crest.

The regional setting of Grimaldi is dominated by the Orientale event. At a distance of 900 kilometers from the center of Orientale, Grimaldi lies near the transition from the radial to smooth facies change on the Orientale ejecta (Moore et al., 1974). The radial facies is the result of a depositional process which partially filled pre-existing craters. Assuming that these craters had original depths similar to those of young lunar craters of the same diameter

Figure 27. Lunar Orbiter photograph (IV-008-M) of Schrödinger Basin (320 km diam) located in the center of this picture. North is approximately to the top. Note the inner ring of discontinuous peaks and the terracing of the interior wall of the outer ring.



range, Moore et al. (1974) have estimated the thickness of the Orientale ejecta at the distance of Grimaldi to be 0.5 to 1.0 kilometers. The origin and extent of the smooth facies is somewhat uncertain (Moore et al., 1974). The occurrence of lobate scarps in the smooth plains allows a thickness of a few hundred meters to be measured for individual units within this facies.

The post-impact history of the Grimaldi region is dominated by three events. The first is the formation of the large Orientale Basin to the west which not only deposited material at Grimaldi ranging in thickness from a few hundred meters to a kilometer but also probably greatly modified the pre-existing tectonic grid of the western limb of the Moon. A second major geologic event was the vast volcanic flooding of Oceanus Procellarum to the east and the extrusion of isolated pockets of volcanic material in the highlands, including volcanic flooding of the region interior to the inner ring of Grimaldi, and the possibility of major intrusive activity throughout this region. Evidence for the earlier occurrence of volcanic activity at Grimaldi would have been mostly destroyed by the Orientale event. The age of the last flow units which cover the region within the inner ring of Grimaldi are estimated from crater statistics to be  $3.0 \pm 0.1 \times 10^9$  years (Boyce, 1976), contemporaneous with the last major volcanic flooding of Oceanus Procellarum and representing some of the youngest volcanic units on the surface of the Moon. The

third major event is the formation of straight lunar rilles, which are interpreted to be the result of a tensional stress field, throughout most of the lunar highlands around Grimaldi, though a direct relationship with this basin is not apparent. Most of the stratigraphic evidence indicates that the formation of most of these rilles postdate Orientale and predate the emplacement of the mare, however, earlier rilles may have been destroyed or covered by the Orientale event. In a few cases, particularly the isolated patches of mare material in the highlands such as Riccioli, lunar rilles postdate the mare material. Young craters which are superposed on these rilles are undisturbed by them.

There is no surface evidence of major long-term adjustment of the lunar crust to the Grimaldi event. The outer ring structure has not deformed or disrupted lunar rilles which formed after Grimaldi and has not deformed mare material in Oceanus Procellarum emplaced across an extension of the outer ring structure. Several mare ridges are present in the mare interior to Grimaldi. These may be compressional features (Baldwin, 1968) or possible source regions (Strom, 1972) for the mare material. The interior of Grimaldi lacks any other structures, such as, irregular depressions or modified floors of small craters, which could be interpreted as possible source regions (Figure 25). The lack of identifiable flow fronts may be the result of a combination of factors controlling the rate of extrusion of lava (Schaber et al., 1976) resulting in many thin flows of large areal extent.

### Model Calculations

In this section the results of several model calculations are compared with the Bouguer gravity. The various components for the anomalous masses are assumed to be circularly symmetric with respect to Grimaldi. The components of the regional gravity field contributed by the mare material in Oceanus Procellarum or the Orientale ejecta blanketing Grimaldi have not been taken into account, though they will contribute to the background level of the lunar gravity field. Since regional components to the local gravity field are not being considered, all model calculation are adjusted to an arbitrary background level to best reproduce the peak-to-peak variation in the Bouguer gravity.

In these calculations the shape of each proposed anomalous mass component is prescribed and the density contrast required to reproduce the Bouguer gravity is solved from the gravity data. The geometry of each component has been taken to be either a right cylinder or a truncated cone. When the thickness of the cylinder or cone is much smaller than its diameter, for a particular diameter and depth of burial of that component, the density and thickness cannot be determined independently, only the density-thickness product.

A study of the Lunar Orbiter photograph shown in Figure 23 and the accompanying map in Figure 24 reveals several geologic units which may have different bulk densities due to either compositional or porosity variations. The density of most of the lunar crust,

determined from the low harmonics of the gravity field, is probably in the range of 2.7 to 2.9 gm/cm<sup>3</sup> (Solomon, 1974; Bills and Ferrari, 1977), though regions of the upper crust may be slightly less dense due to the continual process of cratering. Laboratory measurements of the bulk density of lunar samples returned from the mare regions of the Moon give values in the range of 2.9 to 3.4 gm/cm<sup>3</sup> (Talwani et al., 1973). Densities of returned highland samples are less and range from 2.4 to 2.8 gm/cm<sup>3</sup>. At the lower end of these highland density values are samples which were probably crushed and fractured and subsequently ejected by impact events. The bulk density of impact ejecta may be considerably less, 2.0 gm/cm<sup>3</sup>, since this may consist of a significant volume of fine grain material. At most, the thickness of this ejected material from the largest impacts on the Moon is estimated to be a few kilometers (Short and Forman, 1972; McGetchin et al., 1973) and occurs as patches of light plains material surrounding the most recent multiringed basins. In addition, it has been suggested that there is a possible component to the gravity anomaly of lunar mascons contributed by the lunar mantle (Wise and Yates, 1970). Since the lunar mantle comprises the bulk of the volume of the Moon, its density must be close to the mean density of the Moon, that is, 3.4 gm/cm<sup>3</sup> (Bills and Ferrari, 1977). In summary, there are three possible components associated with Grimaldi which have densities which are anomalous to the density of the normal lunar crust. Briefly stated, the central mare fill and

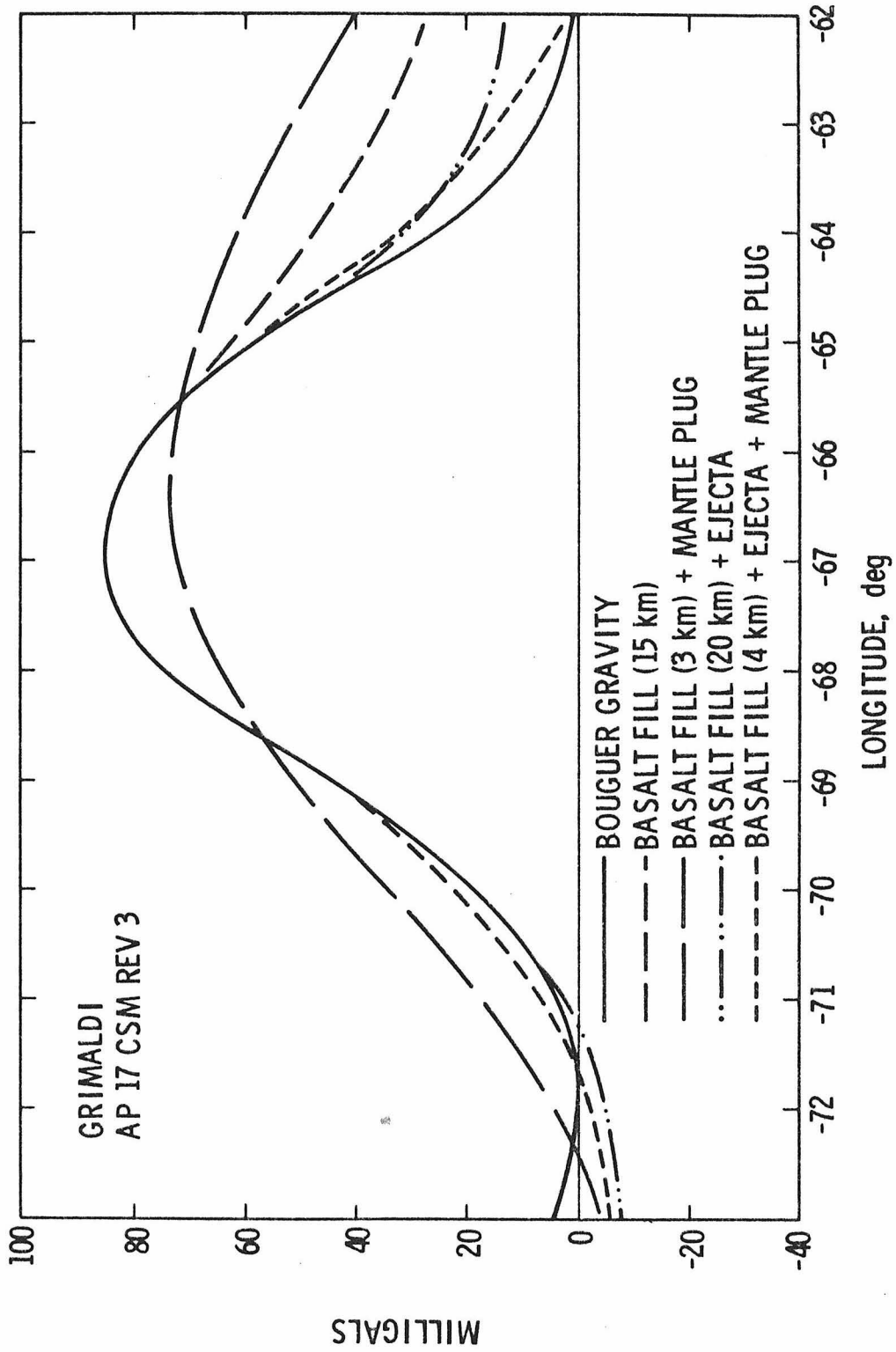


associated intrusive material may have a density contrast with the lunar crust of +0.1 to +1.0 gm/cm<sup>3</sup>, the density contrast between the lunar mantle and crust is probably in the range of +0.6 to +1.1 gm/cm<sup>3</sup>, the density contrast of the low density component due to material crushed and brecciated by the impact may be as much as -0.4 gm/cm<sup>3</sup>, and that due to ejected material as much as -0.8 gm/cm<sup>3</sup> corresponding to an increase in porosity of 30%.

In each of the calculations to be presented, a component has been included which represents the mare fill with various combinations of possible contributions from ejecta or brecciated material and from the lunar mantle. Each of these calculations are compared with the Bouguer gravity profile shown in Figure 28. The characteristic of each model will be discussed shortly. Similar results to those shown in Figure 28 have been obtained for the other orbits used in this analysis, so that, within the uncertainties of this analysis, the various models shown in Figure 28 cannot be distinguished by the inclusion of multiple orbits.

The simplest model shown in Figure 28 has only one component which represents the circular mare fill in Grimaldi. This model requires at least fifteen kilometers of mare fill to account for the magnitude of the gravity anomaly. This is rejected as a reasonable model since a comparison of the present depth of Grimaldi (1.0 km) with the depths of unfilled lunar basins, such as Mendeleev (6 km, Kaula et al., 1973), gives a maximum estimate of three to five

Figure 28. A comparison of the Bouguer gravity profile across Grimaldi with the results of several model calculations described in the text.



kilometers for the thickness of mare material within Grimaldi. Further, this single component model is unable to fully reproduce the eastern end of the Bouguer gravity profile.

The next model listed in Figure 28 attempts to reduce the amount of required mare fill to a reasonable value by the addition of a separate high density component representing a mantle plug at a depth of sixty kilometers. However, the introduction of a high density component at any depth has the consequences of broadening the gravity profile as shown in Figure 28. What is also required is a component which can narrow the gravity signature. This can be accomplished by a ring or annulus of low density material such as that which may be contributed by the ejecta deposited by the formation of Grimaldi.

For these calculations, the region between the two concentric rings is taken as the extent of the bulk of ejecta surrounding Grimaldi, that is, the maximum lateral extent continues outward approximately one crater radius beyond the rim crest, a scaled distance similar to the lateral extent of the continuous ejecta around large lunar craters (Gault et al., 1975). Ejected material certainly extends beyond this distance and must comprise most of the relief of the outer ring since structural uplift of the rim is confined to occur within one-half a crater radius of the rim crest (Roddy et al., 1975; Carlson and Jones, 1965). By increasing the

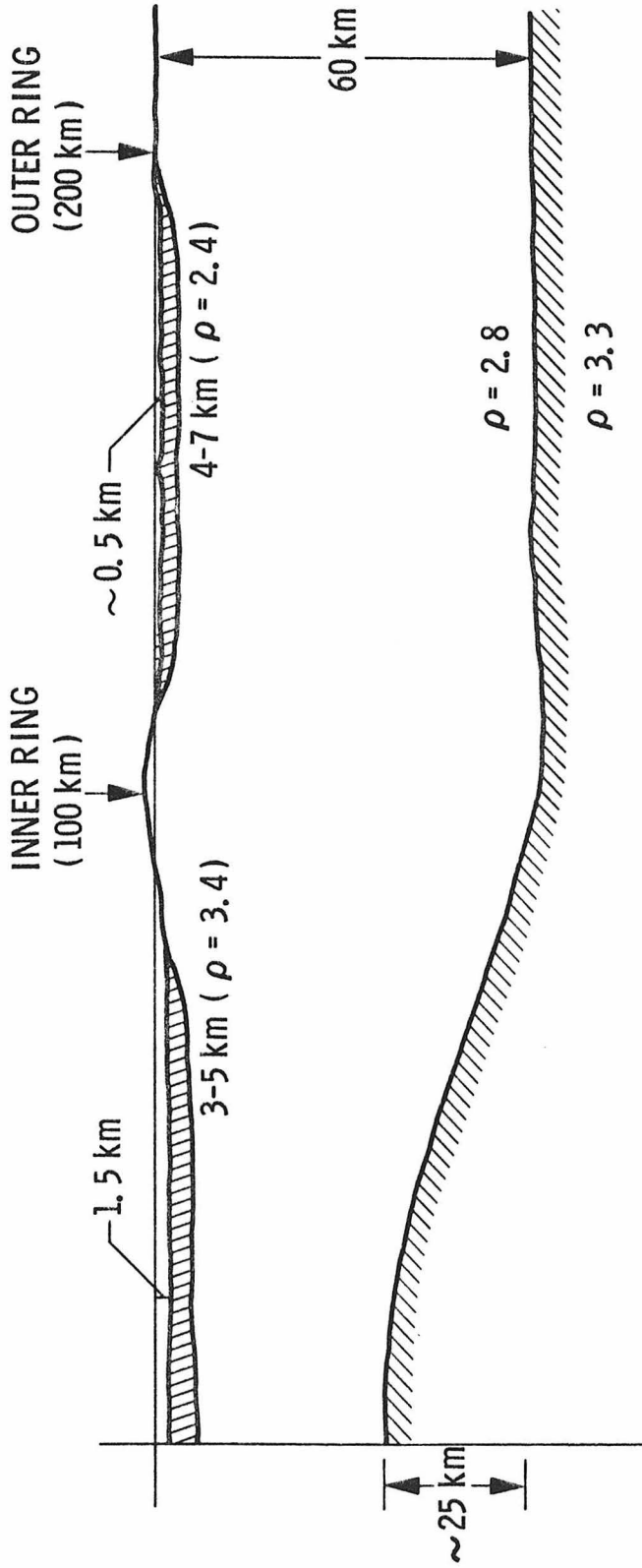
maximum radial extent of this annulus in these model calculations, a lower areal density would be determined such that the net mass deficiency of this component would remain approximately constant. A low density component may also be present within the inner ring, however, the gravitational effect of this component is being masked by the mare fill. For a model consisting of only the mare fill and a ring of ejecta, it is possible to adequately reproduce the observed gravity signature (Figure 28), but again this requires an unrealistic amount of mare fill, approximately twenty kilometers.

The fourth model calculation shown in Figure 28 is a combination of all three components. This gives a realistic value for the amount of mare fill and adequately reproduces the gravity profile. The details of this model are shown in Figure 29. It consists of three to five kilometers of mare fill surrounded by a very thick low density ring with a surface density of  $-2$  to  $-4 \text{ gm-cm}^{-3}\text{-km}$ . The third component is a high density plug of material here interpreted as uplifted lunar mantle material. The lateral extent of this third component is poorly constrained by the gravity data, however, if it is confined to lie within the inner ring then it has a vertical relief of twenty to thirty kilometers.

By fixing the amount of mare fill to that determined by the fourth model described above, that is, four kilometers, there is a slight trade off between the other two anomalous mass components.

Figure 29. Schematic cross-section of Grimaldi determined from the gravity data and consistent with the surface geology. Horizontal and vertical scales are the same.

# GRIMALDI



Modeling the mantle plug as a thin disk with a 100 kilometer radius and the ejecta as a thin annulus with inner and outer radii of 100 and 200 kilometers, respectively, the acceptable variation in the density-thickness product of these two components necessary to reproduce the Bouguer gravity profile is listed in Table VIII. The pre-mare isostatic model, that is the model in which the density-thickness product of the mantle plug and the pre-mare crater bowl is approximately equal, is indicated. In this calculation, the pre-mare crater depth was taken to be five kilometers and the density of the lunar crust to be  $2.8 \text{ gm/cm}^3$ . All other acceptable models listed in Table VIII are sub-isostatic, that is, there is insufficient high density material at depth to balance the interior differential stress produced by the crater bowl, before the emplacement of the mare material. Assuming a value for the density contrast between the lunar mantle and crust, a mass balance calculation can be performed to determine the thickness of the ejecta and the density contrast between the ejecta and the lunar crust. A pre-mare crater depth of five kilometers gives a crater volume of  $1 \times 10^5 \text{ km}^3$ .

The volume of the mantle plug and the corresponding thickness of ejecta have been determined and are listed in Table VIII. In all cases, the ejecta thickness must be several kilometers. By extending the outer radius of the low density annulus to 250 kilometers, the thickness of this component can be reduced by 40%. And from the density-thickness product for the annulus of ejecta, a density contrast may be easily computed (Table VIII) and compared with expected values discussed earlier.



TABLE VIII

## GRAVITY MODELS FOR GRIMALDI

	<u>Density-thickness product (gm-cm<sup>-3</sup>-km)</u>		
Ejecta Ring	-4	-3	-2
Mantle Plug	10	13	16*
Volume of Plug ( $\Delta\rho = +0.7 \text{ gm/cm}^3$ )	$4 \times 10^5 \text{ km}^3$	$5 \times 10^5$	$9 \times 10^5$
Ejecta Thickness	6 km	6.5	7
$\Delta\rho$ ejecta	$-0.7 \text{ gm/cm}^3$	-0.5	-0.3

\*Isostatic model

Discussion

An analysis similar to the one presented here for Grimaldi has been conducted for Orientale by Sjogren and Smith (1978). However, since adequate topographic coverage of the Orientale Basin was not available, they restricted their analysis to a consideration of only the free-air gravity. They also proposed a three component model for Orientale consisting of the same components presented here for Grimaldi, that is, a central thin surface disk representing the interior mare surrounded by a low density ring and a third component of high density material placed at depth. They interpret the low density ring as due to the topographic low of the basin structure. Part of this component may also be due to ejecta deposited around the basin by the Orientale event.

Up to now the high density region at depth has been interpreted to be due to lunar mantle material uplifted beneath the basin. An alternative interpretation is that this represents intruded igneous material. Erlich et al.(1974) have proposed this as an explanation for all lunar mascons drawing upon a possible similarity with the densely intruded crustal material beneath terrestrial volcanic calderas. However, this explanation for lunar mascons does not account for both the association of these positive anomalies with only mare-filled multiringed basins and the presence of zero Bouguer gravity anomalies with old lunar craters (see Chapter V), some of which are

comparable in size to Grimaldi and includes one whose floor is completely covered by mare material.

An adequate explanation for the association of high density material with lunar basins should also account for the absence of this same component beneath large lunar craters of comparable size. The diameters (~200 km) and depths (~3 km) of the lunar craters Pasteur and Humbolt are similar to Grimaldi, taking the inner ring structure of Grimaldi as the crater diameter in accordance with the arguments presented earlier in this chapter. Since all three of these impacts resulted in similar size craters, the basic difference in their structures is the presence of an outer concentric ring around Grimaldi. The morphology of this outer ring, a steep inward facing slope of a few kilometers relief, suggests that this feature represents a fault scarp. A similar interpretation has been made by Hartmann and Wood (1971) for the origin of the outer rings around other lunar basins. From an examination of large terrestrial impact structures, the absolute displacement along this scarp is predominantly with the region between the inner and outer rings downward and collapsing inward toward the crater bowl uplifting the central portion, which for Grimaldi includes uplifted material of the lunar mantle, in a manner similar to that described as floor failure by Melosh (1977). The amount of vertical uplift at Grimaldi is probably twenty to thirty kilometers, approximately 10% of the crater diameter, a proportional amount to that determined for the amount of uplift associated with several terrestrial impact structures (Howard et al., 1974).

Summary

Grimaldi is a small multiringed basin lying on the western limb of the Moon. It has the notoriety of being the smallest known lunar mascon. This distinction enables the use of the existing lunar gravity and topographic data to better define the subsurface structure of these types of lunar features. In rough numbers, the present free-air gravity over Grimaldi at an altitude of 70 kilometers is +60 milligals (Table IX). The crater bowl contributes -30 milligals so that the present Bouguer gravity has a value of +90 milligals. If the basalt fill (three to five kilometers) is stripped away, then the pre-mare free-air gravity was -120 milligals, the crater bowl contributed -190 milligals leaving a positive Bouguer anomaly of some +70 milligals. Furthermore, if Pasteur and Humboldt, two lunar craters of similar diameters to Grimaldi, were filled with mare material to the same depth as is presently within Grimaldi, that is, one kilometer below the pre-impact level, these two craters would still have slightly negative free-air gravity anomalies of -10 to -20 milligals at an altitude of 70 kilometers; they would not be mascons. The association of a positive Bouguer anomaly with a multiringed basin and the lack of positive anomalies associated with large lunar craters, comparable in size to Grimaldi, suggests that this component was produced in connection with the formation of the concentric ring structure. Possibly this positive anomaly is due to higher density lunar mantle material centrally uplifted by the

TABLE IX  
GRAVITY VALUES FOR GRIMALDI--PAST AND PRESENT  
(Spacecraft Altitude 70 km)

	<u>Present</u>	<u>Pre-Mare</u>
Free-air Gravity	+60 mgal	-120 mgal
Crater Bowl	-30	-190
Bouguer Gravity	+90	+70

inward collapse of material which formed the concentric outer ring. In order to fully reproduce the gravity data over Grimaldi, a third anomalous mass component is required consisting of a low density annulus which may represent several kilometers of ejecta surrounding Grimaldi.

## CHAPTER VIII

## NON-IMPACT FEATURES

Introduction

In the previous four chapters, the gravity anomalies associated with lunar impact features, representing a wide range of sizes and ages, were discussed. In this chapter, the anomalies associated with two non-impact features, Lamont and Marius Hills, will be examined and viewed in terms of their inferred geologic histories and their association with various tectonic elements. These two sites are regions in the irregular lunar mare which, though they are very distinct from each other in their morphologic forms, are probably both locations of intrusive activity within the lunar crust. Both have positive free-air gravity anomalies associated with them and neither are obviously related to impact events, though their locations may have been structurally controlled by major impacts early in lunar history.

In turn, a description of Lamont and of Marius Hills will be presented and immediately followed by an analysis of the gravity data across each feature and a discussion of these results contrasting the different geologic and tectonic settings of each site.

## LAMONT

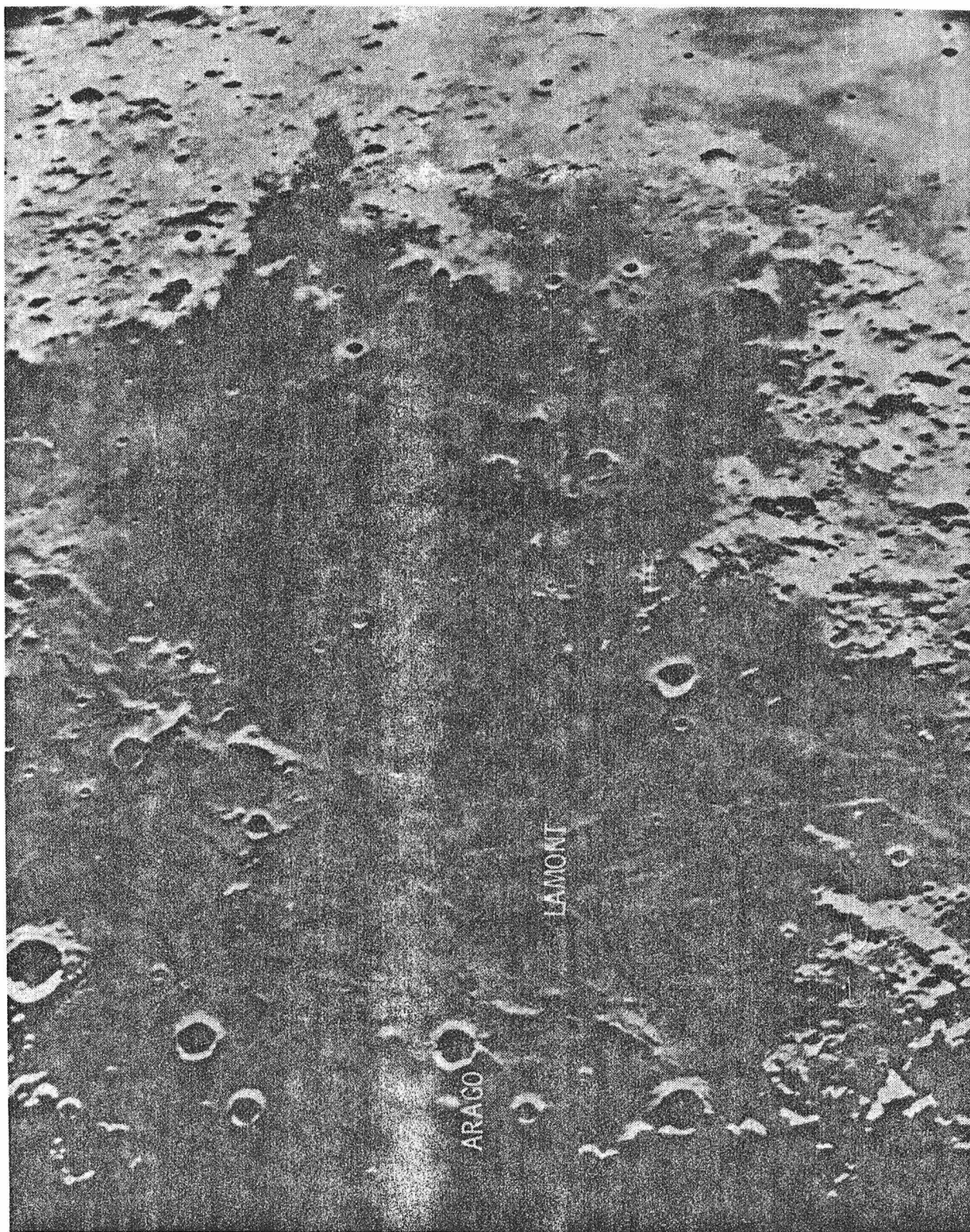
Description

The Lamont structure, located in the southern half of the irregular mare in western Tranquillitatis, is defined by a circular mare wrinkle ridge pattern surrounded by a set of radial or linear mare ridges trending primarily north-south (Figure 30). The circular ridge pattern consists of two incomplete, roughly concentric rings with inner and outer diameters of 60 and approximately 120 kilometers. All mare ridges in this region of the Moon are interpreted here as compressional features since their basic morphologic form—an intensely crumpled and irregular ridge crest, producing foreshortening of some small craters, superposed on a broader structural arch (Bryan, 1973)—is reminiscent of a predominantly east-west compressional stress field. More importantly, the interpretation of a compressional stress environment is suggested by a lack of tensional features, such as straight lunar rilles or coalescing rimless or collapse depressions, along or in line with these ridge crests. The small irregularly distributed and oriented crater chains in western Tranquillitatis noted by Morris and Wilhelms (1967) are probably localized volcanic vents and secondary impact crater chains produced, primarily, by the large crater to the south, Theophilus.

The mare in western Tranquillitatis has a high lunar abundance of titanium oxide, revealed by Earth-based spectral reflectivity measurements (Johnson et al., 1977), and a very old age ( $3.6 \pm 0.1 \times 10^9$  years),



Figure 30. Earth-based photograph of the irregular mare region of Tranquillitatis. North is to the left of the page. Lamont is the circular ring of mare ridges accentuated by the predominantly north-south trending, roughly radial, mare ridges. Note the dome structures west and north of the crater Arago and the straight lunar rilles to the south of Lamont near the site of the Apollo 11 landing. The western lunar rilles mentioned in the text are in the shadow portion of this photograph.

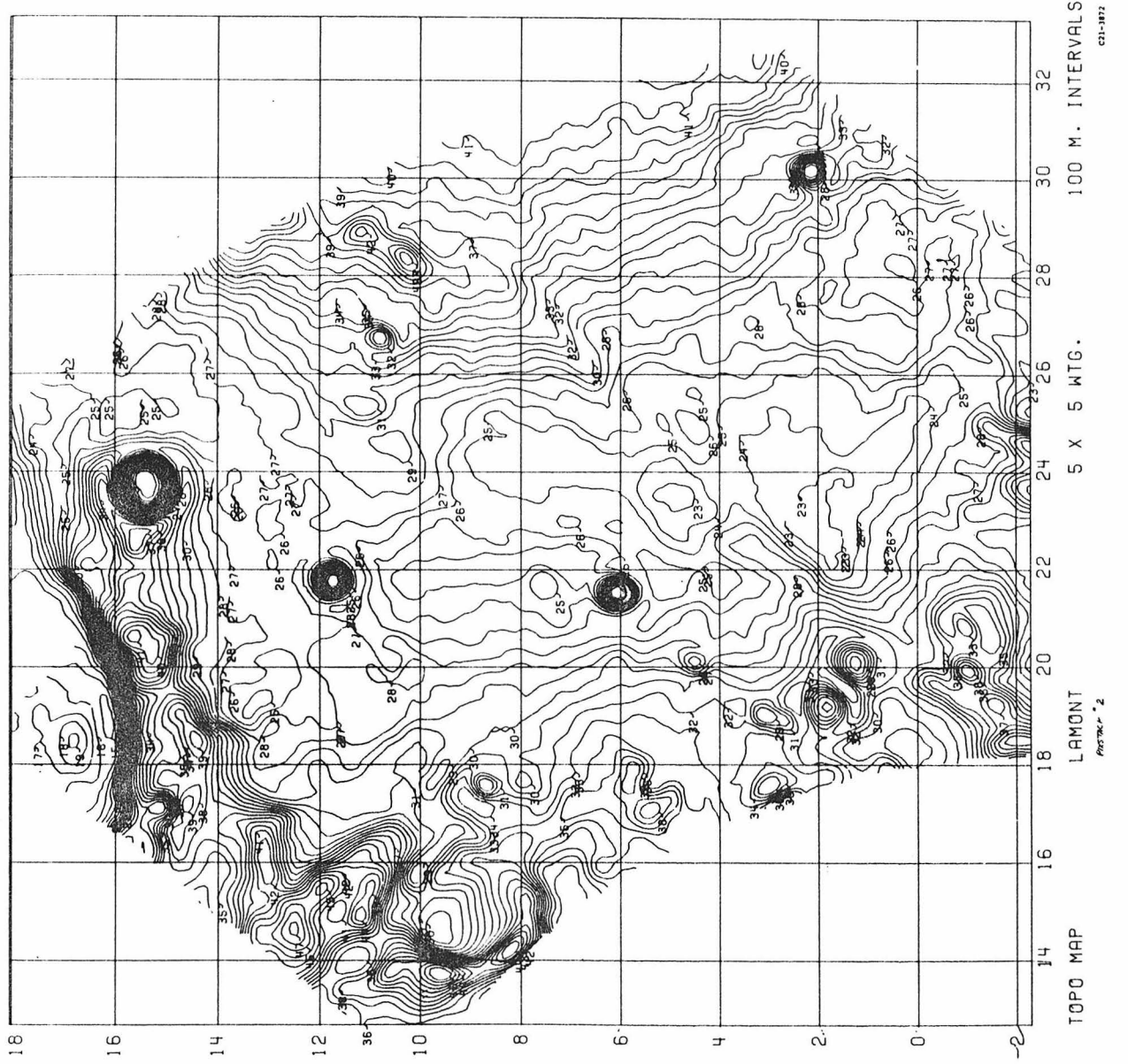


determined by a small crater morphology technique (Boyce, 1976), though slightly younger than the mare region sampled at the Apollo 11 landing site to the south of Lamont.

At Lamont, there is no indentifiable highland material protruding through the mare as there are at several other circular mare wrinkle ridge features, such as Reiner R and Flamsteed P, both in Oceanus Procellarum. The only candidate non-mare material in this region are the dome structures, appearing in low sun angle photographs (Figure 30), lying to the west and to the north of the crater Arago. These domes vary from a few kilometers up to twenty kilometers in diameter with the largest dome reaching to a height of a few hundred meters. All domes have gentle slopes and, at Earth-based resolution, ill-defined contacts with the surrounding mare. The presence of these domes suggests the occurrence of a style of lunar volcanism different from the emplacement of the vast mare plains, possibly due to a combination of changes in eruptive conditions such as a slight change in chemistry or lower temperature of the erupted magma or due to a lower magma supply rate caused by a smaller or a deeper magma reservoir.

Structurally, Lamont is a closed depression occupying a position in a much larger regional trough aligned roughly north-south (Figure 31). This closed depression is primarily confined to the inner circular ridge pattern of Lamont. The linear mare ridges lie totally within the regional trough, further indication of a

Figure 31. Earth-based radar topographic map of the Lamont region of the Moon provided by S. Zisk. Contour interval is 100 meters. Lamont is the small depression located at  $23.5^\circ$  longitude and  $5^\circ$  latitude. Note the large north-south trough which dominates most of western Tranquillitatis extending from zero to  $12^\circ$  latitude.



11/10/1976

compressional origin for these ridges which probably resulted from a regional faulting and buckling of the lunar crust, and are paralleled by a system of lunar rilles to the immediate west excluded from this trough and interpreted as surface extensional features. The lunar rilles to the south (Figure 30) may not be related to the Lamont structure, but may be a continuation of a northwest-southeast trending rille system extending from Mare Vaporum to Mare Fecunditatis (see Scott et al., 1975). The north-south trending rilles are up to several kilometers wide and cut across both mare and highland terrain. There is no clear stratigraphic relationship between these rilles and the mare ridges; both postdate the major emplacement of mare material in western Tranquillitatis and may be contemporaneous.

#### Geophysical Data

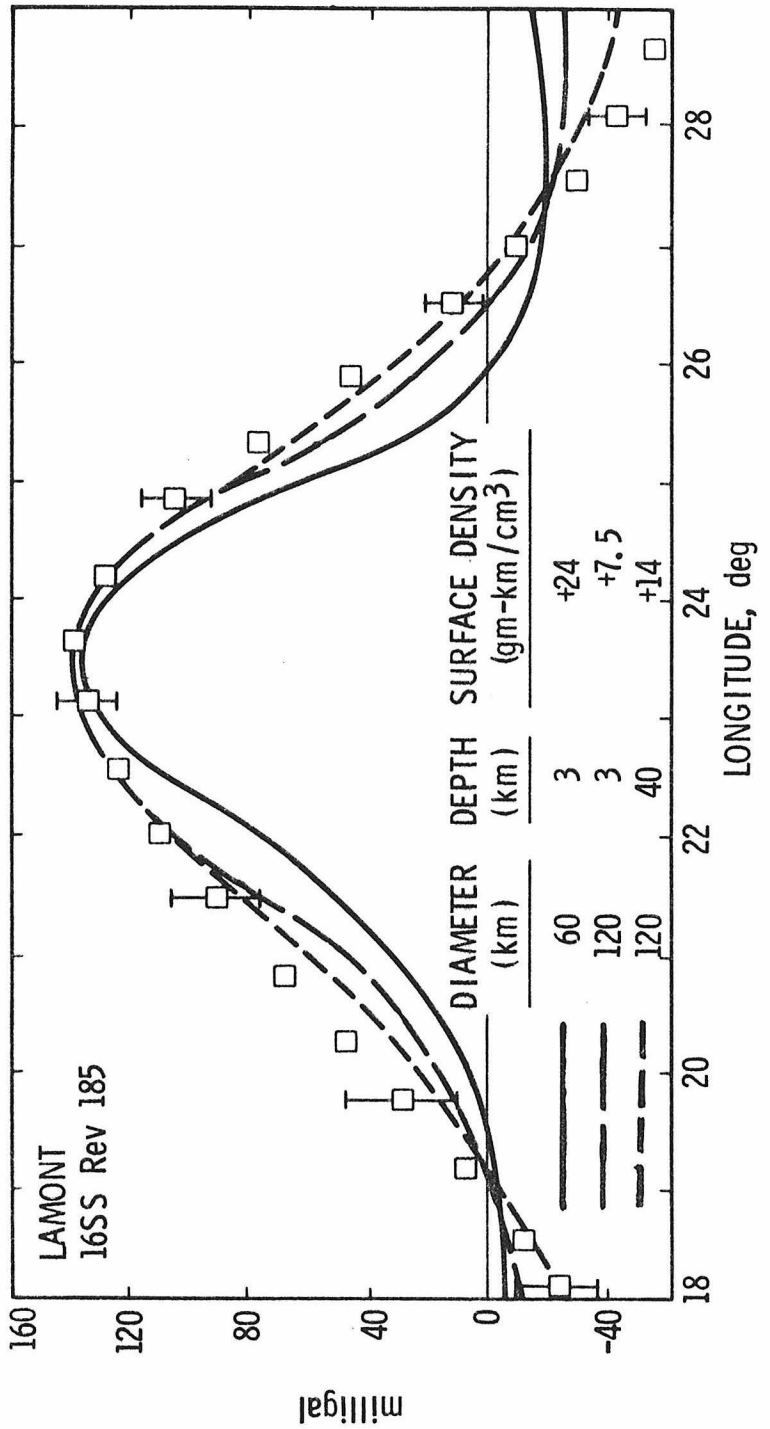
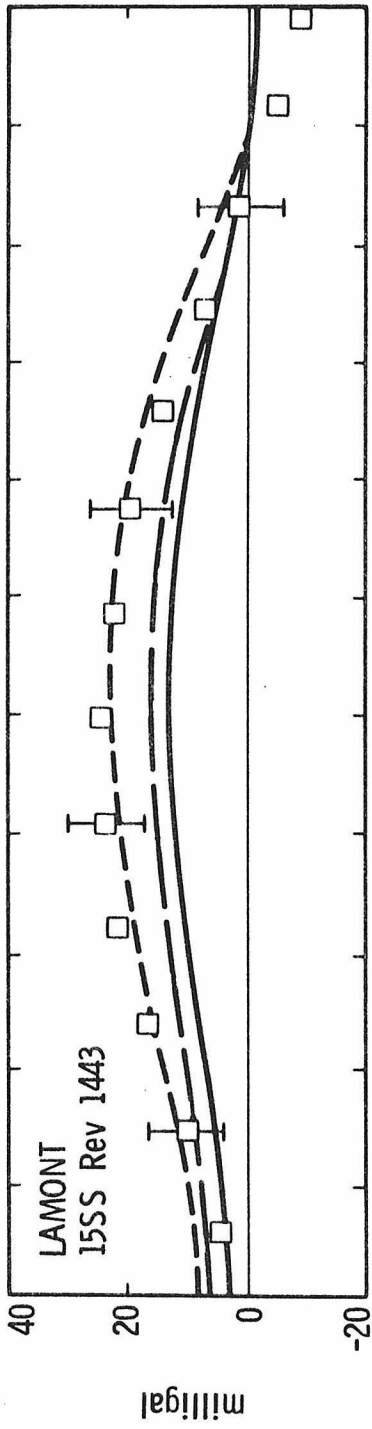
The low altitude gravity data provided by the Apollo 16 subsatellite, revealed a positive free-air gravity anomaly centered at Lamont (Sjogren et al., 1974a) slightly elongated to the north and to the southwest of this feature. This gravity anomaly was also resolved by the high altitude Apollo 15 subsatellite (Sjogren et al., 1974a). The Bouguer gravity for both high and low spacecraft altitude orbits were determined by the procedure described in Chapter III and two representative profiles are shown in the Appendix. The topographic contribution to the local lunar gravity field, primarily arising from the north-south regional trough, assuming a density of  $3.0 \text{ gm/cm}^3$ , adds a maximum of forty-five milligals to the low orbits and ten milligals to the high orbits.

The results of several model calculations for both a high and a low orbit are compared with their respective Bouguer profiles in Figure 32. The uncertainty in deriving these profiles, which is shown for every third point, has been discussed in Chapter III. All model components were assumed to be circular disks symmetrically placed with respect to the center of Lamont. As in previous calculations, the diameter and the depth of burial of a proposed model is prescribed and the surface density for this geometry is determined from the magnitude of the Bouguer anomaly. The thickness is then estimated by dividing the surface density by an assumed value for the density contrast.

The first two model calculations shown in Figure 32 are surface disks of different diameters. The first has a diameter equal to the diameter of the inner ring of wrinkle ridges at Lamont. For the low orbit, it is evident in Figure 32 that this produces a signature too narrow to match the Bouguer profile, so that, either a broader surface component or a deeper depth of burial is required. A broader surface model, such as the second model shown which extends to the less well-defined outer ridge structure of Lamont, is better able to reproduce the Bouguer profiles within the estimated uncertainties. A deeper model positioned anywhere within the expected thickness of the lunar crust, that is, within roughly fifty kilometers of the surface, still requires the anomalous mass to extend

Figure 32. Comparison of model calculations with the Bouguer profiles (squares) across Lamont. The upper profile is for a high orbit (120 km altitude) and the bottom for a low orbit (20 km altitude). Note the vertical scale difference in upper and lower diagrams. Error bars were determined by the procedure described in Chapter III and are shown for only every third data point.





well beyond the inner wrinkle ridge ring and approximately to the diameter of the less well-defined outer ring. A representative deep model is shown in Figure 32 by the third calculation. These deeper models fit the nominal values of the Bouguer profiles better than surface models, though, within the uncertainties, it is not possible to convincingly constrain the depth of burial.

The corresponding surface density of each model calculation shown in Figure 32 is listed in this figure. As previously mentioned, to determine the approximate thickness of these models, a value for the density contrast is assumed and divided into the computed surface density. For an assumed value of  $+0.6 \text{ gm/cm}^3$  for the density contrast between mare material and normal lunar crust, the model calculations shown in Figure 32 give possible thicknesses for the high density component ranging from roughly ten to twenty kilometers. Other possible high density components within the lunar crust would give similar values for the density contrast (see Chapter VII). These thickness estimates may be slightly reduced by increasing the diameter of these models, however, the width of the low orbit gravity signature constrains this diameter to be less than 150 kilometers. At this upper limit the corresponding surface densities, and, hence, thicknesses, determined for the second and third models shown in Figure 32 may be reduced by up to 40%, so that, at a minimum the thickness of the high density component must be at least eight to ten kilometers; a value probably still too large to be totally due to an accumulation of surface mare material, so that, a significant amount of this anomaly must also be due to high density material at depth.

A second important source of information regarding the subsurface structure and the history of Lamont is the magnetic measurements taken from orbit by the magnetometers onboard the Apollo 15 subsatellite at an altitude of approximately 100 kilometers. A map of the lunar remanent magnetic field across Lamont (Figure 33) (see also Proceedings of the Eighth Lunar Science Conference, frontispiece) derived from these measurements shows a pronounced high associated with the scalar magnitude of the magnetic field. The corresponding map of the radial component of this field shows a lack of a magnetic anomaly, in other words, the magnetic field lines associated with the Lamont anomaly are horizontal. This is further borne out by the lack of an anomaly associated with the surface radial component of the remanent magnetic field measured by the electron reflectivity experiment also onboard the Apollo 15 subsatellite.

#### Discussion

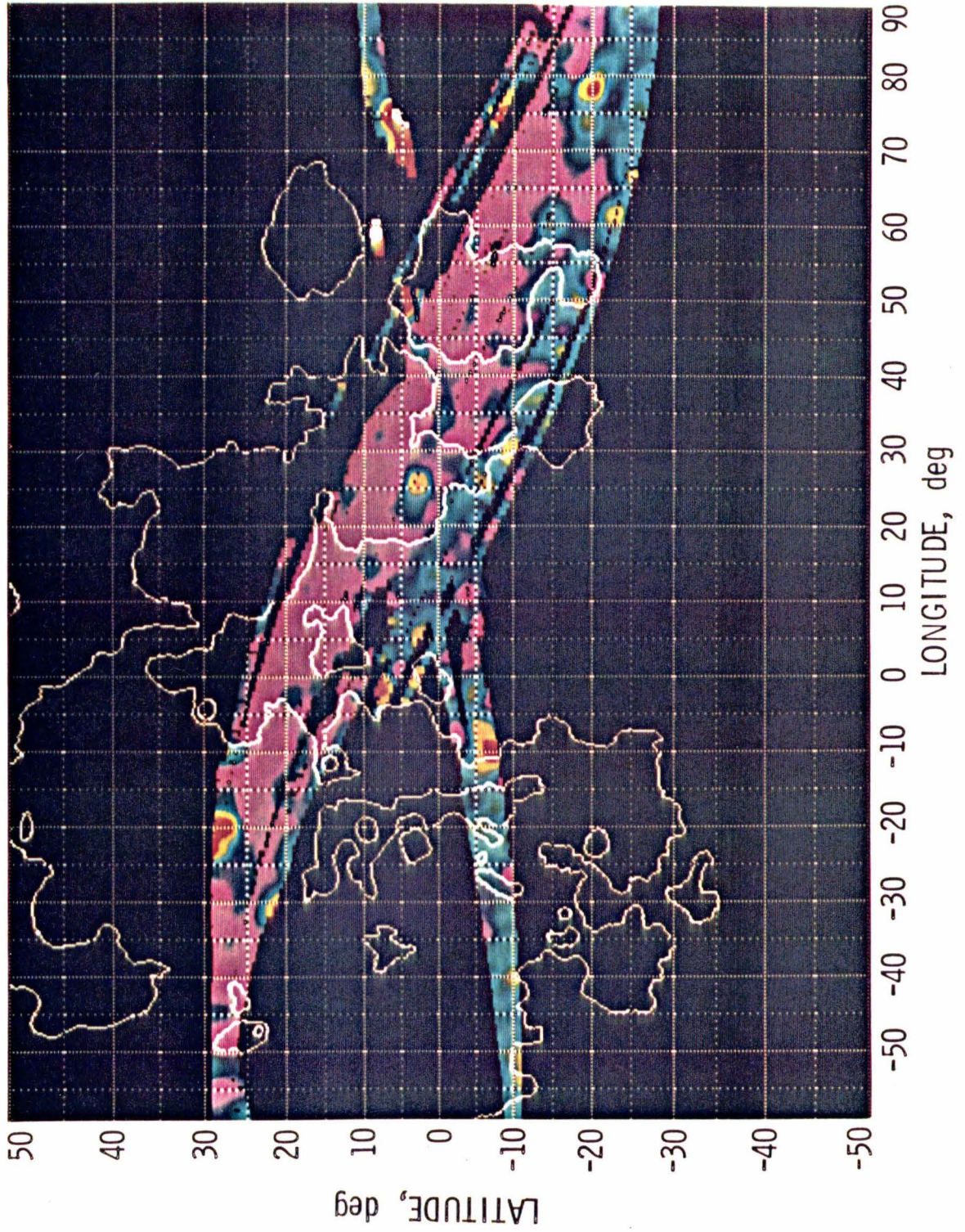
Since the Lamont structure has a positive free-air gravity anomaly and is a topographic low region, it is, by definition, a lunar mascon, though it may not necessarily have the same origin as other lunar mascon features such as Imbrium, Serenitatis, Nectaris, and Crisium Basins.

A large impact event resulting in the formation of a concentric ring structure is generally accepted as the origin of these basins and the later filling of the basin, usually by volcanic material, is a prerequisite for producing the mascon anomaly (see Chapter VII).

A similar origin for the Lamont structure has been suggested by Scott (1974) who interprets most of western Tranquillitatis as an old impact basin with an original outer diameter of 370 kilometers and suggests that the circular mare ridge pattern is the expression of a buried inner ring structure. These suggested dimensions for the ring structures are similar to the present dimensions of Grimaldi which was discussed in the previous chapter. In the case of Grimaldi, that feature is certainly of impact origin, is partly filled by mare material, and is a mascon anomaly. Furthermore, the size of the mass anomaly associated with Lamont is also similar to the size of the major positive component to the mass anomaly associated with Grimaldi.

The above observations support an impact origin for Lamont similar to the event which produced Grimaldi, however, the uncertain identification of the outer ring structure, the predominantly north-south structural elements, and the presence of the magnetic anomaly suggest that the Lamont region may have had a significantly different, or more radical history than most lunar basins. Alternatively, the major geologic events of this region may be structurally controlled by the intersection of separate regional fracture systems produced by several impacts, and the circular structure of Lamont may not be of an impact origin but of an igneous intrusive nature. These alternatives cannot be conclusively decided upon here, however, the

Figure 33. A portion of the map of the lunar remanent magnetic field acquired by magnetometers aboard the Apollo 15 and 16 subsatellites (see Proceedings of the Eighth Lunar Science Conference, frontispiece). The scalar magnitude of the field is represented by colors ranging from violet (0.16 gammas) to red (0.46 gammas).





interpretation of the later history of the Lamont structure is not the unique result of either origin. Most of the remainder of this discussion will principally focus on the intrusive origin to point out that this origin is consistent with all observations and leads to several interesting consequences regarding the role of igneous activity in lunar crustal history and the interpretation of many other positive gravity anomalies which lie within the lunar mare region and are not clearly associated with any well-defined surface feature.

Further indication that the history of the Lamont structure does not follow the post-impact history of other lunar basins is the claim that the magnetic anomaly associated with Lamont is probably not of impact origin. As discussed in Chapter II, magnetic anomalies are absent in structurally simple impact features such as Meteor Crater. Larger, structurally more complex and centrally uplifted impact features may have magnetic anomalies associated with their interiors believed to arise from magnetized high temperature fall-back debris, as at Ries Basin (Pohl et al., 1977), or highly shocked and thermally affected breccia deeper in the crater structure, as at Gosses Bluff (Milton et al., 1972), or possibly from impact-generated magnetization, as at the Manicouagan structure (Coles and Clark, 1978). However, it is uncertain whether the same mechanism could account for all of the geologic evidence pertaining to the location and



nature of magnetic anomalies associated with these terrestrial impact structures and whether it is applicable to Lamont.

On the Moon, there is a noticeable lack of magnetic anomalies associated with the interior of impact features. In view of this lack of correlation and the uncertain relationship of magnetic anomalies with terrestrial impact features, an alternative explanation for the magnetic high, and also for the gravity high associated with Lamont is sought.

On the Earth, both magnetic and gravity highs are associated with basic intrusive regions; most notable are the anomalies associated with volcanic centers along the Hawaiian ridge (Malahoff and Woollard, 1966). Supportive seismic evidence indicates that these magnetic and gravity anomalies are related to deep-seated intrusive material and not to the crustal rock or to the material comprising the major volume of the volcanic constructs along the Hawaiian ridge. Quantitative analysis of these measurements indicate that these intrusive rocks reach within two to six kilometers of the summit of the volcanoes.

For Lamont, seismic data are of course lacking, but the occurrence of the magnetic and gravity highs are suggestive of an intrusive origin, similar to the intrusive activity at centers along the Hawaiian ridge, for the anomalies associated with Lamont and, as will be described, for the circular structural pattern.

A proposed geologic history for Lamont and western Tranquillitatis is shown in Figure 34. In this figure, the major mass anomaly has been chosen to be shown as a single localized basaltic mass intruding into a less dense lunar anorthositic crust. Instead of a single plug of material, a plexus of dikes and sills may be more realistic for the intrusive body. The presence of the magnetic anomaly at Lamont suggests that the timing of the major intrusive event (Figure 34a) preceded the surface emplacement of the mare basalts in western Tranquillitatis, which are possibly only slightly magnetized (Lin et al., 1977), that is, sometime before  $3.7$  to  $4.0 \times 10^9$  years ago. This is consistent with measurements of the paleointensity of the stable magnetic remanence in returned lunar samples which show a decrease in the intensity of the lunar magnetic field with a later time of formation (Stephenson et al., 1977). This intrusion may have been aided by the slight global extensional stress field at this time in lunar history suggested by thermal evolutionary models of the Moon (Solomon and Head, 1978).

This mass may have continued to intrude and be a major region of accumulation of magma prior to extrusion of material onto the surface (Figure 34b). The possible time interval for the major stage of extrusive activity, based on radiogenic ages of returned Apollo 11 basalts (Papanastassiou et al., 1977), was  $3.6$  to  $4.0 \times 10^9$  years. During and after this stage, there apparently was no

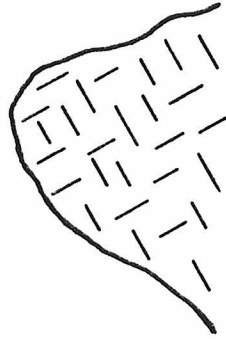
Figure 34. Schematic diagrams illustrating a proposed history of the Lamont and western Tranquillitatis region of the Moon.

INTRUSION (>4 x 10<sup>9</sup> YEARS)

B̄ FIELD

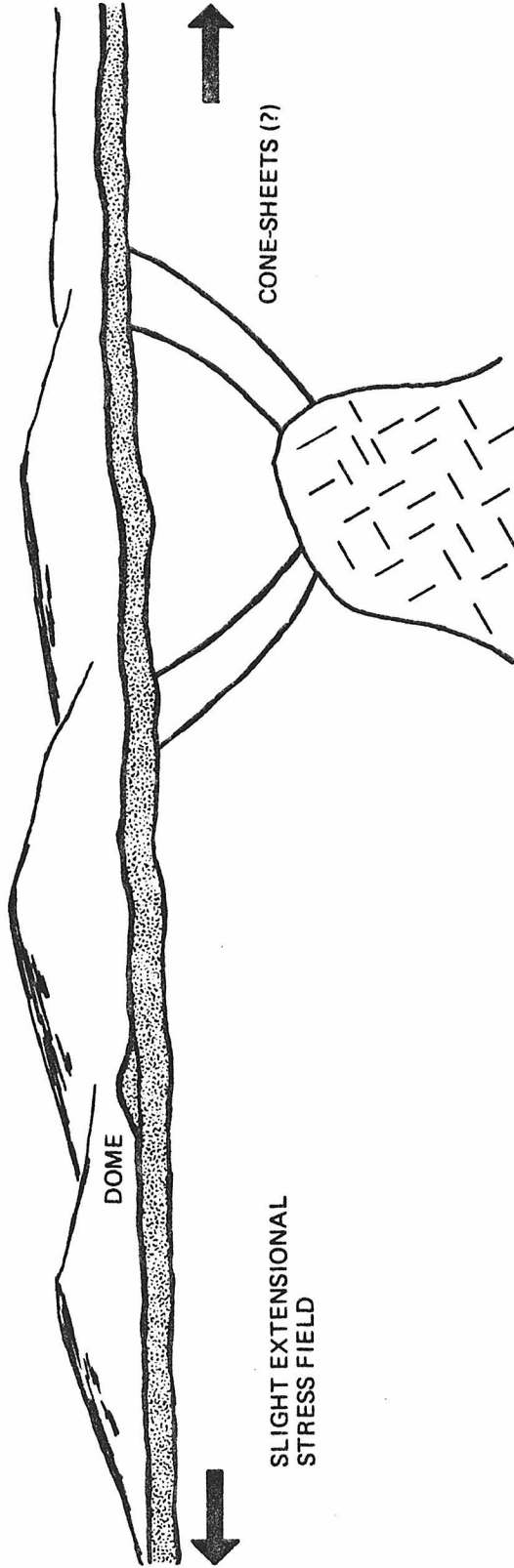


SLIGHT EXTENSIONAL  
STRESS FIELD



CONTINUED INTRUSION AND EMPLACEMENT OF MARE (3.6-4.0 x 10<sup>9</sup> YEARS)

NO APPRECIABLE  $\bar{B}$  FIELD



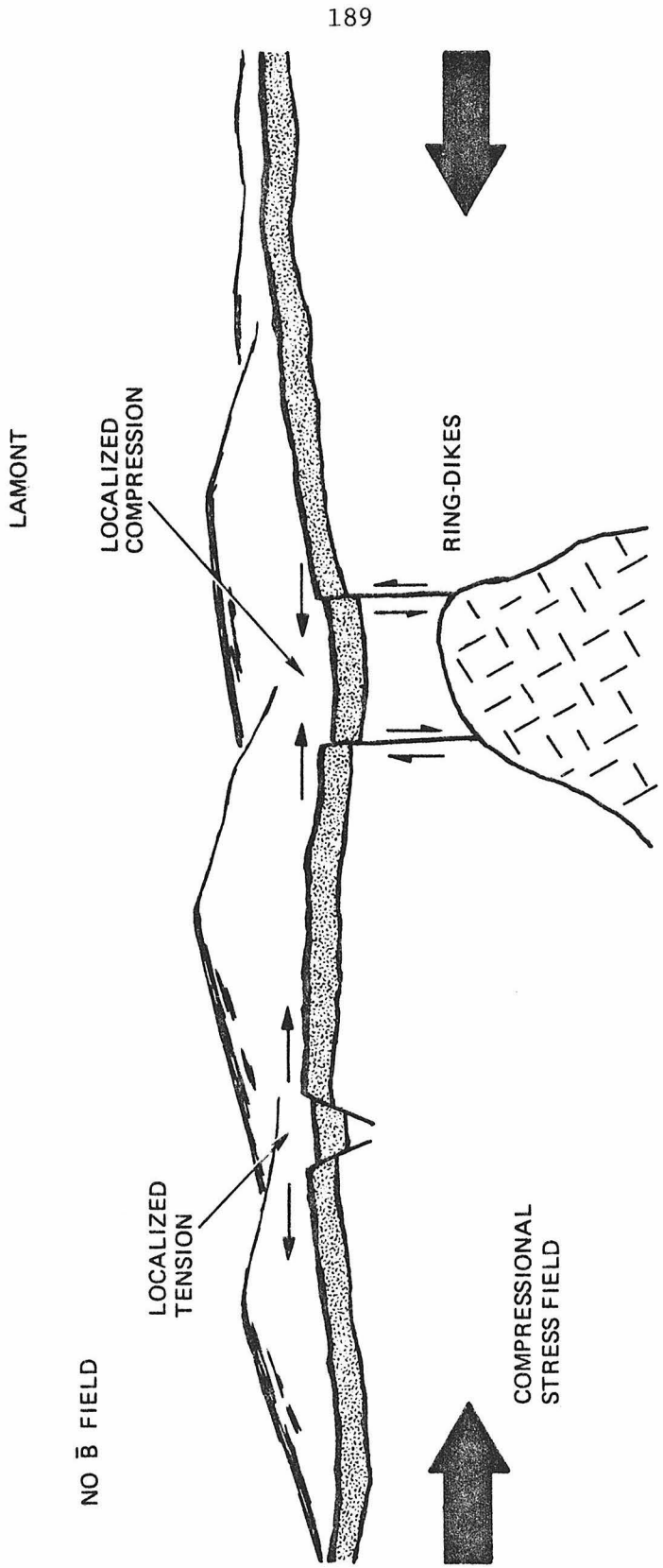
CONE-SHEETS (?)

188

DOME

SLIGHT EXTENSIONAL  
STRESS FIELD

MAGMA WITHDRAWAL; FAULTING AND BUCKLING ( $< 3.6 \times 10^9$  YEARS)



NO  $\bar{B}$  FIELD

LOCALIZED TENSION

LAMONT

LOCALIZED COMPRESSION

COMPRESSIONAL STRESS FIELD

RING-DIKES

appreciable lunar magnetic field recorded in the mare material. This continued intrusive activity may have been accompanied by the formation of concentric inclined dikes known as cone-sheets (Anderson, 1936) which served as conduits for the extrusion of magma onto the surface. The total volume of extrusion in western Tranquillitatis, assuming an average thickness of one kilometer, is  $200,000 \text{ km}^3$ , an amount comparable to the volume of the Columbia River Plateau basalts (Waters, 1962). If the mass anomaly at Lamont is totally due to intruded material and has a density contrast of  $+0.6 \text{ gm/cm}^3$  with the lunar crust, then the volume of intrusion was also roughly  $200,000 \text{ km}^3$ .

Possibly overlapping in time with the last major stages of intrusive and extrusive activity was the formation of the four major structural elements in western Tranquillitatis described earlier, that is, the circular ridge pattern and the north-south trending mare ridges, trough, and straight lunar rilles (Figure 34c). These features are consistent with a predominantly east-west compressional stress field resulting in the formation of the north-south structural elements by faulting and buckling of the lunar crust and a circular pattern centered over the localized intrusive body. This east-west compression created a minor buckling of the crust resulting in concentrated surface compression in the trough (mare ridges) and slight, localized, surface tension at a slight rise of

the crust to the west (straight lunar rilles). The circular pattern and topographic low centered at Lamont may be similar to terrestrial ring-dikes which are circular, almost vertical dikes which accompany the withdrawal of magmatic support (Anderson, 1936).

The origin of this east-west compressional stress field may be due either to contractional cooling or to tidal despinning of the Moon. Thermal history models of the Moon have shown that contractional cooling may globally produce up to 600 bars of compressive stress between  $3.6$  and  $2.4 \times 10^9$  years and in excess of 1000 bars over the whole of lunar history; only a fraction of this is necessary to initiate the observed faulting and buckling of the lunar crust in western Tranquillitatis.

The other alternative, tidal despinning, is also adequate to produce this deformation. To illustrate, the flattening,  $\epsilon$ , of a rotating fluid mass is given by the ratio of the centripetal to gravitational forces.

$$\epsilon = \pi \frac{\omega^2}{G\rho} \quad (29)$$

Here  $\omega$  is the rotational velocity,  $G$  is the gravitational constant, and  $\rho$  is the density. In order to locally generate as much as a few hundred bars of compressive stress, for a material with a rigidity of  $5 \times 10^{11}$  dynes/cm<sup>2</sup>, the required strain, or change in flattening, is  $2 \times 10^{-4}$ . For the Moon, this corresponds to a minimum initial rotational rate of roughly three to six days. The time scale for



this despinning, estimated from an expression given by Goldreich and Soter (1966, Equation 17) and assuming synchronous rotation, is  $\sim 10^9$  years, sufficiently long-term to be consistent with the post-mare occurrence of this deformation.

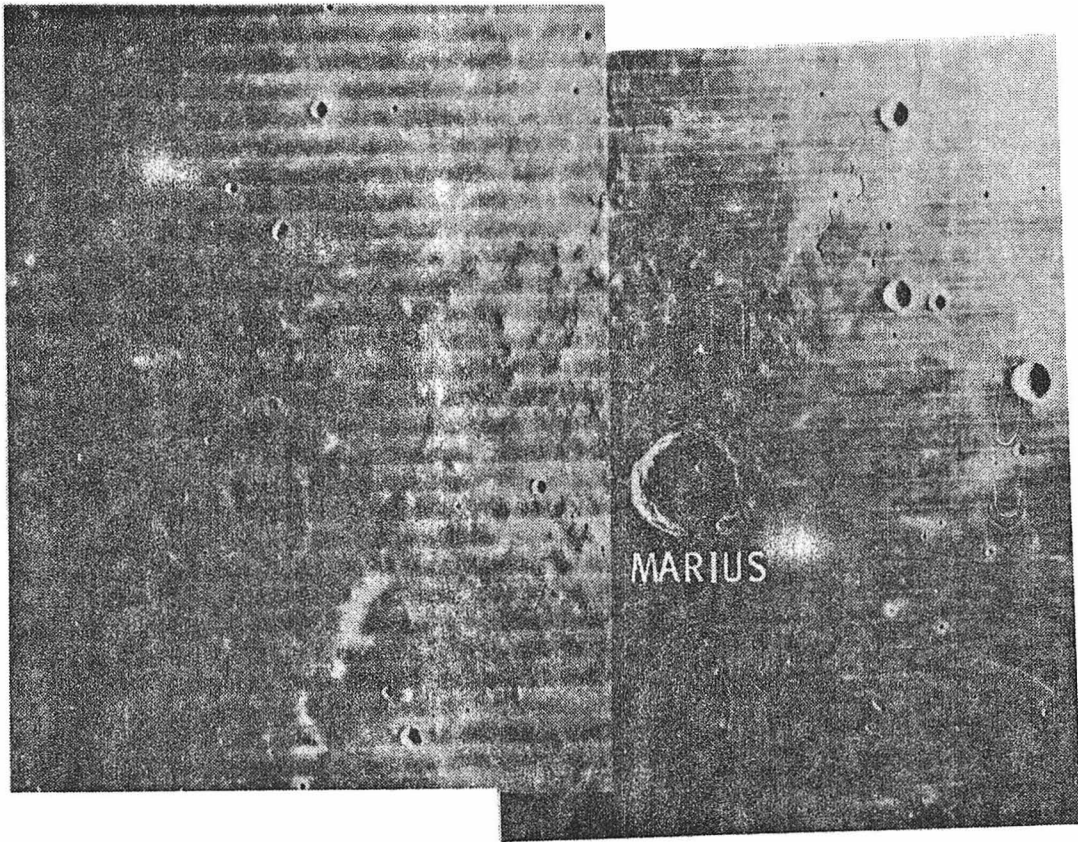
It is significant that Lamont is a very old mare region of the Moon and also exhibits gravity and magnetic anomalies and a unique post-mare structural history. Other regions, such as the irregular mare of Oceanus Procellarum, also have many small scale positive gravity anomalies, most notable is the anomaly southeast of Copernicus (Sjogren et al., 1974a) which is similar in magnitude and width to the Lamont anomaly, but lacking any surface expression. It is proposed here that many of these locations of positive gravity anomalies are also sites of early intrusive activity in the lunar crust which were completely covered by later extrusive activity. In western Tranquillitatis, continued volcanic flooding resulting in an accumulation of an additional five hundred meters of material would have completely buried the mare ridge structures at Lamont.

#### MARIUS HILLS

##### Description

Marius Hills is a southward dipping plateau lying in the irregular mare of Oceanus Procellarum covering an area of  $35,000 \text{ km}^2$  and rising to an average elevation of a few hundred meters above the surrounding mare plain (Figure 35). Well-developed scarps and

Figure 35. Lunar Orbiter photographs (IV-150-H2 and IV-157-H2) of Marius Hills. North is to the top of the page. Note the coalescing, rimless depressions to the north of the crater Marius (40 km diam) and the sinuous lunar rilles originating in the western portion of the plateau.



contacts with the surrounding mare of Oceanus Procellarum are lacking along most of the boundary of this plateau and the composition of this region, as determined from spectral reflectivity measurements (McCord et al., 1972), is similar to that of the surrounding mare. This region is named for its close proximity to the forty kilometer crater Marius which lies on the eastern border of the plateau and which is filled with Imbrian age mare material to a level six to eight hundred meters below the mare level immediately to the southeast.

Marius Hills is much younger than Lamont and represents a very late-stage occurrence of surface volcanism of the Moon. Stratigraphically, this plateau is Eratosthenian in age (McCauley, 1967) and, from an examination of the morphology of small craters, an absolute age of  $2.6 \pm 0.3 \times 10^9$  years (Boyce, 1976) has been placed on the mare material of this plateau.

The chief distinguishing characteristic of this region of the Moon are the many small cones and domes (~300) which populate the plateau varying in diameter from a few kilometers up to twenty-five kilometers and rising to a height above their bases of several hundred meters. A morphologic classification of these domes has been given by McCauley (1967) and Whitford-Stark and Head (1977). As was mentioned in the discussion of the dome structures in the Lamont region, the presence of these volcanic constructs suggest the occurrence of a style of lunar volcanism different from the emplacement of the vast mare plains.

Several sinuous rilles, interpreted as lava channels or collapsed lava tubes (Oberbeck et al., 1969), begin at irregular depressions within the plateau or just beyond the boundary and continue in a generally downslope direction, sometimes totally a few hundred kilometers in length, and gradually merge with the surrounding mare. In at least one case at Marius Hills, a rille originating on the plateau has its source at a cone (Greeley, 1971).

Two major mare wrinkle ridge systems, trending roughly north-south, transect Marius Hills. The eastern most system passes across the topographic high of the plateau just to the northwest of the crater Marius. Slightly to the east of this high region are located several coalescing, irregular, steep-sided depressions five kilometers in width. These features appear to be similar to terrestrial collapse caldera and are probably also the result of the near surface localized withdrawal of magmatic support (Williams, 1941).

#### Geophysical Data

The positive free-air gravity across Marius Hills is primarily due to the higher elevation of the plateau above the surrounding mare plain (see Appendix). Within the uncertainty of this analysis, there is a marginal detection of a positive Bouguer anomaly located approximately at  $-51^{\circ}$  longitude along the Apollo 15 CSM groundtrack (Muller et al., 1974). The latitudinal or lateral extent of this Bouguer anomaly is poorly constrained due to lack of sufficient low

altitude areal coverage of this region, however, the longitudinal position of this anomaly on the lunar surface approximately corresponds to the location of the topographic high of the plateau.

Assuming a disk-shaped geometry, the following two models adequately fit the nominal Bouguer profile.

	<u>Model A</u>	<u>Model B</u>
Diameter	60 km	60 km
Depth of Burial	4 km	35 km
Surface Density	+4.5 gm-km/cm <sup>3</sup>	+6.0 gm-km/cm <sup>3</sup>

As with the lunar craters, there is a trade off of model parameters such that the total mass excess remains roughly constant.

Unfortunately, there are no orbiting magnetometer measurements across Marius Hills, as there are for Lamont, to determine the scalar magnitude or the horizontal component of the remanent lunar magnetic field. The measurements of the electron reflectivity experiments show a lack of a radial component to the surface remanent magnetic field in this entire region of the Moon; the same result as for Lamont.

### Discussion

At Marius Hills, an impact origin for the possible positive Bouguer anomaly appears to be unlikely in view of the surface geology, though the location of this plateau region on the Moon and the localized positive Bouguer anomaly, interpreted here as intrusive in origin, within the plateau may have been controlled by fractures

produced by impact events early in lunar history. It is noteworthy, in view of the morphologic differences, that the nominal value for the Bouguer anomaly is much smaller at Marius Hills than at Lamont and that it is apparently isolated from the major region of the plateau.

The youthful appearance of Marius Hills indicates that this volcanism was a very late-stage event in lunar history and the lack or marginal detection of a positive Bouguer anomaly further suggests that, in contrast to Lamont, only relatively minor intrusive activity may have accompanied this late-stage lunar volcanism and that such activity was not responsible for the formation of the entire plateau.

## HISTORY OF THE LUNAR CRUST

A chief aim of lunar science has been to study many different aspects of the Moon in an attempt to describe the history and evolution of this body. It is understood that the present lunar data are incomplete and that many major events in lunar history are not adequately represented or have not yet been correctly perceived. This incompleteness does make it difficult to separate generalities in the evolution of the Moon from isolated unique events and, hence, does allow many different scenarios to be constructed from the same set of observations. However, by the introduction of new data and new ideas it is possible to better constrain and characterize some of the proposed alternatives and from this gain a better understanding of lunar history.

Initially, Earth-based observations of the Moon were the sole basis for lunar studies, but with the advent of practical rocketry it was then possible to send instruments to the Moon to scrutinize and probe the lunar surface at close range. These lunar missions culminated in several manned landings which not only returned samples of the lunar surface for detailed examination in terrestrial laboratories but also returned a wealth of information collected on the surface and from lunar orbit. Of particular concern in the present work has been an analysis of the gravity anomalies associated with individual lunar features, mostly impact craters, derived from the



Doppler radio tracking of low orbiting lunar spacecraft. It is the purpose of this last chapter to expand on several points made in the earlier chapters and to place this work in context with other lunar research.

#### Lunar Cratering and Igneous Activity

The present surface of the Moon is readily distinguishable into a highly cratered, rugged highland region and a relatively smoother and darker mare region which covers less than 20% of the lunar surface and which consists mainly of the superposition of many basaltic lava flows. The lunar highlands, or terra, certainly predate and presumably underlie all of the lunar mare and represent the bulk composition of the lunar crust. Chemical constraints provided by the returned lunar samples indicate that early in lunar history the Moon differentiated into a feldspathic crust and a more mafic mantle with the lunar mare representing a much later differentiate of this mantle material (Ringwood and Essene, 1970).

From seismic data, the thickness of the lunar crust in eastern Oceanus Procellarum is 60 kilometers (Toksöz et al., 1974) with a slightly larger (70-80 km) average global thickness determined from the lunar center-of-mass to center-of-figure offset (Kaula et al., 1974). As commented in Chapter IV, the impacts which formed the large lunar craters, such as Copernicus, were capable of brecciating and probably also excavating at least small amounts of material from depths as great as one-fourth the present crater diameter. Extending

this result to the very large impacts which formed the multiringed basins, these events were certainly capable of penetrating the lunar crust resulting in excavation and deposition of a small amount of the lunar mantle material onto the surface, possibly represented by the dunite fragments returned from the Apollo 17 landing site (Dymek et al., 1975).

Due to the locations of the small number of lunar landings, the velocity structure of the lunar crust is only well-defined for eastern Oceanus Procellarum. In this region, the profile is characterized by a very low velocity surface layer several hundred meters to a kilometer thick overlying a region with a very steep velocity gradient continuing to a depth of about 25 kilometers at which point the velocity is possibly discontinuous and remains roughly constant to the bottom of the seismically defined crust (Toksöz et al., 1974). The thin low velocity surface layer, recognized at all Apollo lunar landing sites, is the result of the continuous bombardment of the lunar surface by many small impacts. The very steep velocity gradient in the upper lunar crust is due to the progressive closure of impact-induced microcracks under increasing hydrostatic pressure (Todd et al., 1973). Below this, the constant velocity profile of the lower crust indicates the absence of these features at these greater depths, though whether this absence is a result of the lack of sufficiently large impacts in this region which could penetrate to these depths or of the annealing of microcracks which at one time were present is uncertain (Simmons et al., 1973).

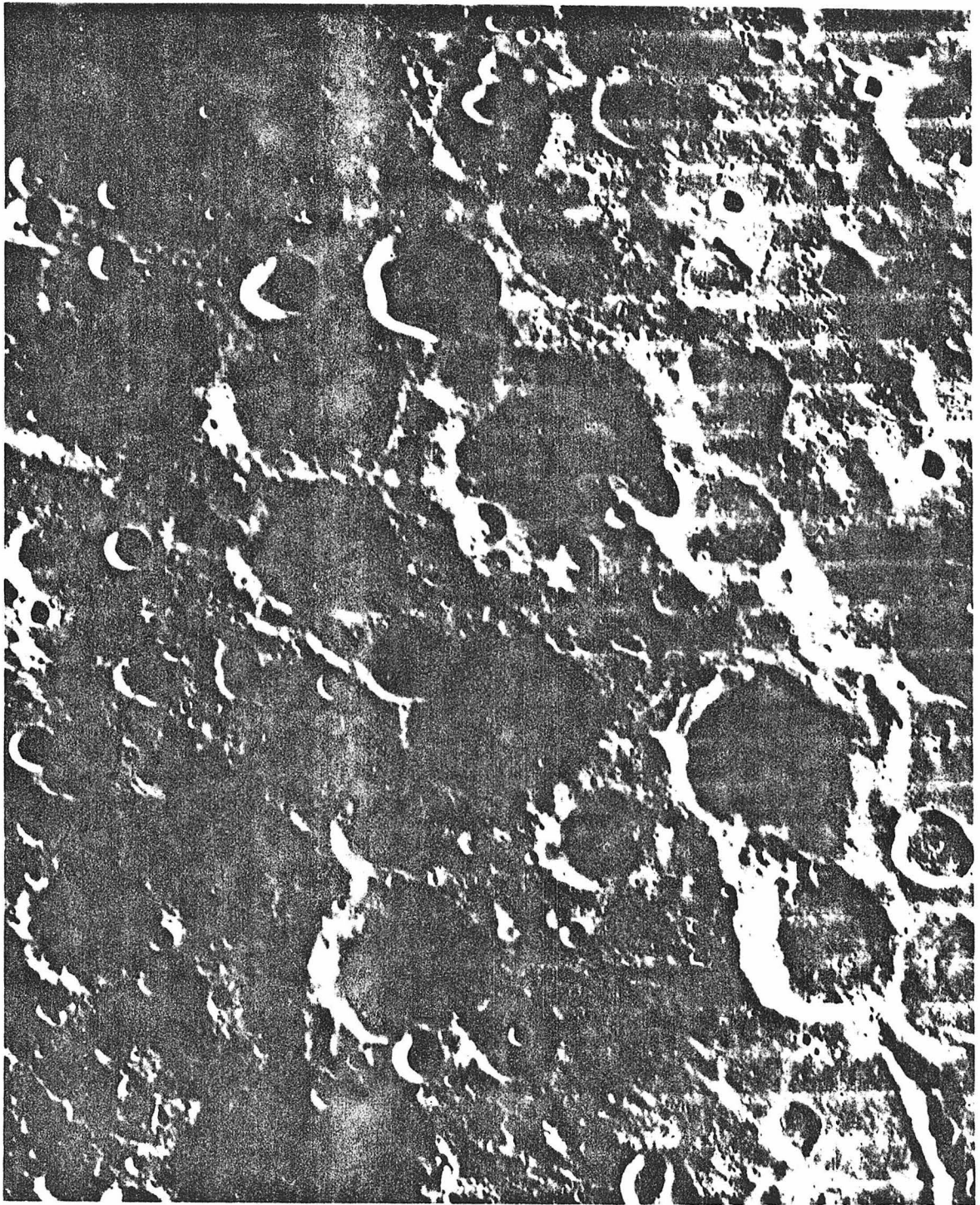
The difficulty in using this velocity profile to infer lunar impact history is knowing whether or not it is representative of the entire Moon, in particular, the position of the 25 kilometer discontinuity. If this is the average position of this discontinuity planetwide, then sometime after the consolidation of the lunar crust, the Moon must have been subjected to a sufficiently high cratering rate to globally fracture the crust to this depth. Monte Carlo cratering calculations performed by Hörz et al. (1976) indicate that to produce this average depth of fracturing over most of the lunar surface requires a cratering rate many times larger than the present density of large craters in the lunar highlands.

If the lunar crust was globally fractured and disrupted to a depth of several tens of kilometers, then it may be somewhat surprising that later cratering (e.g., Copernicus) was capable of generating sufficiently large density contrasts to result in detectable negative Bouguer gravity anomalies. This then suggests: 1) that the seismic profile of the lunar crust derived from the Apollo lunar missions is only representative of eastern Oceanus procellarum and, hence, the lunar crust was never globally fractured to these depths since the consolidation of the crust, or 2) that at some time in lunar history the upper crust has been recompactd, removing the porosity but not the microcrack structure, or 3) that the pore spaces produced by earlier impacts have been filled. Recall from the previous chapters

that only the young lunar craters have been shown to have negative Bouguer anomalies and that all old lunar craters, except Piccolomini, have zero anomalies. The process or processes responsible for the disappearance of the initially negative Bouguer anomalies associated with old lunar craters are possibly also responsible for the disappearance of the porosity which would have resulted from the early planetwide intense cratering which can possibly be inferred from the presence of the 25 kilometer discontinuity.

An igneous process has been suggested in Chapter V to account for this disappearance by an intrusive mechanism. Presumably, magma migrates through the crust along the many impact-produced fractures and removes most of the initial pore space created by the impacts. The occurrence on the surface of mare material in only the topographically lowest regions of the Moon suggests that the maximum height reached by lunar magma was hydrostatically controlled (Kaula et al., 1973). This hydrostatic control is strongly indicated in some heavily cratered regions, such as that shown in Figure 36, which were only partially flooded by lavas. However, elevation differences between lunar mare of different ages or compositions may be as great as one kilometer, such as between Grimaldi and Oceanus Procellarum (see Chapter VII), presumably due to a different magma reservoir

Figure 36. Lunar Orbiter photograph (IV-006-H3) of southern Mare Australe showing the partial flooding of a highly cratered region. Note that the mare lavas appear to rise to the same level in all large craters without transecting adjoining crater walls.



location or efficiency in transporting the magma. This restriction of surface volcanic activity to only the topographically lowest regions of the Moon is a direct result of the presence of a very thick lunar crust which is less dense than the liquid magma (Solomon, 1975). A possible difficulty with this igneous process, as pointed out in Chapter V, is the inability of magma to passively fill pore spaces over the necessary several tens of kilometers without undergoing significant cooling and a halt to migration.

A very different style of igneous intrusion from that described above is inferred to have occurred on the Moon from the existence of isolated gravity and magnetic anomalies. These are localized intrusions, so far only identified in the mare regions, revealed by the association of a gravity or a magnetic high with structural and morphologic features which identify a probably source area for the local mare material. The best example is the Lamont feature in western Tranquillitatis (Chapter VIII) which has both a gravity and a magnetic high associated with a unique set of north-south trending structural features. Other possible centers of intrusion, also discussed in Chapter VIII, are the source area for the last major lava flows in the Imbrium Basin near the crater Euler  $\beta$  (Schaber, 1973) which has a magnetic high and a region of the Marius Hills plateau which has a Bouguer gravity high. Other localized lunar gravity and magnetic highs, not obviously related to any surface feature, may

have a similar origin, but their expression has been greatly modified by either later impacts or extensive volcanic flooding.

An alternative process for the global recompaction of the lunar crust following an intensive heavy bombardment and also for the removal of the negative gravity anomalies initially associated with old unfilled lunar craters is the seismic shaking resulting from the formation of the last few multiringed basins. This process is attractive since it is potentially global in its effect, though as pointed out in Chapter V, the efficiency at this scale is unknown and there are potential stratigraphic difficulties.

#### Lunar Isostasy

The question of the state of lunar isostasy was also addressed in Chapter V. For small scale lunar features, such as those considered in this work, no indication of crustal movement in response to the differential stresses produced by surface topography was found; certainly no indication of a state close to total compensation at this scale. This is due to the presence of a sufficiently thick lunar lithosphere so that the spatial extent of the lunar features considered here are too small to result in long-term creep of the interior of the Moon. For the crater Pasteur, one of the largest features considered here (diameter 250 km; depth 3 km), the stress difference, assuming an elastic half-space, resulting from this crater is 75 bars (see McConnell, 1965) at a depth of 60 kilometers, that is at the depth of the crust-mantle interface, which is the



location of the major density contrast in the outer region of the Moon and potential origin for the Bouguer anomaly. This may be somewhat increased by considering a finite thickness for the lunar lithosphere. For a thickness of 200 kilometers, this stress at a depth of 60 kilometers will increase to 100 bars (see Melosh, 1976), a value close to the maximum stresses supported over long periods of time within the Earth (Lambeck, 1979) and probably too small to allow steady-state creep at this depth.

It is important to note that on a large scale, such as the lunar central nearside highlands, the Moon is compensated (Wood, 1970). This relief of differential interior stresses which resulted from surface loading apparently only occurred early in lunar history, since indications of compensation are only associated with very old lunar terrain. This older terrain was probably also controlled by large impacts whose structures were greatly modified by long-term interior movement because of the elevated thermal state earlier in lunar history (Solomon and Head, 1978) allowing for a more complete creep relief of stresses (Weertman, 1970). Later large impacts into the Moon failed to result in a similar degree of response of the interior, except when such response was directly impact related and resulted in the upward movement of the lunar mantle and the production of a concentric ring structure, such as Grimaldi (Chapter VII). Later, relatively minor adjustments have occurred at some very large lunar basins such as Humorum and Serenitatis as expressed on the surface by concentric rille structures (Baldwin, 1963).

## APPENDIX

## FREE-AIR AND BOUGUER GRAVITY PROFILES

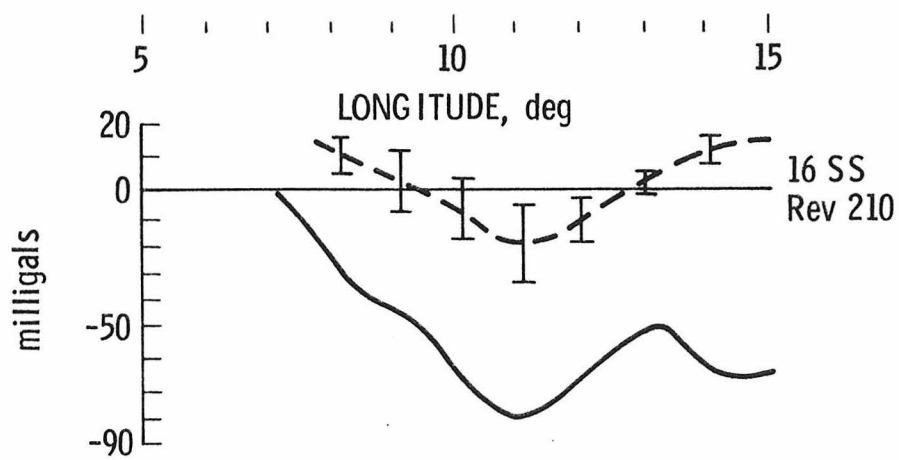
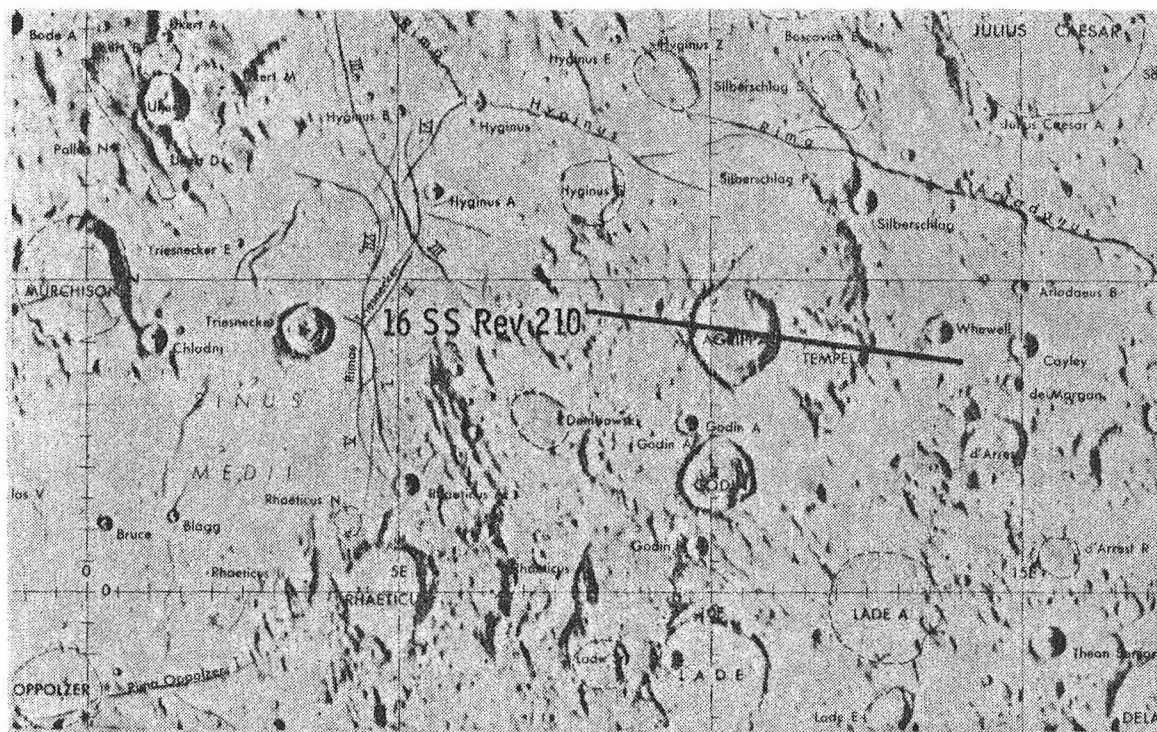
Representative free-air and Bouguer gravity profiles across each of the features considered in this work are given in this appendix along with a base map showing the location of the ground-track for each particular orbit. The spacecraft altitudes for each orbit, referenced to a 1738.0 kilometer radius sphere, were given in Table II (p. 5).

The features are presented alphabetically and an index is given on the next page. The free-air gravity is shown by a solid line and the Bouguer gravity by a dashed line, both as a function of longitude. The derivation of these Bouguer profiles was discussed in Chapter III. The error bars, shown at one degree averaged longitude increments along the Bouguer profiles, are the square root of the sum of the squares of the uncertainties in determining each profile contributed by uncertainties in the topography, by different assumed values for the density of the lunar crust, and by the intrinsic noise of the Doppler data.

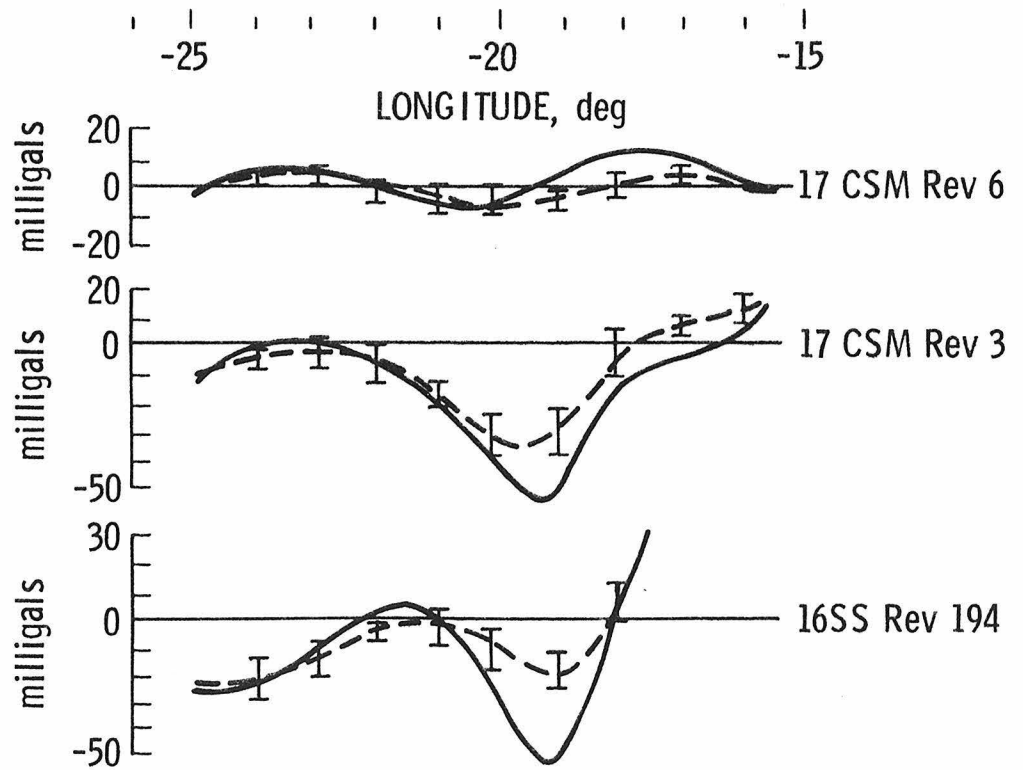
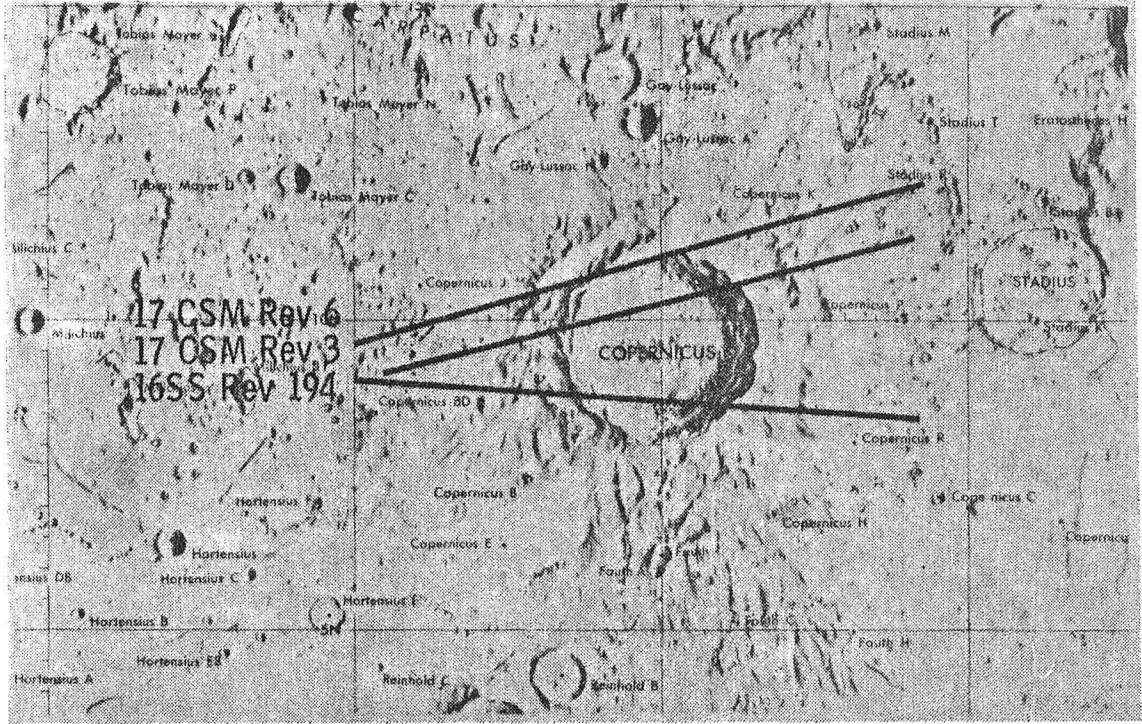
## INDEX FOR THE GRAVITY PROFILES SHOWN IN APPENDIX

<u>Feature Name</u>	<u>Page</u>
Agrippa	211
Copernicus	212
Eratosthenes	213
Grimaldi	214
Hecataeus	215
Herschel	216
Hipparchus	217
Humboldt	218
Kepler	219
Lamont	220
Langrenus	221
Macrobius	222
Marius Hills	223
Neper	224
Pasteur	225
Petavius	226
Piccolomini	227
Ptolemaeus	228
Sacrobosco	229
Snellius	230
Theophilus	231

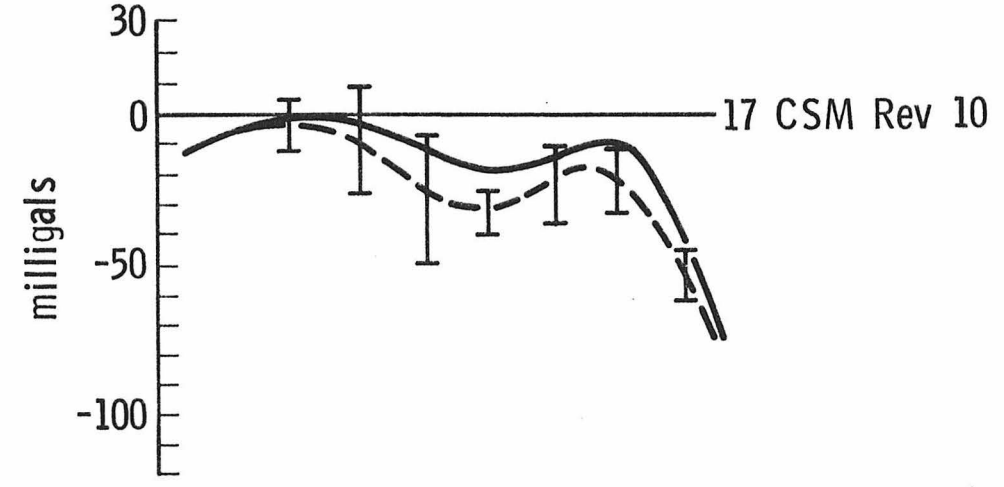
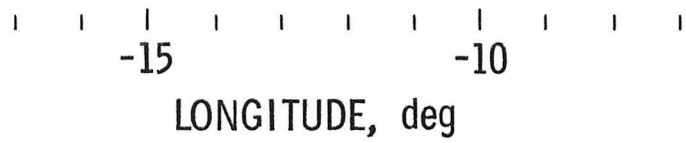
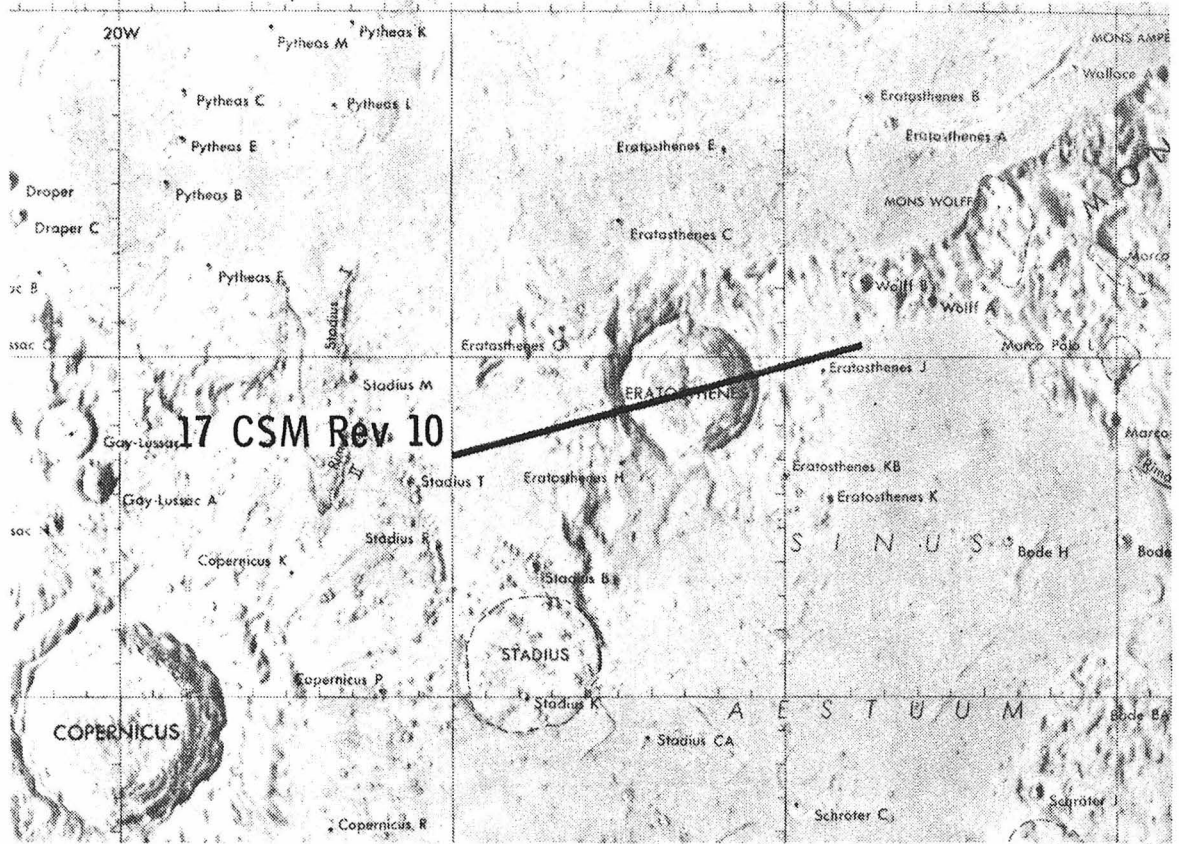
# AGRIPPA



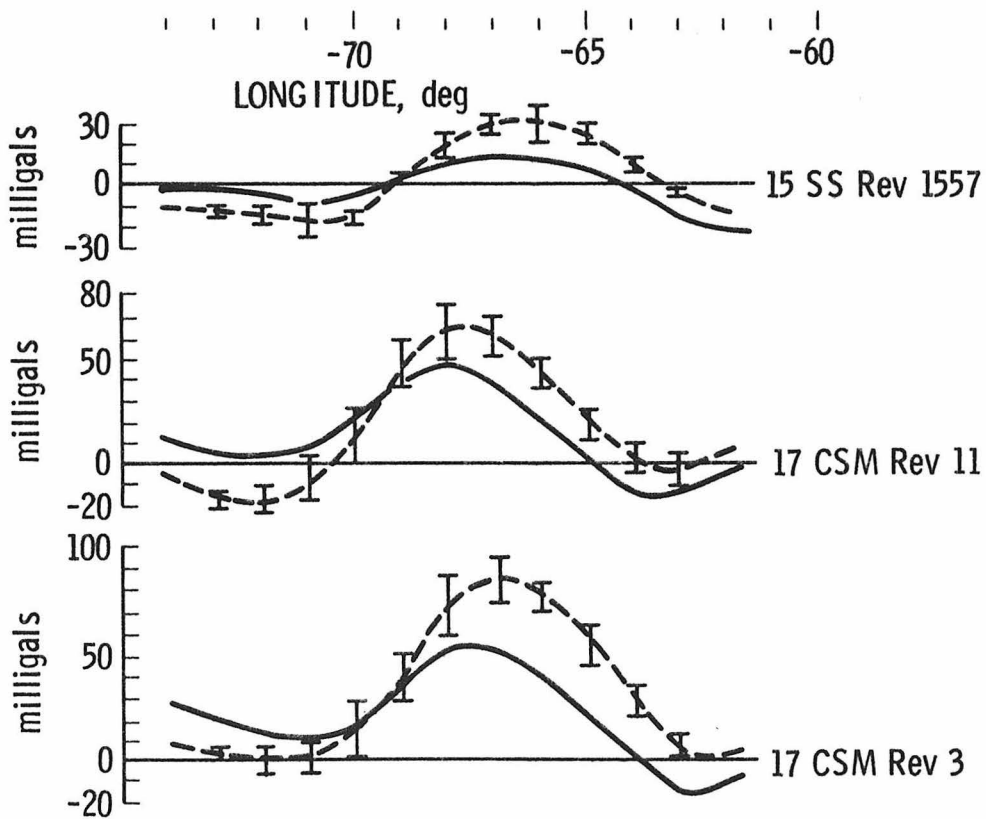
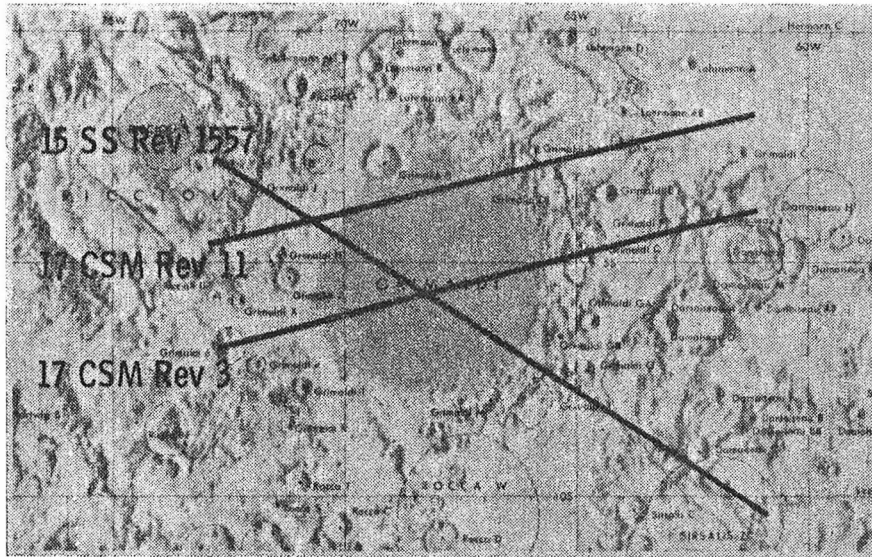
# COPERNICUS



# ERATOSTHENES



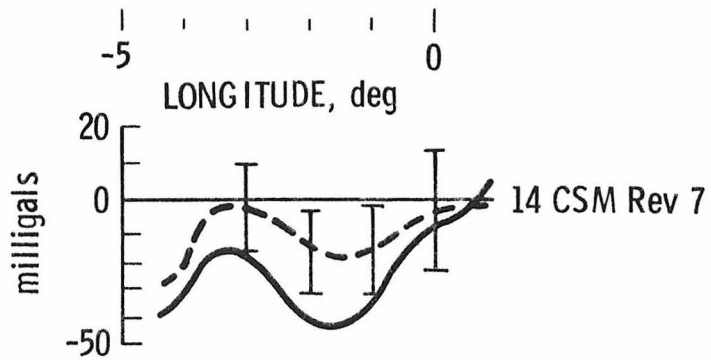
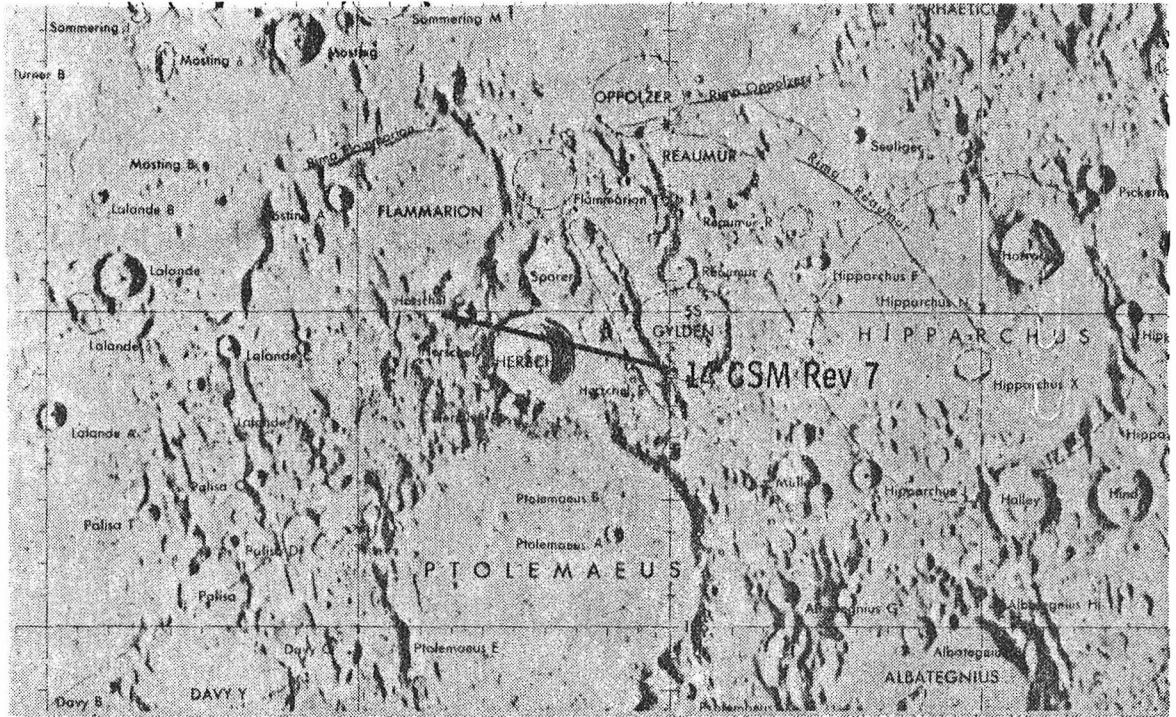
# GRIMALDI



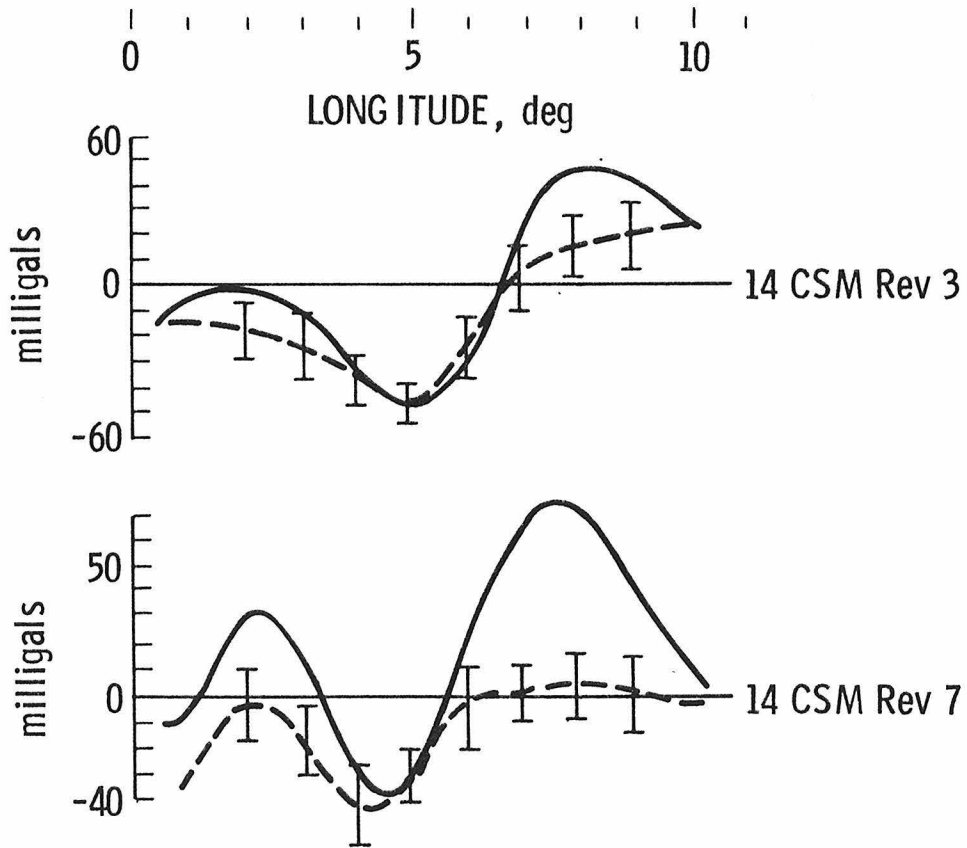
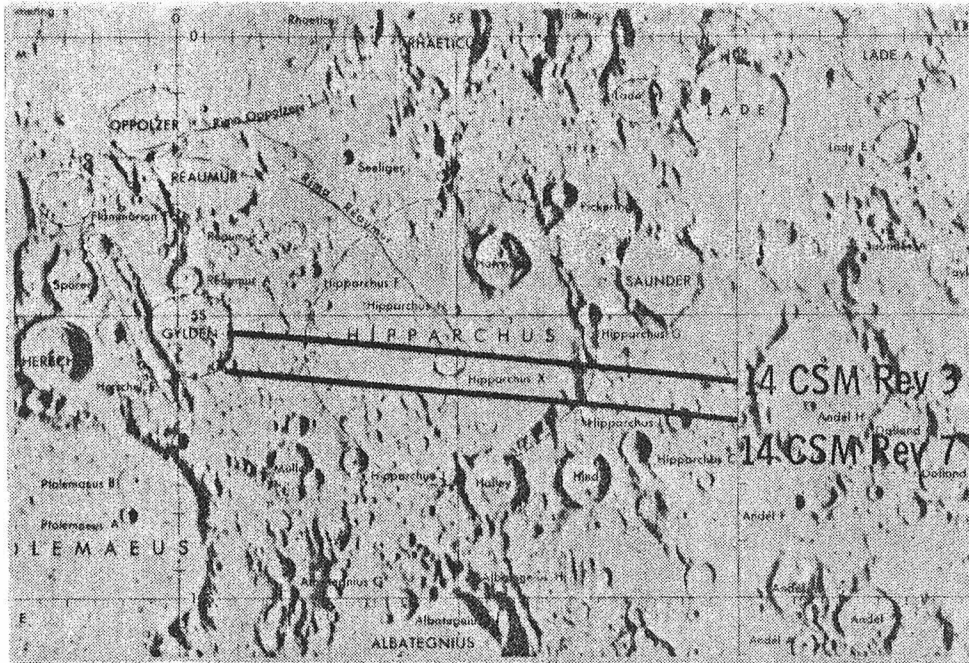




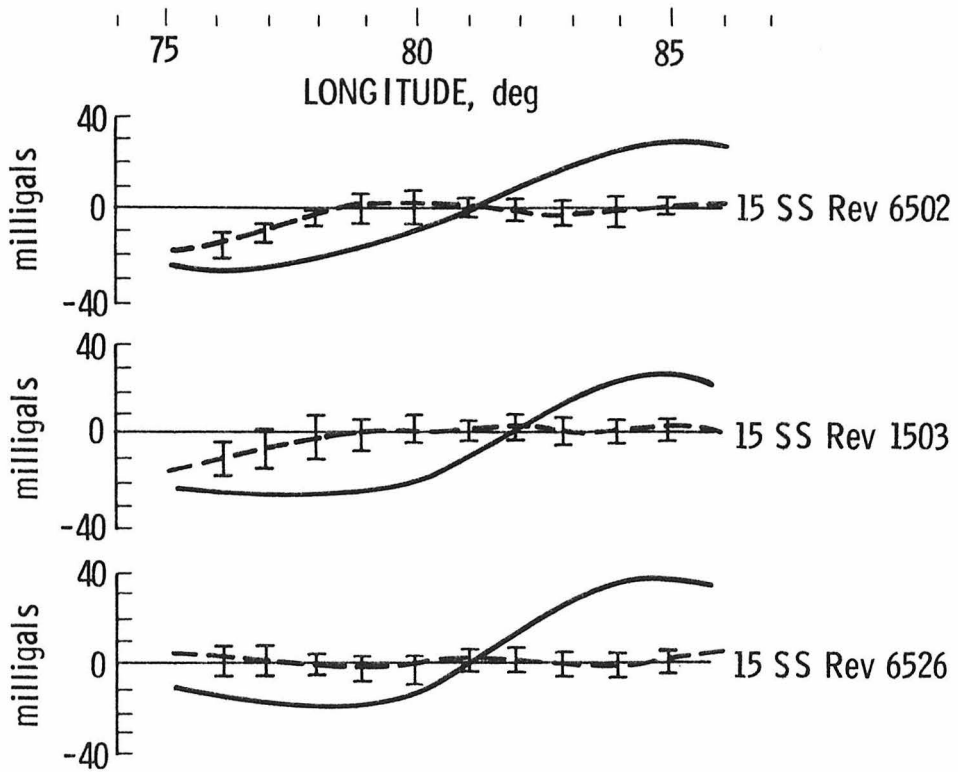
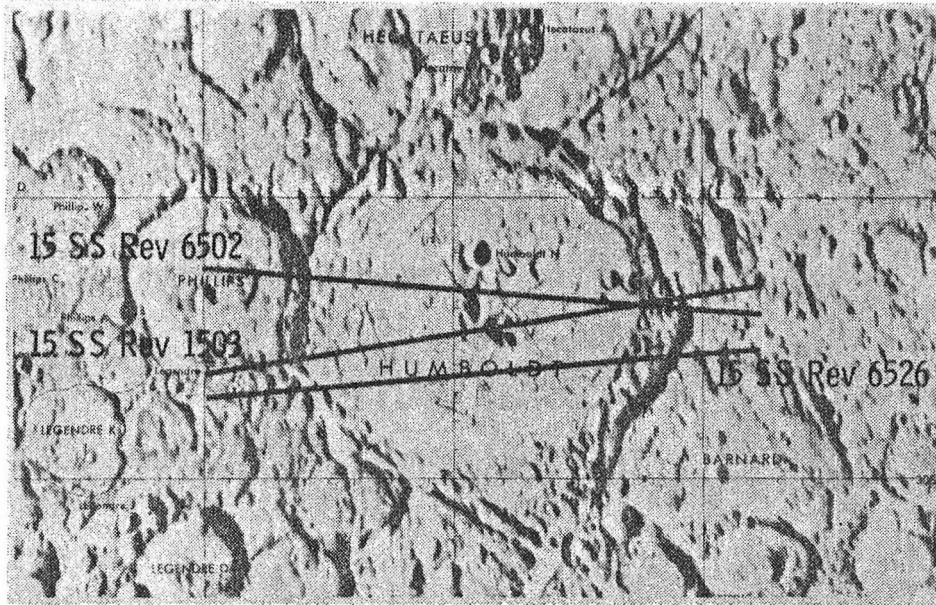
# HERSCHEL



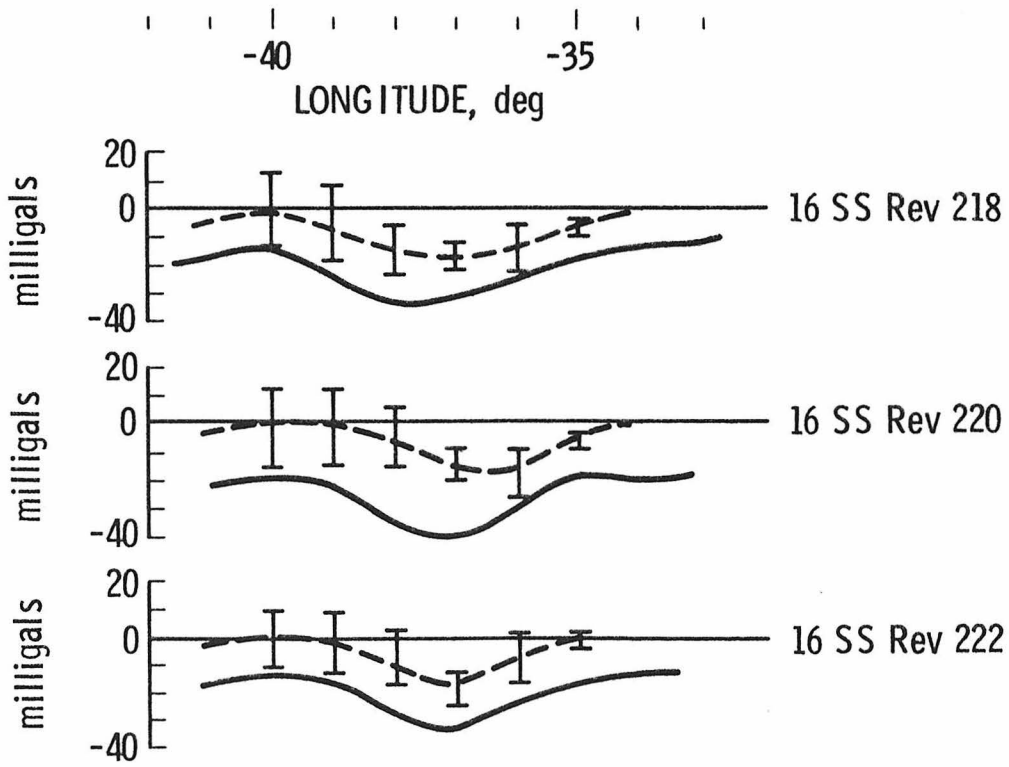
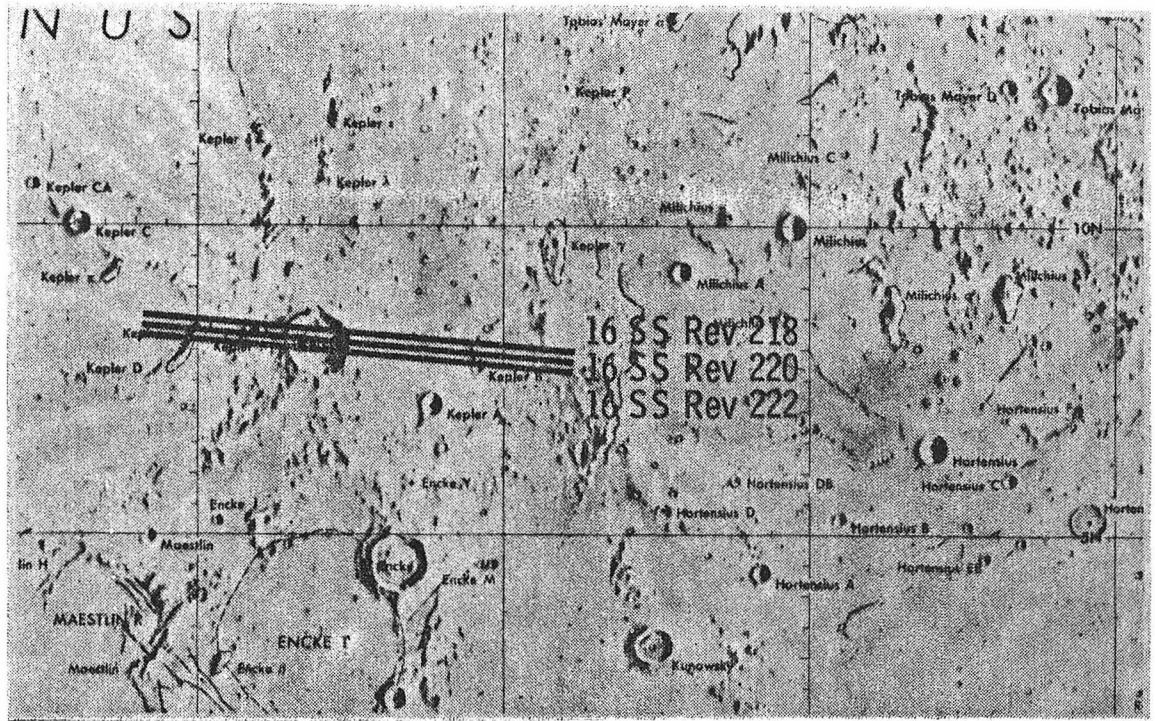
# HIPPARCHUS



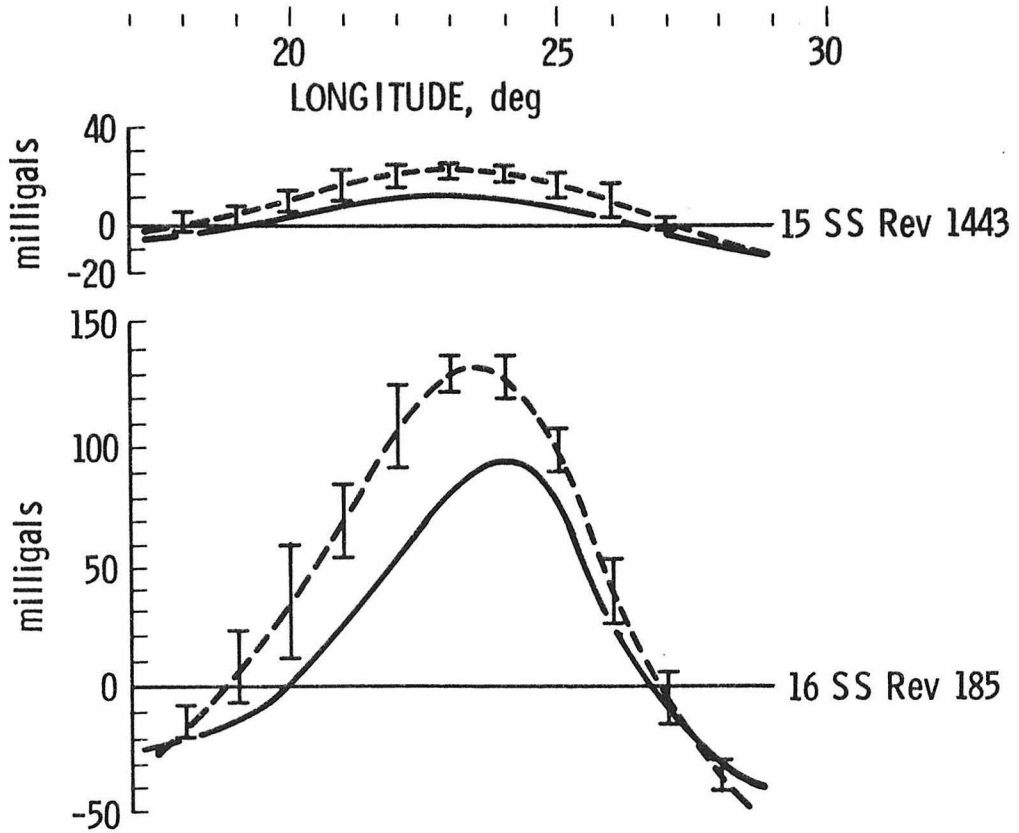
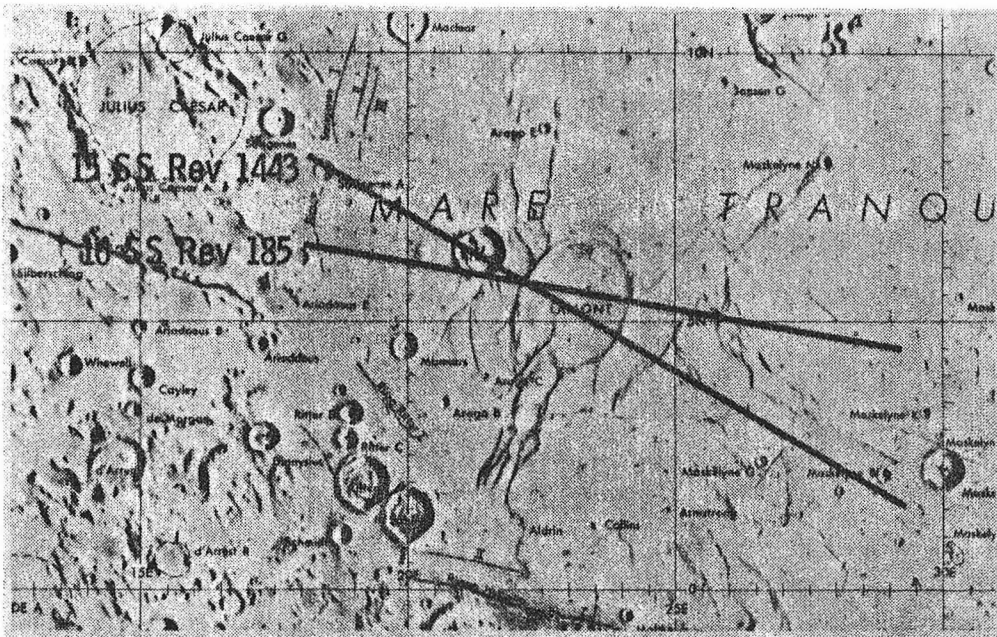
# HUMBOLDT



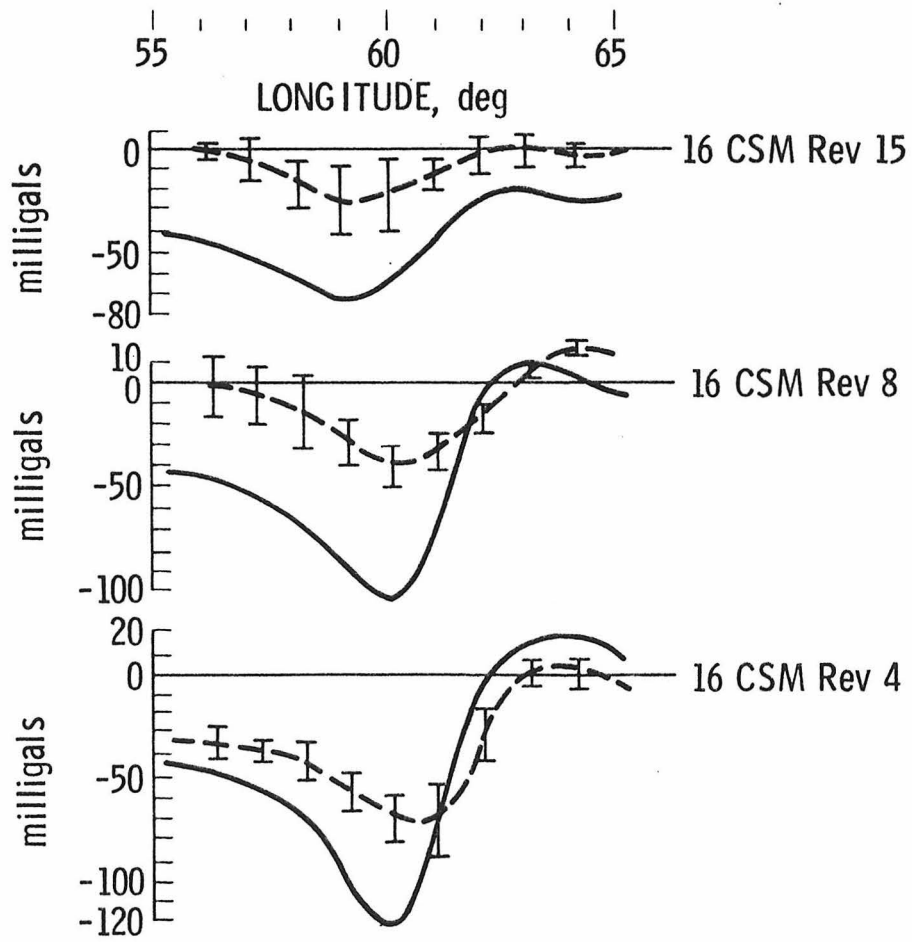
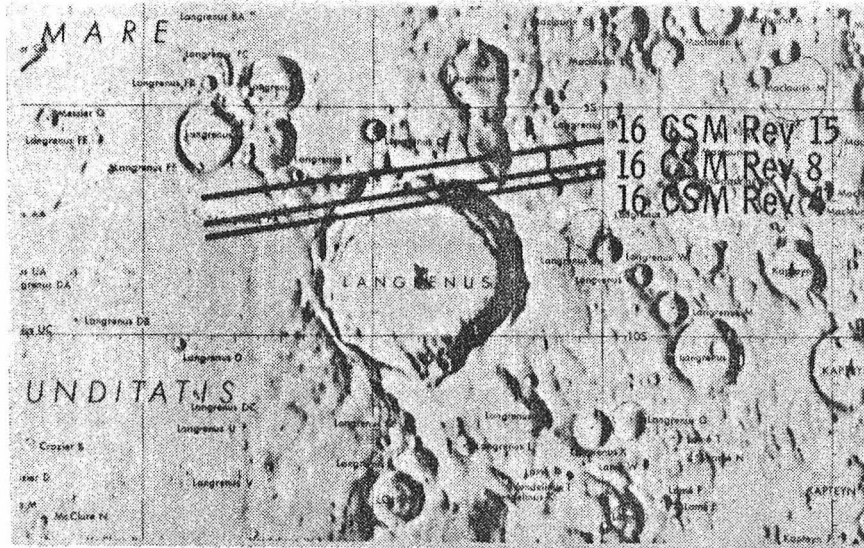
# KEPLER



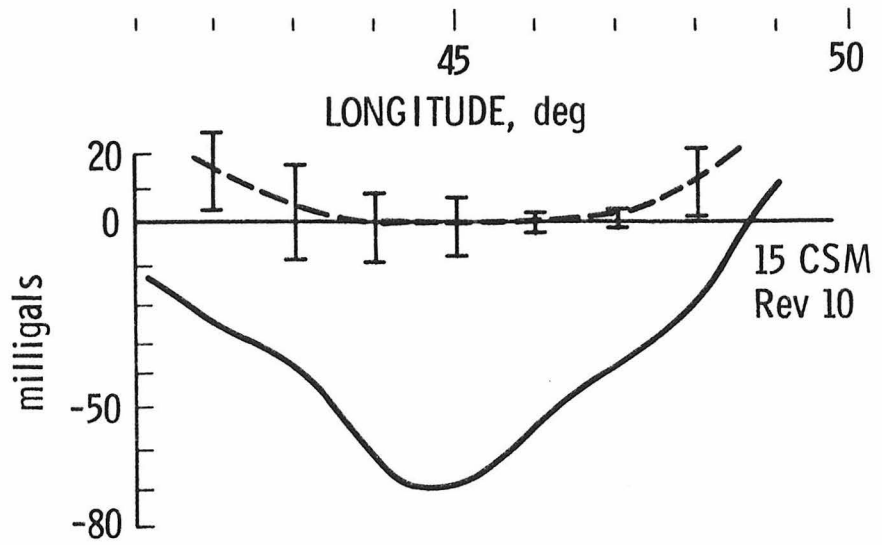
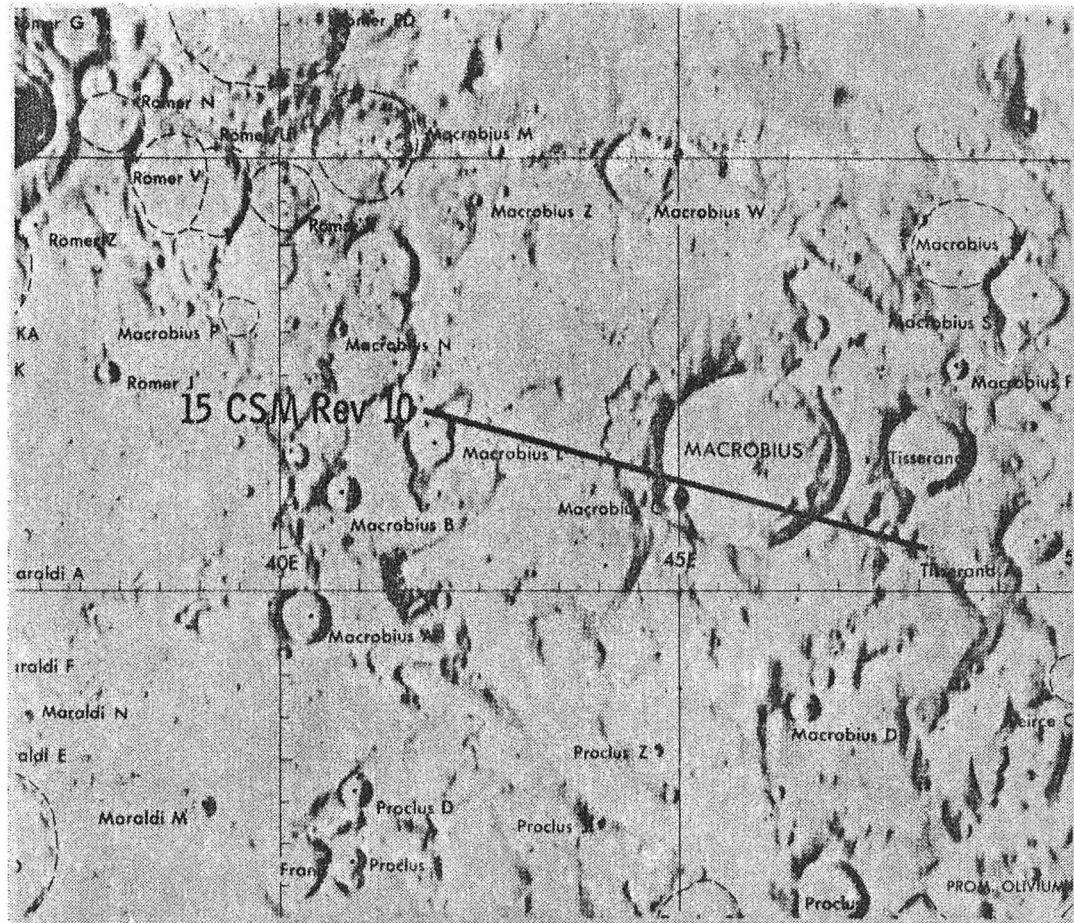
# LAMONT



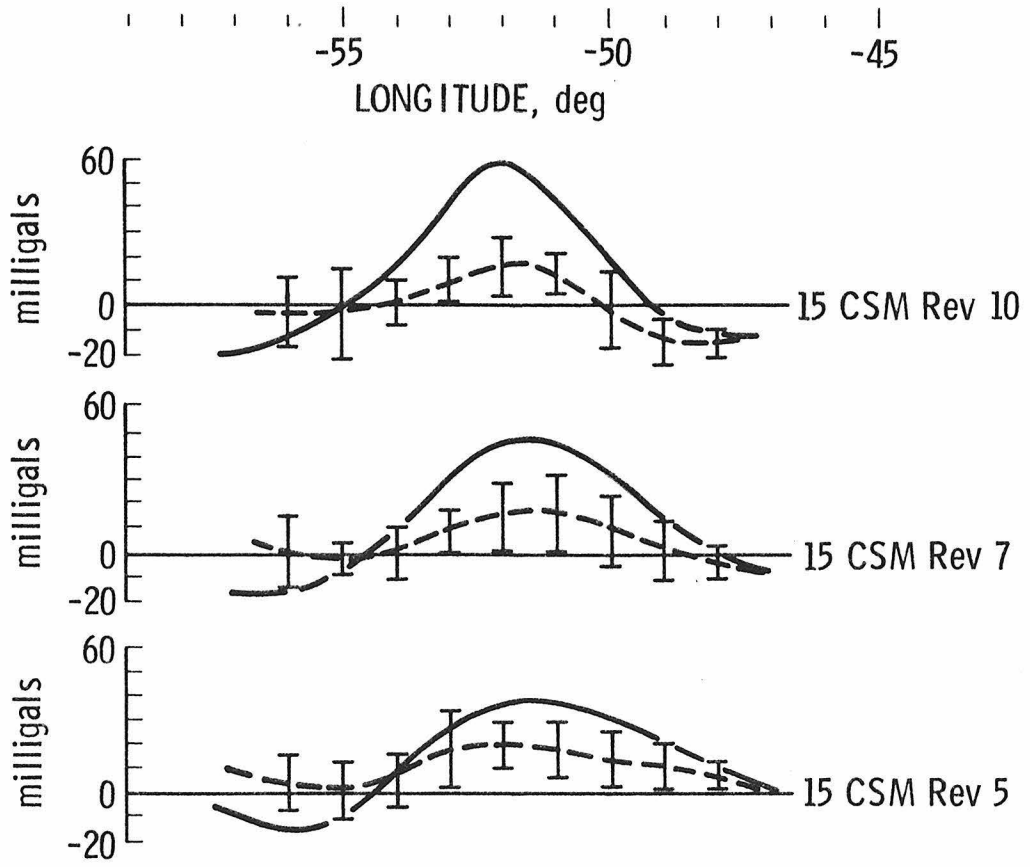
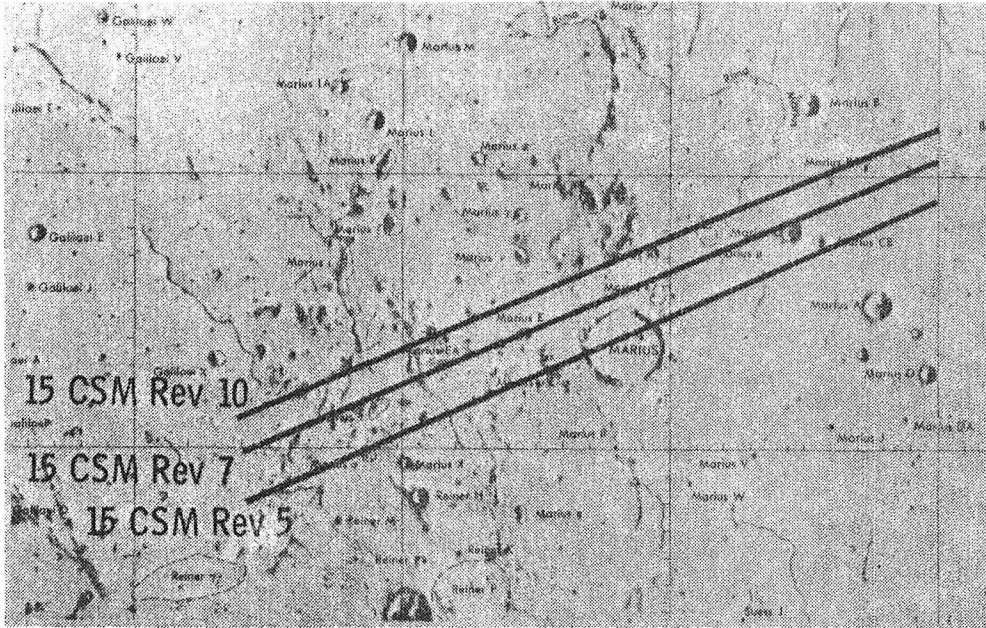
# LANGRENUS



# MACROBIUS

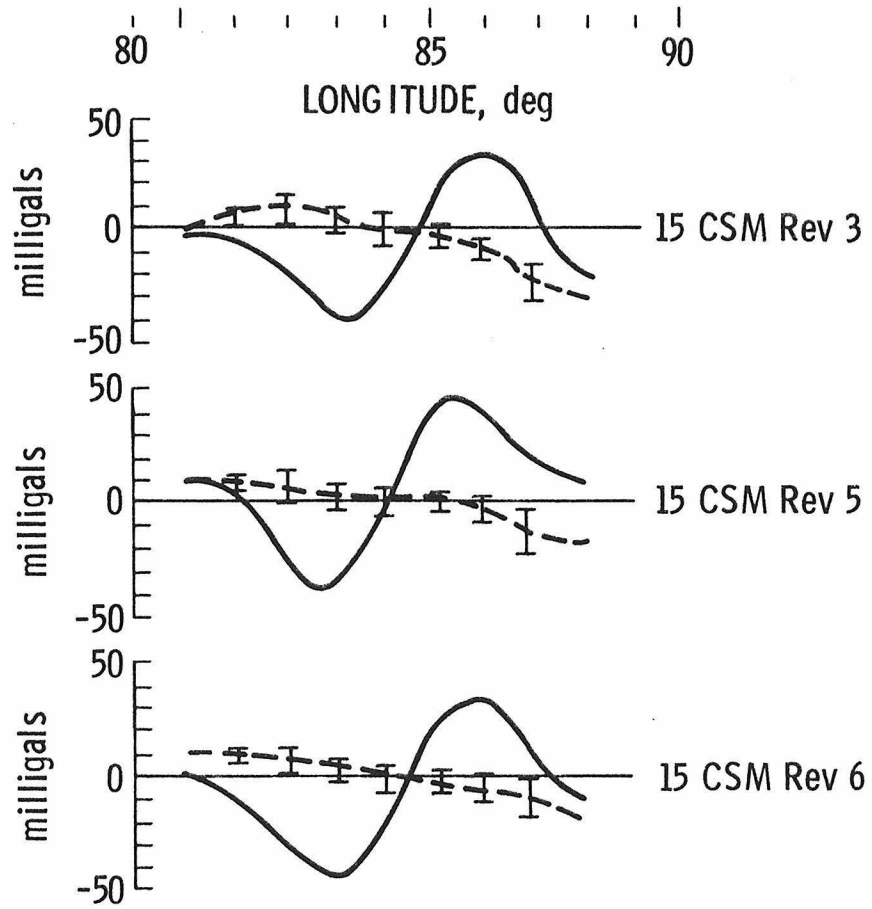
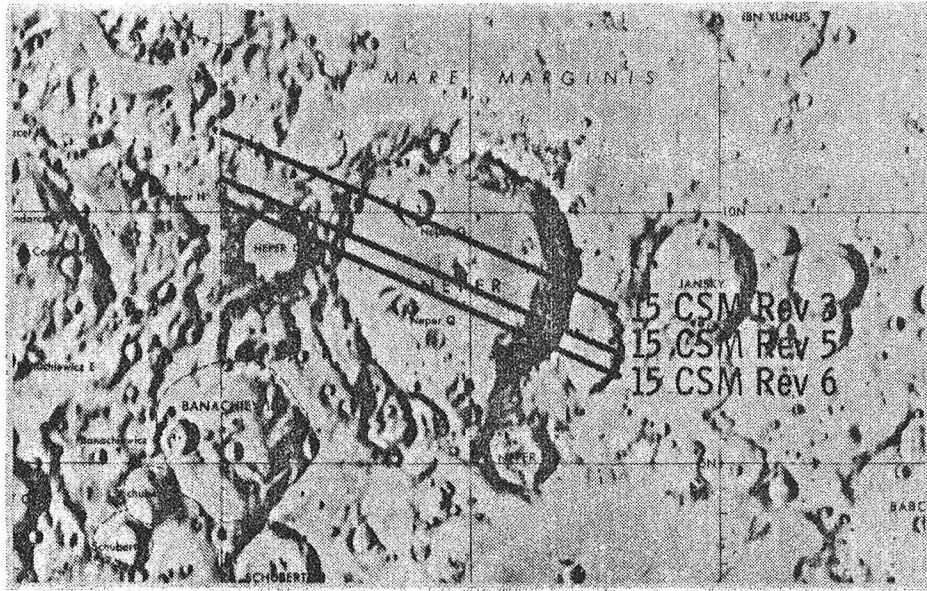


# MARIUS HILLS

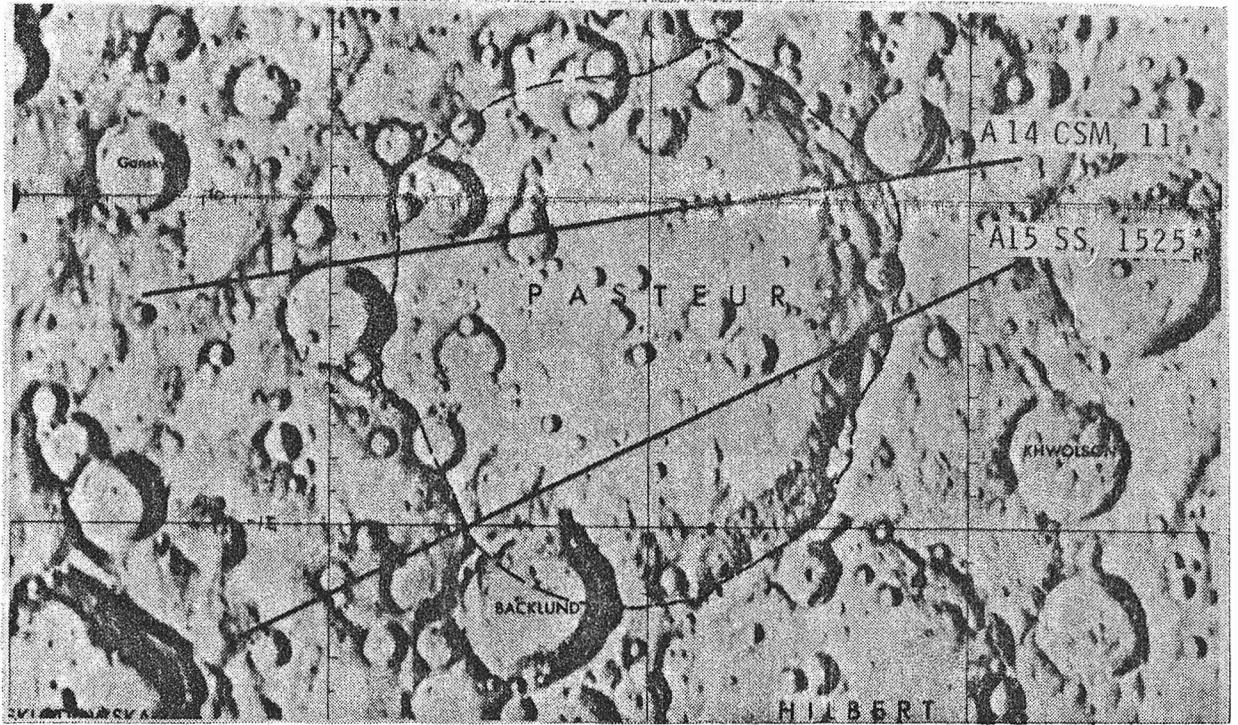




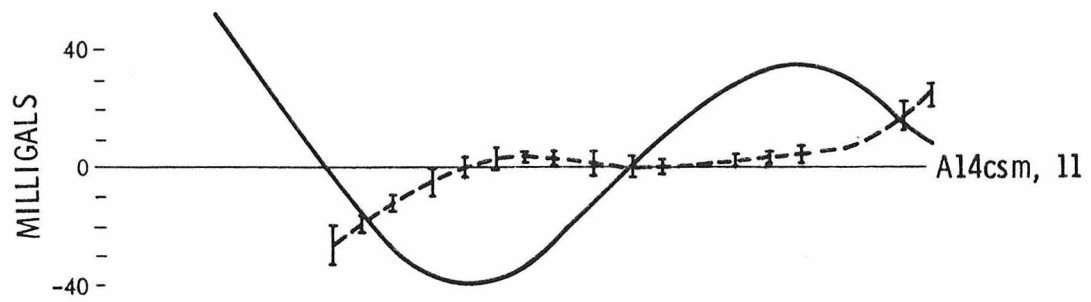
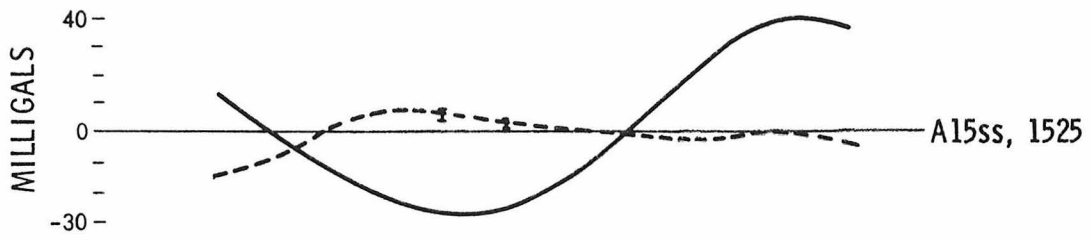
# NEPER



# PASTEUR

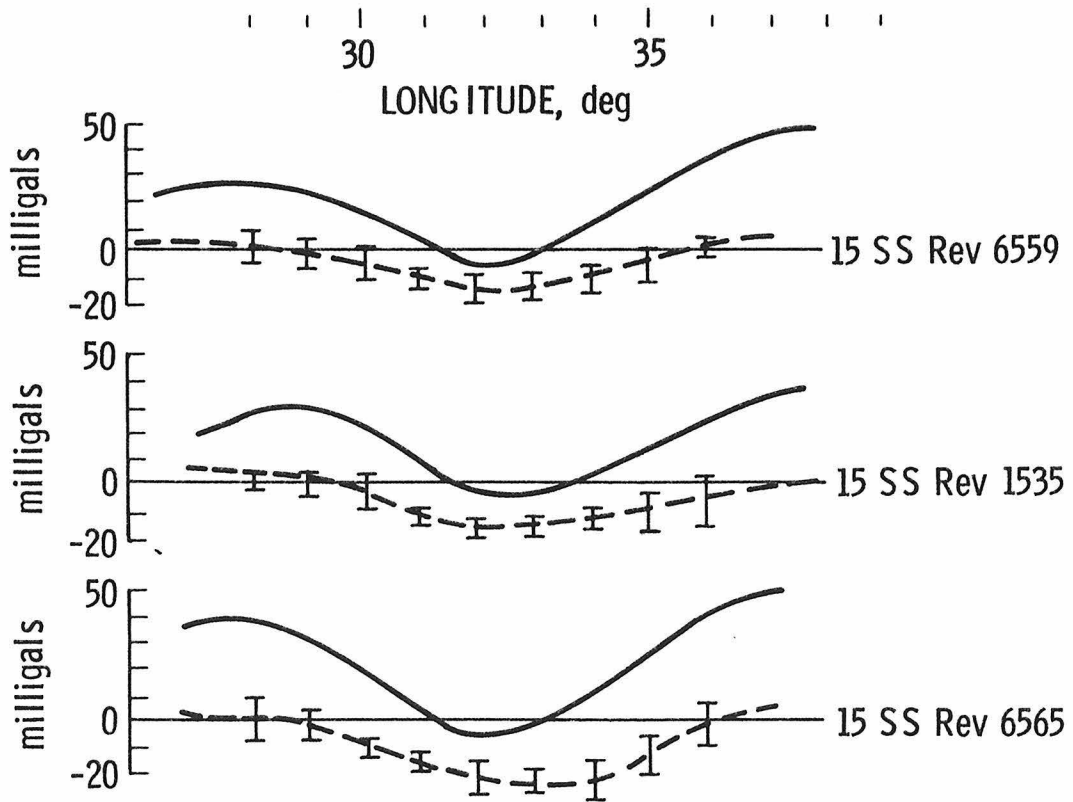
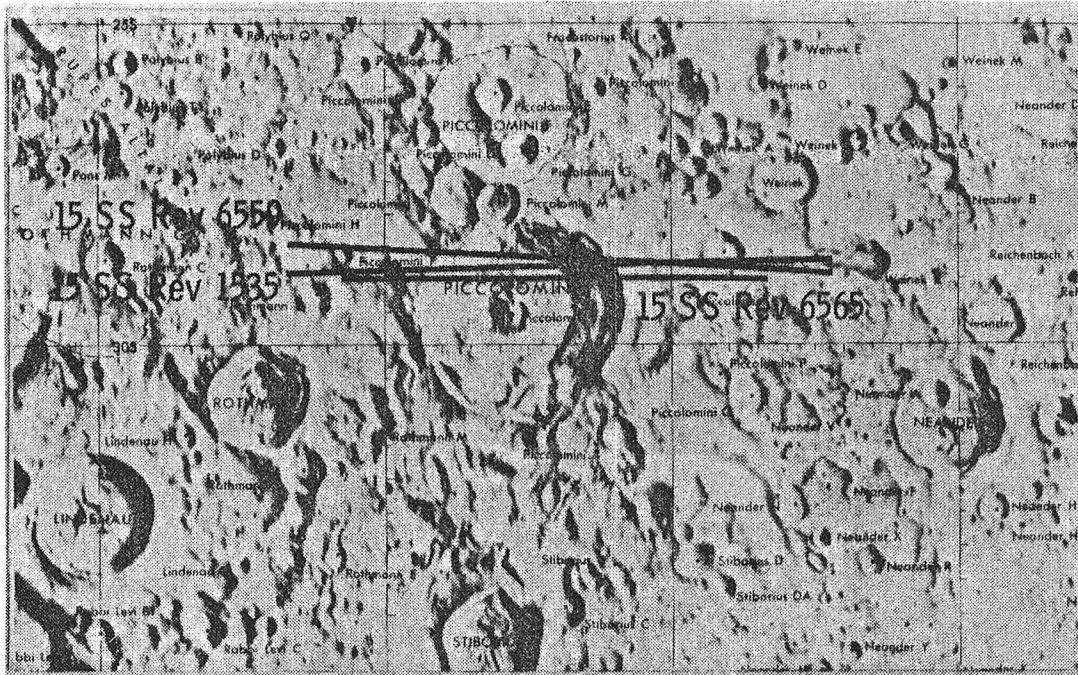


98 | 100 | 105 | 109  
LONGITUDE, deg

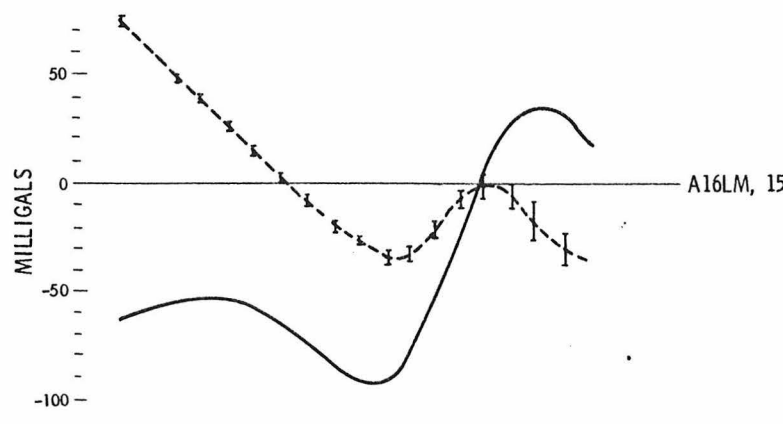
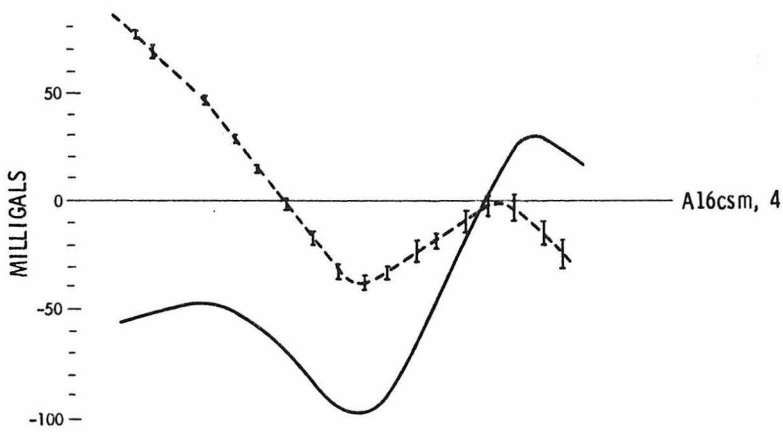
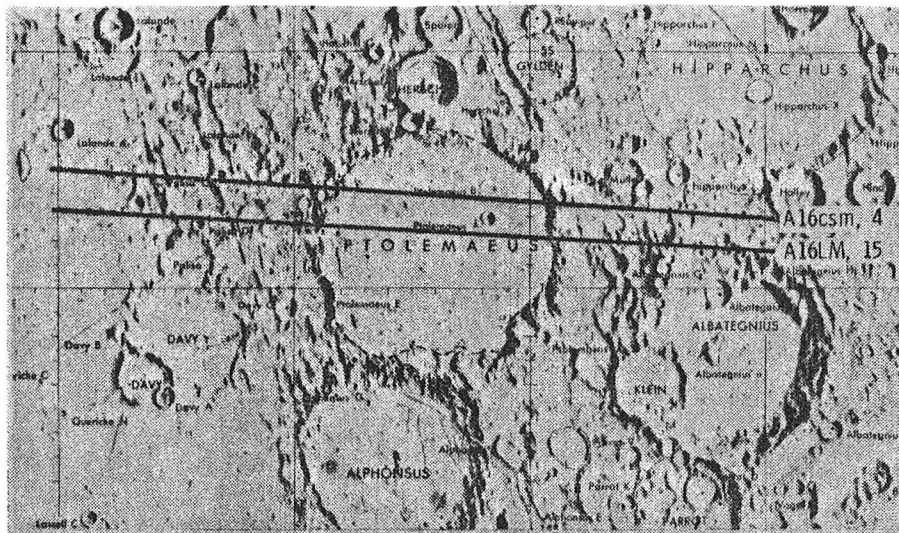




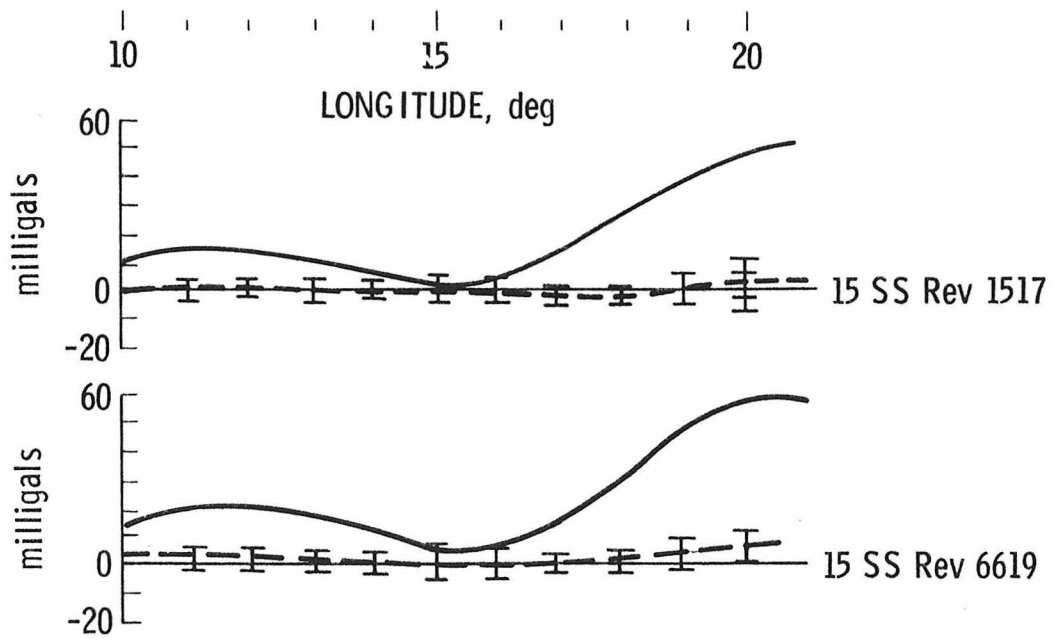
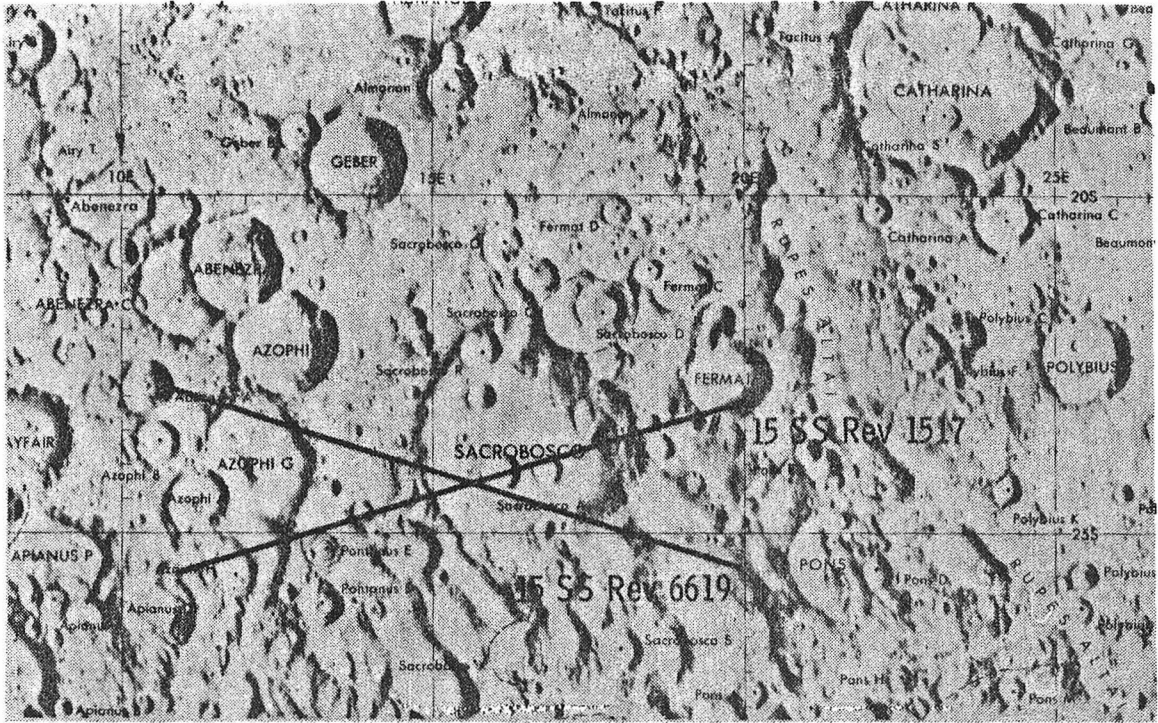
# PICCOLOMINI



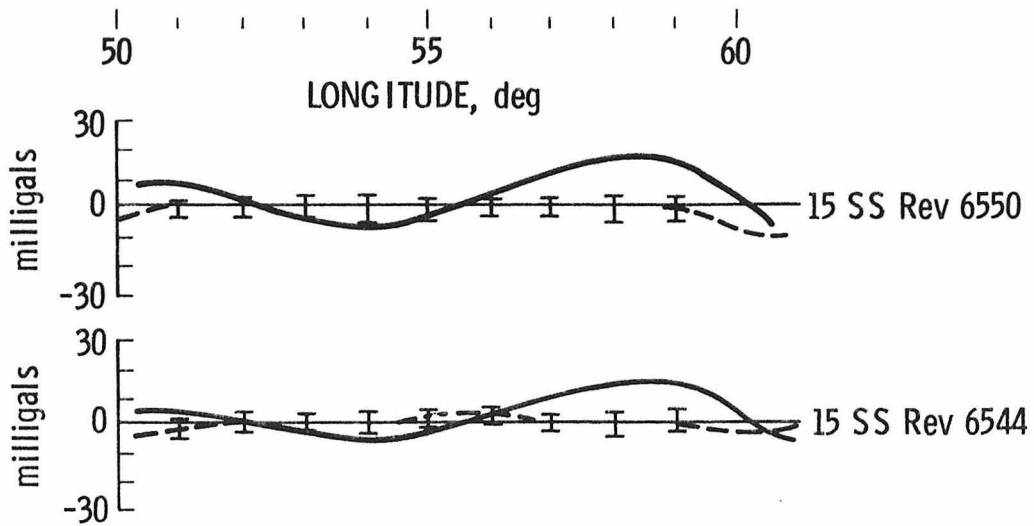
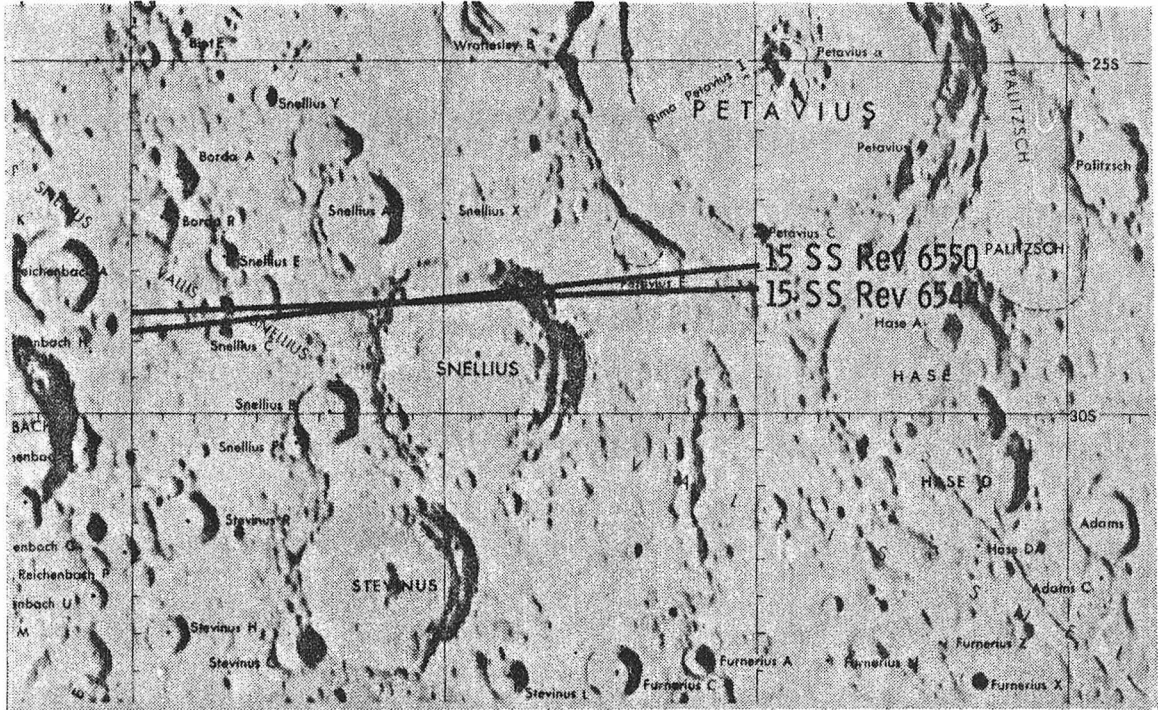
# PTOLEMAEUS



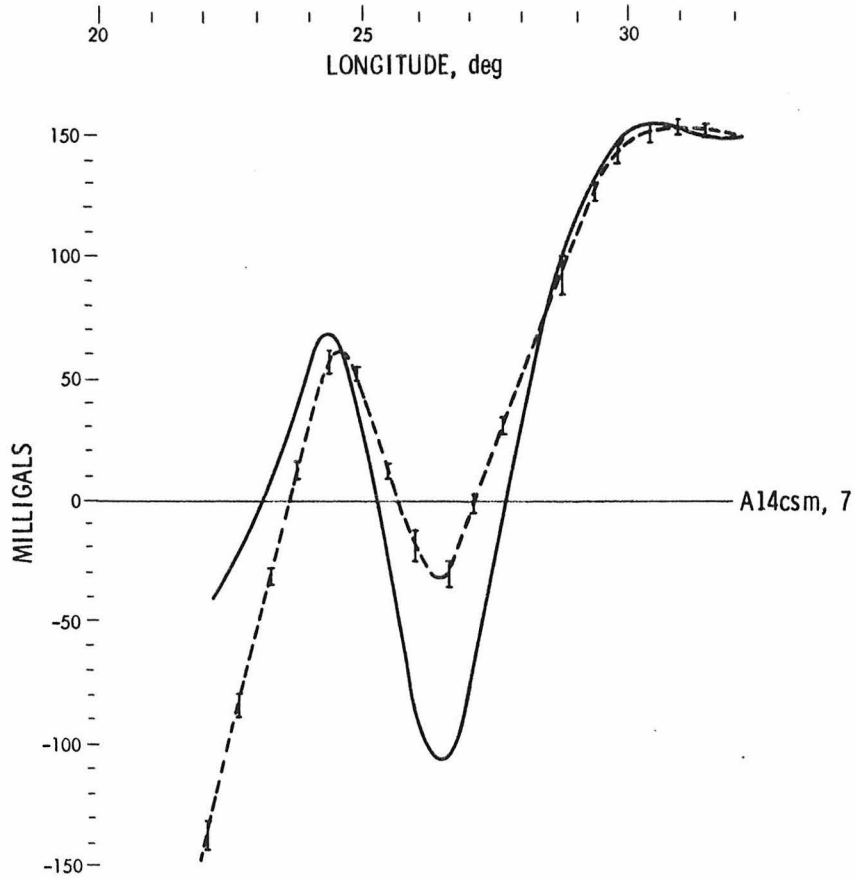
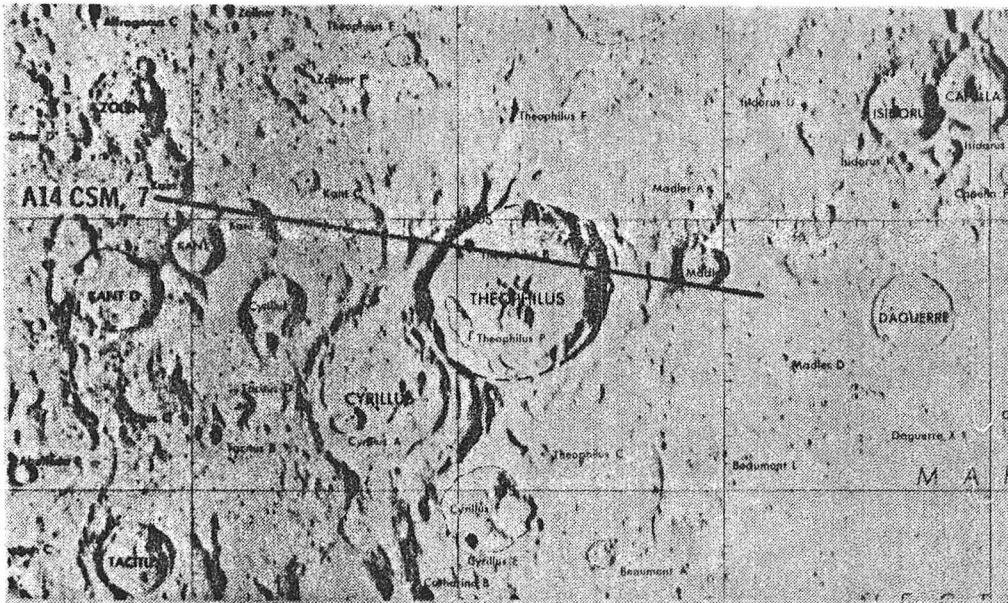
# SACROBOSCO



# SNELLIUS



# THEOPHILUS





## REFERENCES

- Ackermann, H.D., Godson, R.H., and Watkins, J.S. (1975). Refraction technique used for subsurface investigations of Meteor Crater, Arizona. J. Geophys. Res. 80, 765-775.
- Anderson, E.M. (1936). The dynamics of the formation of cone sheets, ring dikes and cauldron subsidence. Roy. Soc. Edinburgh Proc. 56, 128-157.
- Baldwin, R.B. (1963). The Measure of the Moon. Univ. Chicago Press. 488 pp.
- Baldwin, R.B. (1968). Lunar mascons: Another interpretation. Science 162, 1407-1408.
- Baldwin, R.B. (1970). Absolute ages of the lunar maria and large craters. II. The viscosity of the Moon's outer layers. Icarus 13, 215-225.
- Barkan, D.D. (1962). Dynamics of Bases and Foundations. (Translation edited by G.P. Tschebotarioff), McGraw-Hill Book Co., 68-75.
- Beals, C.S., Innes, M.J.S., and Rottenberg, J.A. (1963). Fossil meteorite craters. In The Solar System, Vol. IV., The Moon, Meteorites, and Comets. (Middlehurst, B.M. and Kuiper, G.P., eds.) Univ. Chicago Press (Chicago) 235-284.
- Beals, C.S. and Halliday, I. (1967). Impact craters on the Earth and Moon. J. Roy. Astron. Soc. Canada 61, 295-313.
- Bills, B.G. and Ferrari, A.J. (1977). A lunar density model consistent with topographic, gravitational, librational and seismic data. J. Geophys. Res. 82, 1306-1314.

- Bowin, C., Simon, G., and Wollenhaupt, W.R. (1975). Mascons: A two-body solution. J. Geophys. Res. 80, 4947-4955.
- Boyce, J.M. (1976). Ages of flow units in the lunar nearside maria based on Lunar Orbiter IV photographs. Proc. Lunar Sci. Conf. 7th, 2717-2728.
- Bryan, W.B. (1973). Wrinkle-ridges as deformed surface crust on ponded mare lava. Proc. Lunar Sci. Conf. 4th, 93-106.
- Bull, C.B., Corbate, C.E., and Zahn, J.C. (1967). Gravity survey of the Serpent Mound area, southern Ohio. Ohio J. Sci. 67, 359-371.
- Bunch, T.E. (1968). Some characteristics of selected minerals from craters. In Shock Metamorphism of Natural Materials. (French, B.M. and Short, N.M., eds.) Mono Book Co. (Baltimore) 413-432.
- Carder, D.S. and Cloud, W.K. (1959). Surface motion from large underground explosions. J. Geophys. Res. 64, 1471-1487.
- Carlson, R.H. and Jones, G.D. (1965). Distribution of ejecta from cratering explosions in soils. J. Geophys. Res. 70, 1897-1910.
- Chow, V.T. (1964). Handbook of Applied Hydrology. McGraw-Hill Book Co., p. 13-10.
- Classen, J. (1977). Catalogue of 320 certain, probable, possible, and doubtful impact structures. Meteoritics 12, 61-78.
- Coles, R.L. and Clark, J.F. (1978). The central magnetic anomaly, Manicouagan structure, Quebec. J. Geophys. Res. 86, 2805-2815.
- Conel, J.E. and Holstrom, G.B. (1968). Lunar mascons: A near-surface interpretation. Science 162, 1403-1405.

- Daly, R.A. (1903). The mechanics of igneous intrusion. Am. J. Sci. 15, 269-298.
- Daly, R.A. (1933). Igneous Rocks and the Depths of the Earth. McGraw-Hill Book, Co., pp. 267-286.
- Dence, M.R. (1965). The extraterrestrial origin of Canadian craters. Ann. N.Y. Acad. Sci. 123, 941-969.
- Dence, M.R. (1968). Shock zoning at Canadian Craters: Petrography and structural implications. In Shock Metamorphism of Natural Materials. (French, B.M. and Short, N.M., eds.), Mono Book Co. (Baltimore) 169-184.
- Dence, M.R., Innes, M.J.S., and Beals, C.S. (1965). On the probable meteorite origin of the Clearwater Lakes, Quebec. J. Roy. Astron. Soc. Canada 59, 13-22.
- Dence, M.R. and Popelar, J. (1972). Evidence for an impact origin for Lake Wanapitei, Ontario. Geol. Assoc. Canada Sp. Papers 10, 117-124.
- Dence, M.R., Grieve, R.A.F., and Robertson, P.B. (1977). Terrestrial impact structures: Principal characteristics and energy considerations. In Impact and Explosion Cratering (Roddy, D.J., Pepin, R.O., and Merrill, R.B., eds.) Pergamon Press (New York) 247-275.
- Dennis, J.G. (1971). Ries structure, southern Germany, A review. J. Geophys. Res. 76, 5394-5406.
- DeWiest, R.J.M. (1965). Geohydrology. John Wiley and Sons, pp. 168-171.

- Dietz, R.S. (1968). Shatter cones in cryptoexplosion structures. *In Shock Metamorphism of Natural Materials*. (French, B.M. and Short, N.M., eds.) Mono Book Co. (Baltimore) 267-285.
- Dymek, R.F., Albee, A.L. and Chodos, A.A. (1975). Comparative petrology of lunar cumulate rocks of possible primary origin: Dunite 72415, troctolite 765035, norite 78235, and anorthosite 62237. *Proc. Lunar Sci. Conf. 6th*, 301-341.
- Eggleton, R.E. and Schaber, G.G. (1972). Cayley formation interpreted as basin ejecta. *In Apollo 16 Preliminary Science Report*, NASA SP-315, sect. 29, 7-16.
- Elachi, C., Kobrick, M., Roth, L., Tierman, M., and Brown, W.E., Jr. (1976). Local lunar topography from the Apollo 17 ALSE radar imagery and altimetry. *The Moon 15*, 119-131.
- Erlich, E.N., Melekestsev, I.V., and Steinberg, G.S. (1974). General peculiarities of lunar volcanism. *Mod. Geol. 5*, 31-43.
- Evans, G.L. (1961). Investigations at the Odessa Meteor Crater. *Lawrence Radiation Lab. UCRL-6438*, sect. D, 1-11.
- Ferrari, A.J. (1977). Lunar gravity: A harmonic analysis. *J. Geophys. Res. 82*, 3065-3084.
- Ferrari, A.J., Nelson, D.L., Sjogren, W.L., and Phillips, R.J. (1978). The isostatic state of the lunar Apennines and regional surroundings. *J. Geophys. Res. 83*, 2863-2871.
- Fredriksson, K., Dube, A., Milton, D.J. and Balasundaram, M.S. (1973). Lonar Lake, India: An impact crater in basalt. *Science 180*, 862-864.

- French, B.M. (1968). Shock metamorphism as a geological process.  
*In Shock Metamorphism of Natural Materials.* (French, B.M. and Short, N.M., eds.) Mono Book Co. (Baltimore) 1-17.
- Fudali, R.F. and Cassidy, W.A. (1972). Gravity reconnaissance at three Mauritanian craters of explosive origin. Meteoritics 7, 51-70.
- Fudali, R.F., Gold, D.P., and Gurney J.J. (1973). The Pretoria Salt Pan: Astrobleme or cryovolcano. J. Geol. 81, 495-507.
- Gault, D.E., Quaide, W.L., and Oberbeck, V.R. (1968). Impact cratering mechanics and structures. *In Shock Metamorphism of Natural Materials.* (French, B.M. and Short, N.M., Eds.) Mono Book Co. (Baltimore) 87-99.
- Gault, D.E., Guest, J.E., Murray, J.B., Dzurisin, D., and Malin, M.C. (1975). Some comparisons of impact craters on Mercury and the Moon. J. Geophys. Res. 80, 2444-2460.
- Goldreich, P. and Soter, S. (1966). Q in the solar system. Icarus 5, 375-389.
- Gottlieb, P. (1970). Estimation of local lunar gravity features. Radio Science 5, 301-312.
- Gottlieb, P., Muller, P.M., Sjogren, W.L., and Wollenhaupt, W.R. (1970). Lunar gravity over large craters from Apollo 12 tracking data. Science 168, 477-479.
- Greeley, R. (1971). Lava tubes and channels in the lunar Marius Hills. The Moon 3, 289-314.

- Halliday, I. and Griffin, A.A. (1963). Evidence in support of a meteoritic origin for West Hawk Lake, Manitoba, Canada. J. Geophys. Res. 68, 5297-5305.
- Halliday, I. and Griffin, A.A. (1967). Summary of drilling at the West Hawk Lake Crater. J. Roy. Astron. Soc. Canada 61, 1-8.
- Hartmann, W.K. and Wood, C.A. (1971). Moon: Origin and evolution of multi-ring basins. The Moon 3, 3-78.
- Hawke, B.R. and Head, J.W. (1977). Impact melt on lunar crater rims. In Impact and Explosion Cratering. (Roddy, D.J., Pepin, R.O., and Merrill, R.B., eds.) Pergamon Press (New York) 815-841.
- Head, J.W. (1974). Orientale multi-ringed basin interior and implications for the petrogenesis of lunar highland samples. The Moon 11, 327-356.
- Head, J.W. (1977). Origin of outer rings in lunar multiringed basins: Evidence from morphology and ring structure. In Impact and Explosion Cratering. (Roddy, D.J., Pepin, R.O., and Merrill, R.B., eds.) Pergamon Press (New York) 563-573.
- Hörz, F., Gibbons, R.V., Hill, R.E., and Gault, D.E. (1976). Large scale cratering of the lunar highlands: Some Monte Carlo model considerations. Proc. Lunar Sci. Conf. 7th, 2931-2945.
- Howard, K.A., Wilhelms, D.E., and Scott, D.H. (1974). Lunar basin formation and highland stratigraphy. Rev. Geophys. Sp. Phys. 12, 309-327.

- Hughes, H.G., App, F.N., and McGetchin, T.R. (1977). Global seismic effects of basin-forming impacts. Phys. Earth Planet. Int. 15, 251-263.
- Innes, M.J.S. (1961). The use of gravity methods to study the underground structure and impact energy of meteorite craters. J. Geophys. Res. 66, 2225-2239.
- Innes, M.J.S. (1964). Recent advances in meteorite crater research at Dominion Observatory, Ottawa, Canada. Meteoritics 2, 219-241.
- Jaeger, J.C. (1968). Cooling and solidification of igneous rocks. In Basalts: The Poldervaart Treatise on Rocks of Basaltic Composition. (Hess, H.H. and Poldervaart, A., eds.) Vol. 2, 503-536.
- Jensch, Von A. (1965). Geophysikalische Messungen im Steinheimer Becken. Neues Jahrb. Mineral. Monats., 279-284.
- Johnson, T.V., Saunders, R.S., Matson, D.L., and Mosher, J.A. (1977). A  $TiO_2$  abundance map for the northern maria. Proc. Lunar Sci. Conf. 8th., 1029-1036.
- Kaula, W.M., Schubert, G., Lingenfelter, R.E., Sjogren, W.L., and Wollenhaupt, W.R. (1973). Lunar topography from Apollo 15 and 16 altimetry. Proc. Lunar Sci. Conf. 4th, 2811-2819.
- Kaula, W.M., Schubert, G., Lingenfelter, R.E., Sjogren, W.L., and Wollenhaupt, W.R. (1974). Apollo laser altimetry and inferences as to lunar structure. Proc. Lunar Sci. Conf. 5th, 3049-3058.
- Kieffer, S.W. (1971). Shock metamorphism of the Coconino Sandstone at Meteor Crater, Arizona. J. Geophys. Res. 76, 5449-5473.

- Kovach, R.L. and Watkins, J.S. (1973). The structure of the lunar crust at the Apollo 17 site. Proc. Lunar Sci. Conf. 4th, 2549-2560.
- Krinov, E.L. (1963). Meteorite craters on the Earth's surface. *In* The Solar System, Vol. IV. The Moon, Meteorites, and Comets. (Middlehurst, B.M. and Kuiper, G.P., eds.) Univ. Chicago Press (Chicago) 183-207.
- Kunze, A.W.G. (1974). Creep response of the lunar crust in mare regions from an analysis of crater deformation. Phys. Earth Planet. Int. 8, 375-387.
- Lambeck, K. (1979). Comments on the gravity, topography and moment of inertia of Mars. (in preparation).
- Latham, G.V., McDonald, W.G., and Moore, H.J. (1970). Missile impacts as sources of seismic energy on the Moon. Science 168, 242-245.
- Lin, R.P., Anderson, K.A., and Bush, R. (1977). Age distribution of lunar surface magnetic fields. *In* Lunar Science VIII. The Lunar Science Institute, Houston, 581-582.
- Linsley, R.K., Jr., Kohler, M.A., and Paulhus, J.L.H. (1958). Hydrology for Engineers. McGraw-Hill Book Co., p. 130.
- Mackin, J.H. (1969). Origin of lunar maria. Geol. Soc. Am. Bull. 80, 735-748.
- Malahoff, A. and Woollard, G.P. (1966). Magnetic measurements over the Hawaiian Ridge and their vulcanological implications. Bull. Volc. 29, 735-762.



- Malin, M.C. and Dzurisin, D. (1978). Modification of fresh crater landforms: Evidence from the Moon and Mercury. J. Geophys. Res. 83, 233-243.
- Manaytis, V.L., Mikhaylov, M.V., and Selivanovskaya, T.V. (1976). The Popigai meteorite crater. Nauka Press, Moscow. (NASA Technical Translation F-16,900).
- McCauley, J.F. (1967). Geologic map of the Hevelius region of the Moon. U.S. Geol. Surv. Map I-491.
- McConnell, R.K., Jr. (1965). Isostatic adjustment in a layered Earth. J. Geophys. Res. 70, 5171-5188.
- McCord, T.B., Charette, M.P., Johnson, T.V., Lebofsky, L.A., and Pieters, C. (1972). Spectrophotometry (0.3 to 1.1  $\mu$ ) of visited and proposed Apollo lunar landing sites. The Moon 5, 52-89.
- McGetchin, T.R., Settle, M., and Head, J.W. (1973). Radial thickness variation in impact crater ejecta: Implications for lunar basin deposits. Earth Planet. Sci. Lett. 20, 226-236.
- McGetchin, T.R., Settle, M. and Chouet, B.A. (1974). Cinder cone growth modeled after northeast crater, Mount Etna, Sicily. J. Geophys. Res. 79, 3257-3272.
- Melosh, H.J. (1976). On the origin of fractures radial to lunar basins. Proc. Lunar Sci. Conf. 7th, 2967-2982.
- Melosh, H.J. (1977). Crater modification by gravity: A mechanical analysis of slumping. In Impact and Explosion Cratering. (Roddy, D.J., Pepin, R.O., and Merrill, R.B., eds.) Pergamon Press (New York), 1245-1260.

- Milne-Thomson, L.M. (1951). The Calculus of Finite Differences.  
MacMillan and Co. (London) p. 155.
- Milton, D.J., Barlow, B.C., Brett, R., Brown, A.R., Glikson, A.Y.,  
Manwaring, E.A., Moss, F.J., Sedmik, E.C.E., Son, J. Von, and  
Young, G.A. (1972). Gosses Bluff impact structure, Australia.  
Science 175, 1199-1207.
- Minear, J.W. (1977). Melt migration: A lunar model. *In* Basaltic  
Volcanism Study Project, Vol. I. Lunar Science Institute, Houston,  
45-46.
- Mogi, K (1958). Relations between the eruptions of various volcanoes  
and the deformation of the ground surfaces around them. Bull.  
Earth. Res. Inst. 36, 99-134.
- Moore, H.J., Hodges, C.A., and Scott, D.H. (1974). Multiringed basins--  
Illustrated by Orientale and associated features. Proc. Lunar  
Sci. Conf. 5th., 71-100.
- Morris, E.C. and Wilhelms, D.E. (1967). Geologic map of the Julius  
Caesar Quadrangle of the Moon. U.S. Geol. Surv. Map I-510.
- Muehlberger, W.R., Batson, R.M., Boudette, E.L., Duke, C.M., Eggleton,  
R.E., Elston, D.P., England, A.W., Freeman, V.L., Hait,  
M.H., Hall, T.A., Head, J.W., Hodges, C.A., Holt, H.E., Jackson,  
E.D., Jordan, J.A., Larson, K.B., Milton, D.J., Reed, V.S.,  
Rennilson, J.J., Schaber, G.G., Schafer, J.P., Silver, L.T.,  
Stuart-Alexander, D., Sutton, R.L., Swann, G.A., Tyner, R.L.,  
Ulrich, G.E., Wilshire, H.G., Wolfe, E.W., and Young, J.W. (1972).  
Preliminary geologic investigation of the Apollo 16 landing

- site. In Apollo 16 Preliminary Science Report, NASA SP-315 sect. 6, 1-81.
- Muller, P.M. and Sjogren, W.L. (1968). Mascons: Lunar mass concentrations. Science 161, 680-684.
- Muller, P.M., Sjogren, W.L., and Wollenhaupt, W.R. (1974). Lunar gravity: Apollo 15 Doppler radio tracking. The Moon 9, 195-205.
- Murase, T. and McBirney, A.R. (1970). Viscosity of lunar lavas. Science 167, 1491-1493.
- Newmark, N.M. and Rosenblueth, E. (1971). Fundamentals of Earthquake Engineering. Prentice-Hall, Inc., pp 424-439.
- Oberbeck, V.R., Quaide, W.L., and Greeley, R. (1969). On the origin of lunar sinuous rilles. Mod. Geol. 1, 75-80.
- O'Keefe, J.D. and Ahrens, T.J. (1976). Impact ejecta on the Moon. Proc. Lunar Sci. Conf. 7th, 3007-3025.
- Papanastassiou, D.A., DePaulo, D.J., and Wasserburg, G.J. (1977). Rb-Sr and Sm-Nd chronology and genealogy of mare basalts from the Sea of Tranquillity. Proc. Lunar Sci. Conf. 8th, 1639-1672.
- Phillips, R.J., Conel, J.E., Abbott, E.A., Sjogren, W.L., and Morgan, J.B. (1972). Mascons: Progress toward a unique solution for mass distribution. J. Geophys. Res. 77, 7106-7114.
- Phillips, R.J., Sjogren, W.L., Abbott, E.A., and Zisk, S.H. (1978). Simulation gravity modeling to spacecraft-tracking data: Analysis and applications. J. Geophys. Res. 83, 5455-5464.
- Pike, R.J. (1967). Schroter's rule and the modification of lunar crater impact morphology. J. Geophys. Res. 72, 2099-2106.

- Pike, R.J. (1974). Depth/diameter relations of fresh lunar craters: Revision from spacecraft data. Geophys. Res. Lett. 1, 291-294.
- Pike, R.J. (1976). Crater dimensions from Apollo data and supplemental sources. The Moon 15, 463-477.
- Pike, R.J. (1977). Apparent depth/apparent diameter relation for lunar craters. Proc. Lunar Sci. Conf. 8th, 3427-3436.
- Pohl, J., Stöffler, D., Gall, H., and Ernstson, K. (1977). The Ries impact crater. In Impact and Explosion Cratering (Roddy, D.J., Pepin, R.O., and Merrill, R.B., eds.) Pergamon Press (New York) 323-404.
- Pohn, H.A. and Offield, T.W. (1970). Lunar crater morphology and relative-age determination of lunar geologic units--Part I. Classification. U. S. Geol. Surv. Prof. Paper 700-C, 153-162.
- Popelar, J. (1972). Gravity interpretation of the Sudbury area. Geol. Assoc. Can. Sp. Paper 10, 103-116.
- Regan, R.D. and Hinze, W.J. (1975). Gravity and magnetic investigations of Meteor Crater, Arizona. J. Geophys. Res. 80, 776-788.
- Reiff, W. (1977). The Steinheim Basin--An impact structure. In Impact and Explosion Cratering. (Roddy, D.J., Pepin, R.O., and Merrill, R., eds.) Pergamon Press (New York) 309-320.
- Ringwood, A.E. and Essene, E. (1970). Petrogenesis of Apollo 11 basalts, internal constitution and origin of the Moon. Proc. Apollo 11 Lunar Sci. Conf., 769-799.
- Robertson, P.B. and Grieve, R.A.F. (1975). Impact structures in Canada: Their recognition and characteristics. J. Roy.

- Astron. Soc. Canada 69, 1-21.
- Roddy, D.J. (1968). The Flynn Creek Crater, Tennessee. *In* Shock Metamorphism of Natural Materials. (French, B.M. and Short, N.M., eds.) Mono Book Co. (Baltimore) 291-322.
- Roddy, D.J. (1977). Pre-impact conditions and cratering processes at the Flynn Creek Crater, Tennessee. *In* Impact and Explosion Cratering. (Roddy, D.J., Pepin, R.O., and Merrill, R.B., eds.) Pergamon Press (New York) 277-308.
- Roddy, D.J., Boyce, J.M., Colton, G.W., and Dial, A.J. (1975). Meteor Crater, Arizona, rim drilling with thickness, structural uplift, diameter, depth, volume, and mass-balance calculations. Proc. Lunar Sci. Conf. 6th, 2621-2644.
- Sander, G.W., Overton, A., and Bataille, R.D. (1964). Seismic and magnetic investigations of the Deep Bay Crater. J. Roy. Soc. Canada 58, 16-30.
- Schaber, G.G. (1973). Lava flows in Mare Imbrium: Geologic evaluation from Apollo orbital photography. Proc. Lunar Sci. Conf. 4th, 73-82.
- Schaber, G.G., Boyce, J.M., and Moore, H.J. (1976). The scarcity of mappable flow lobes on the lunar maria: Unique morphology of the Imbrium flows. Proc. Lunar Sci. Conf. 7th, 2783-2800.
- Schultz, P.H. (1976). Floor-fractured craters. The Moon 15, 241-273.
- Schultz, P.H. and Gault D.E. (1975). Seismic effects from major basin formation on the Moon and Mercury. The Moon 12, 159-177.

- Schultz, P.H. and Gault, D.E. (1976). Seismically induced modification of lunar surface features. Proc. Lunar Sci. Conf. 6th, 2845-2862.
- Scott, D.H. (1974). The geologic significance of some lunar gravity anomalies. Proc. Lunar Sci. Conf. 5th, 3025-3036.
- Scott, D.H. and Pohn, H.A. (1972). Geologic map of the Macrobius Quadrangle of the Moon. U.S. Geol. Surv. Map I-799.
- Scott, D.H., Diaz, J.M., and Watkins, J.A. (1975). The geologic evaluation and regional synthesis of metric and panoramic photographs. Proc. Lunar Sci. Conf. 6th, 2531-2540.
- Seeger, C.R. (1968). Origin of the Jephtha Knob structure, Kentucky. Am. J. Sci. 226, 630-660.
- Seeger, C.R. (1972). Geophysical investigations of the Versailles, Kentucky, astrobleme. Geol. Soc. Am. Bull. 83, 3515-3518.
- Settle, M. and Head, J.W. (1976). The role of rim slumping in the modification of lunar crater morphometry. *In* Lunar Science VII. The Lunar Science Institute, Houston, 794-796.
- Shapiro, I.I., Zisk, S.H., Rogers, A.E.E., Slade, M.A., and Thompson, T.W. (1972). Lunar topography: Global determination by radar. Science 178, 939-948.
- Shoemaker, E.M. (1963). Impact mechanics at Meteor Crater, Arizona. *In* The Solar System, vol. IV. The Moon, Meteorites, and Comets. (Middlehurst, B.M. and Kuiper, G.P., eds.) Univ. Chicago Press (Chicago), 301-336.

- Shoemaker, E.M. and Eggleton, R.E. (1961). Terrestrial features of impact origin. In Proc. Geophys. Lab./Lawrence Radiation Lab. Cratering Sym. (Nurdyke, M.D., ed.) sect. A, 1-27.
- Short, N.M. (1970). Anatomy of a meteorite impact crater: West Hawk Lake, Manitoba, Canada. Geol. Soc. Am. Bull. 81, 609-648.
- Short, N.M. and Forman, M.L. (1972). Thickness of impact crater ejecta on the lunar surface. Mod. Geol. 3, 69-91.
- Simmons, G., Todd, T., and Wang, H. (1973). The 25-km discontinuity: Implications for lunar history. Science 182, 158-161.
- Sjogren, W.L., Gottlieb, P., Muller, P.M., and Wollenhaupt, W.R. (1972a). Lunar Gravity via Apollo 14 Doppler radio tracking. Science 175, 165-168.
- Sjogren, W.L., Gottlieb, P., Muller, P.M., and Wollenhaupt, W.R. (1972b). S-Band transponder experiment. In Apollo 15 Preliminary Science Report. NASA SP-289, sect. 20, 1-6.
- Sjogren, W.L., Wimberly, R.N., and Wollenhaupt, W.R. (1974a). Lunar gravity via the Apollo 15 and 16 subsatellites. The Moon 9, 115-128.
- Sjogren, W.L., Wimberly, R.N., and Wollenhaupt, W.R. (1974b). Lunar gravity: Apollo 16. The Moon 11, 35-40.
- Sjogren, W.L., Wimberly, R.N., and Wollenhaupt, W.R. (1974c). Lunar gravity: Apollo 17. The Moon 11, 41-52.
- Sjogren, W.L. and Smith, J.C. (1976). Quantitative mass distribution models for Mare Orientale. Proc. Lunar Sci. Conf. 7th, 2639-2648.

- Sjogren, W.L., Anderson, J.D., Phillips, R.J., and Trask, D.W.  
(1976). Gravity fields. IEEE Trans. Geoscience Electronics  
GE-14, 172-183.
- Solomon, S.C. (1974). Density within the Moon and implications for  
lunar composition. The Moon 9, 147-166.
- Solomon, S.C. (1975). Mare volcanism and lunar crustal structure.  
Proc. Lunar Sci. Conf. 6th, 1021-1042.
- Solomon, S.C. and Head, J.W. (1978). Vertical movement in mare  
basins: Relation to mare emplacement, basin tectonics, and  
lunar thermal history. J. Geophys. Res. (submitted).
- Stearns, R.G., Wilson, C.W., Jr., Tiedemann, H.A., Wilcox, J.T.,  
and Marsh, P.S. (1968). The Wells Creek structure, Tennessee.  
In Shock Metamorphism of Natural Materials. (French, B.M. and  
Short, N.M., eds.) Mono Book Co. (Baltimore) 323-337.
- Stephenson, A., Runcorn, S.K., and Collinson, D.W. (1977). Paleo-  
intensity estimates from lunar samples 10017 and 10020. Proc.  
Lunar Sci. Conf. 8th, 679-687.
- Stöffler, D. (1971a). Coesite and stishovite in shocked crystalline  
rocks. J. Geophys. Res. 76, 5474-5488.
- Stöffler, D. (1971b). Progressive metamorphism and classification  
of shocked and brecciated crystalline rocks at impact craters.  
J. Geophys. Res. 76, 5541-5551.
- Stöffler, D., Gault, D.E., Wedekind, J., and Polkowski, G. (1975).  
Experimental hypervelocity impact into quartz sand: Distribution  
and shock metamorphism of ejecta. J. Geophys. Res. 80, 4062-4077.



- Strom, R.G. (1972). Lunar mare ridges, rings and volcanic ring complexes. *In* The Moon. (Runcorn, S.K. and Urey, H.C., eds.) 187-215.
- Sweeney, J.F. (1978). Gravity study of great impact. J. Geophys. Res. 83, 2809-2815.
- Talwani, M., Thompson, G., Dent, B., Kahle, H.G., and Buch, S. (1973). Traverse gravimeter experiment. *In* Apollo 17 Preliminary Science Report. NASA SP-330, sect. 13, 1-13.
- Todd, T., Richter, D.A., Simmons, G., and Wang, H. (1973). Unique characterization of lunar samples by physical properties. Proc. Lunar Sci. Conf. 4th, 2639-2662.
- Toksöz, M.N., Dainty, A., Solomon, S.C., and Anderson, K.R. (1974). Structure of the Moon. Rev. Geophys. Space Phys. 12, 539-567.
- Trueman, D.L. (1976). Evidence in support of a meteorite impact crater at Poplar Bay, Lac du Bonnet, southeastern Manitoba, Canada. Can. J. Earth Sci. 13, 1608-1612.
- Turcotte, D.L. and Ahern, J.L. (1978). A porous flow model for magma migration in the asthenosphere. J. Geophys. Res. 83, 767-772.
- Van Lopik, J.R. and Geyer, R.A. (1963). Gravity and magnetic anomalies of the Sierra Madera, Texas, "dome". Science 142, 45-47.
- Walcott, R.I. (1970). Isostatic response to loading of the crust in Canada. Can. J. Earth Sci. 7, 716-727.
- Walsh, J.B. (1965). The effect of cracks on the compressibility of rock. J. Geophys. Res. 70, 381-389.

- Waters, A.C. (1962). Basalt magma types and their tectonic associations. The Crust of the Pacific Basin. Am. Geophys. Union Monograph 6, 158-170.
- Weertman, J. (1970). The creep of the Earth's mantle. Rev. Geophys. Space Phys. 8, 145-168.
- Whitford-Stark, J.L. (1973). Internal origin for lunar rilled craters and the maria. Nature 248, 573-575.
- Whitford-Stark, J.L. and Head, J.W. (1977). The Procellarum volcanic complexes: Contrasting styles of volcanism. Proc. Lunar Sci. Conf. 8th, 2705-2724.
- Wilhelms, D.E. and McCauley, J.F. (1971). Geologic map of the near side of the Moon. U.S. Geol. Surv. Inv. Map I-703.
- Williams, H. (1941). Calderas and their origin. Univ. Calif. Bull. Geol. Sci. 25, 239-246.
- Wise, D.U. and Yates, M.T. (1970). Mascons as structural relief on a lunar 'moho'. J. Geophys. Res. 75, 261-268.
- Wong, L., Buechler, G., Downs, W., Sjogren, W.L., Muller, P., and Gottlieb, P. (1971). A surface-layer representative of the lunar gravitational field. J. Geophys. Res. 76, 6220-6236.
- Wood, J.A. (1970). Petrology of the lunar soil and geophysical implications. J. Geophys. Res. 75, 6497-6513.
- Yurk, Y.Y., Yeremenko, G.K., and Polkanov Yu. A. (1975). The Boltysh depression--A fossil meteorite crater. Intern. Geol. Rev. 18, 196-202.

- Zisk, S.H. (1972a). A new, Earth-based radar technique for the measurement of lunar topography. The Moon 4, 296-306.
- Zisk, S.H. (1972b). Lunar topography: First radar-interferometer measurements of the Alphonsus-Ptolemaeus-Arzachel region. Science 178, 977-980.